Visualization of ionically active channels in the Nafion® membrane by using Electrochemical Atomic Force Microscopy

vorgelegt von

Dipl.-Chem. Elena Aleksandrova

aus Presnowka, Kasachstan

CONTENTS

EIDESSTATTLICHE ERKLÄRUNG

Hiermit versichere ich Eides statt, dass ich die vorliegende Arbeit ohne fremde Hilfe selbständig verfasst habe. Außer den angegebenen Literaturstellen wurden keine weiteren Hilfsmittel verwendet.

Stuttgart, den 03.12.2012   Elena Aleksandrova

Prüfungsvorsitzender: Prof. Dr. Frank Gießelmann

Hauptberichter: Prof. Dr. Emil Roduner

Mitberichter: Prof. Dr. K. Andreas Friedrich

Tag der mündlichen Prüfung: 03.12.2012

Danksagung

An dieser Stelle möchte ich allen danken, die mir die Vollendung meiner Promotion ermöglicht haben.

Ganz besonderer Dank gebührt meinem Doktorvater, Herrn Prof. Dr. E. Roduner für die Überlassung dieses interessanten und facettenreichen Themas, sowie für seinen Glauben an meine Fähigkeiten, ständige Förderung und wissenschaftliche Betreuung dieser Arbeit.

Frau Prof. Renate Hiesgen gilt mein besonderer Dank für zahlreiche, fachliche Diskussionen und ständige Unterstützung. Ganz besonders bedanke ich mich bei Dir und der Hochschule Esslingen für die Überlassung der Messgeräte, ohne die eine Fertigstellung der Dissertation nicht möglich gewesen wäre.

Besten Dank an Herr Prof. Dr. K. A. Friedrich für die Begutachtung meiner Arbeit und Publikationen.
Danke an Herr Til Kaz (Deutsches Zentrum für Luft- und Raumfahrt e.V) für die Beschichtung der in dieser Arbeit verwendeten Membranen.

Mein großer Dank gilt auch für die Mitarbeiter der Institutswerkstatt, insbesondere dem Herrn Jürgen Hußke und Mitarbeitern der HS-Esslingen Dr. Jürgen Haiber und Bernd Jung.

Ich bedanke mich auch bei allen Mitgliedern des Arbeitskreises und allen Kollegen, die mir durch fachliche Tipps und mit den freundlichen Worten geholfen haben. Danke für die angenehme und hilfsbereite Arbeitsatmosphäre.

Vielen Dank gilt auch Frau Inge Blankenship für ihre Hilfe bei allen organisatorischen Fragen.

Mein herzlicher Dank geht an meine Eltern und meinen Bruder. Alex danke Dir für die Motivation! Danken möchte ich auch meiner Oma, die mich in jeglicher Hinsicht unterstützt und mir stets den notwendigen Rückhalt gegeben hat.

Chapter 1

1   INTRODUCTION

1.1   Main objectives

Most of the automotive manufacturers worldwide have announced to start commercialization of fuel cell vehicles. However, existing vehicles are only available on a prototype status. The widespread industrial development of fuel cells is impeded by several component limitations. For polymer electrolyte membrane fuel cells (PEMFCs) as an example, the barriers to commercialization include the cost of stack and durability. The high cost of PEMFCs is due to the use of platinum particles as the catalysts of the hydrogen oxidation and oxygen reduction reaction, the proton conducting membranes e.g. "Nafion®" and the bipolar plates which are often made of graphite or its composites. As one of the major hurdles for PEMFCs to become an affordable commodity in the long term, the automotive industry has identified the material properties of the polymer electrolyte membrane which limits fuel cell operation in terms of operating temperature and humidification conditions.

New types of electrolyte membranes and catalysts can offer a solution, but at first several questions about fundamental electrochemical mechanism need to be solved to verify the potential of the components in the operating fuel cell. Therefore, not only new materials have to be developed for improved performance but also new investigation techniques in order to clarify the impact of the degradation mechanism on the fuel cell efficiency.

In a PEMFC the membrane separates the anodic and cathodic reaction chambers in terms of electric isolation and reactant separation and provides proton conductivity. The operating conditions have to be chosen in such a way that the membrane can maintain mechanical integrity as well as provide highest ion conductivity and electrochemical stability [1–3].

In general, the fuel cell performance is directly related to ion conductivity in the membrane, which in turn depends strongly upon its degree of hydration and on the

distribution of the ion transport channels which are a result of polymer microphase separation into hydrophilic and hydrophobic domains [4]. Understanding the membrane conductivity under working conditions is one of the most challenging tasks in low-temperature fuel cell research. Indeed, the electro-osmosis in the course of the proton passage across the membrane as well as the production of additional water at the cathode, give rise to a current distribution that is spatially inhomogeneous and fluctuates in time. This may be caused by the structure of the interface between the ion-exchange polymer and the catalyst layer. At places with very high reactant turnover the reaction heat leads to the formation of "hot spots", causing higher membrane resistance due to partial membrane drying at the anode side and initiating free radical formation, which can accelerate membrane degradation [5].

The nanoscale information is essential to understand the performance limiting features. In this work an electrochemical atomic force microscopy (EC-AFM) method is used to provide the surface topology of a Nafion® 112 membrane and provides a detailed picture of proton conductivity on the nm-scale, allowing comparison to existing X-ray scattering methods. The observed dynamics of large conductivity changes of Nafion® is reflected in the formation of current pathways at room temperature and given relative humidity. Time resolved experiments are used to compare with theories of proton conduction in fuel cell membranes and verify models of microphase-separated structure derived from existing microscopic data. Furthermore, the measured current values reveal a remarkable correlation with the size of the conductive areas. Analysis of the distribution of conductive areas on the Nafion® surface suggests that there are different mechanisms which contribute to the proton current in Nafion® membrane. Additionally, time dependence in local conductivity is found and analyzed in terms of redistribution of water in the membrane. A statistical analysis of the current distribution is performed and compared with theoretical simulations. Evidence is found for the existence of a critical current density. On a timescale of seconds the response of the conductive network is probed by applying voltage steps to the AFM tip.

1.2   Overview of the research

The Dissertation consists of five main parts. In the INTRODUCTION a short foreword about research areas of interest and aims of the work are given. It is followed by the FUNDAMENTALS where several topics concerning fuel cell research are discussed. Fuel cells as power sources from an electrochemical point of view are introduced. Possible pathways of current distribution and membrane degradation are pointed out. An introduction into specific aspects of fuel cell operation and oxygen reduction at the cathode side of the fuel cell provides a background for a better understanding of results obtained in experiments and calculations later-on. Recent ideas on membrane degradation are demonstrated and discussed.

The chapter EXPERIMENTAL METHODS introduces the employed EC-AFM and preparation of the membrane coating technique as well as the 3-D analysis using the WSxM and Matlab software. The RESULTS AND DISCUSSION part summarizes experimental data from EC-AFM studies of fuel cell Nafion$^{®}$ membranes. The influences of applied voltage on the membrane conductivity are discussed. An evaluation of results obtained with WSxM and Matlab software are given. The presence of an applied electric field and coadsorbed water molecules as well as the significance for low temperature fuel cells are discussed. A SUMMARY resumes the results.

Chapter 2

2 FUNDAMENTALS

2.1 General fuel cell concepts

During the last decades an enormous effort in research and development was undertaken to improve the fuel cell performance, especially in the fields of automotive and of portable power sources [6]. Today, almost every car manufacturer has built and demonstrated at least one prototype fuel cell-powered vehicle. The benefits obtained using a fuel cell for energy conversion are high efficiency and low emissions. Although fuel cells are only nowadays gaining commercial interest, the principle of operation was discovered already in 1838-1842 from Christian Schönbein and William Grove [7, 8]. The engineering work is attributed to Grove because he finally constructed an operating cell consisting of continuous feed of hydrogen and oxygen reactants to platinum electrodes and a sulfuric acid solution as an electrolyte [9, 10]. After several years the research on fuel cells acquired new impetus leading to the invention of new cell assemblages, including polymer electrolyte fuel cells (PEFCs) as a result of development work at General Electric (USA) during the 1950s [11, 12]. PEFCs proved their power as an energy source in the Gemini spacecraft during the early 1960s. This was followed by the Apollo Space Program, which used the fuel cells to generate electricity for life support, guidance, and communications. This program strongly makes the case for fuel cells as a power source for automobiles addressing the rising costs of oil and increasing environmental concerns. In 1989, Perry Energy Systems working with Ballard successfully demonstrated a PEM fuel cell-powered submarine [13]. In 1993, the PEM fuel cell system appeared as the most attractive object for development. High power densities were obtained as a result of new membrane types and catalyst research. Ballard Power Systems demonstrated fuel cell-powered buses and the first passenger car. Of

15

several different types of fuel cells under development today, PEFCs have been recognized as a potential future power source for zero-emission vehicles [14]. Fundamentally, a fuel cell is an electrochemical energy converter that converts chemical energy of fuel directly into electricity, avoiding the low efficiency conversion of thermal to mechanical energy occurring in thermo-mechanical engines. Typical reactants for the PEM fuel cell are hydrogen and oxygen. It is widely believed that hydrogen can serve as a future energy carrier. It can be produced from the nearly unlimited supply of water with no inherent emission of pollutants, and oxygen can be taken directly from the air. The consumption of hydrogen by converting it into electricity again produces water resulting in a closed material loop. Today, hydrogen is mainly obtained via a reforming process from (non-renewable) energy carriers like natural gas, hydrocarbons, and also from methanol. If the hydrogen is produced from renewable energy sources, then the electrical power produced can be truly sustainable.

2.1.1   Electrochemical background

The fuel cell consists of an electrolyte, negative and positive electrodes. The electrochemical reactions occur at the surface of the catalyst, in particular at the interface between catalyst and the polymer electrolyte membrane. During operation, a fuel cell generates waste heat and water as by-products. To regulate the supply of reactant gases, their exhaust, and the cell temperature it needs a supporting system.

In a typical PEM fuel cell a membrane with sulfonic acid cation exchange groups are utilized and, therefore, the electrochemical reactions take place simultaneously under strongly acidic conditions as is shown in Fig. 1. Hydrogen is fed to the anode, where it is oxidized on the platinum electrocatalyst according to the following reaction:

$$\text{Anode: } 2H_2 \rightarrow 4H^+ + 4e^- \tag{2-1}$$

The cathode, similarly electrocatalyzed with platinum, is fed with oxygen from the air. At this electrode electrons and protons are combined with oxygen producing water:

$$\text{Cathode: } O_2 + 4H^+ + 4e^- \rightarrow 2H_2O \tag{2-2}$$
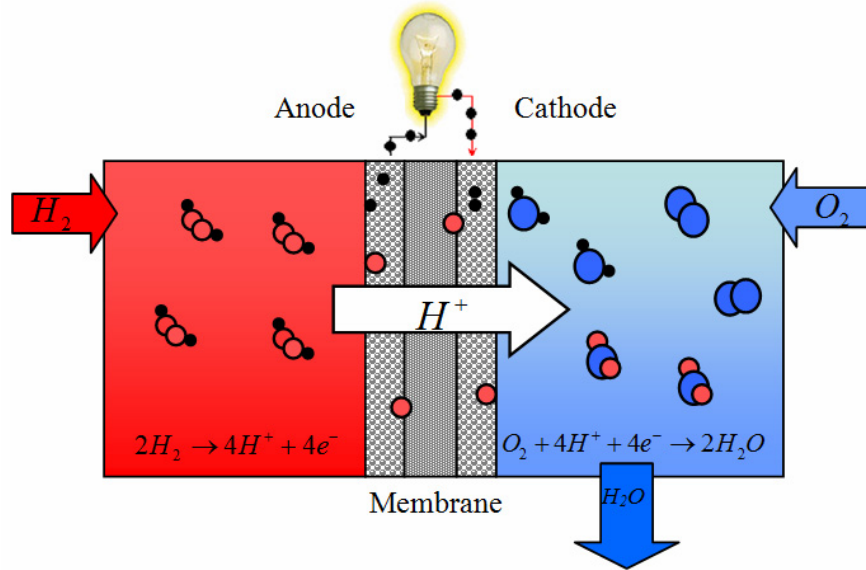
Figure 1: Basic principle of operation of a PEM fuel cell. Hydrogen is oxidized at the anode, and the protons formed are transported to the cathode through the polymer electrolyte while the electrons are conducted via the external circuit to the cathode where both react with oxygen.

The overall reaction is the same as the reaction of hydrogen combustion, which is a strongly exothermic and exergonic process:

$$\text{Overall: } H_2 + \frac{1}{2}O_2 \rightarrow H_2O \text{ with } \Delta G = -273 \text{ kJ mol}^{-1} \qquad (2\text{-}3)$$

Under standard conditions (298 K, 1 atm) the theoretical reversible potential of this reaction can be calculated using following equation:

$$\Delta E^0 = \frac{-\Delta G}{nF} = 1.23 \text{ V} \qquad (2\text{-}4)$$

where ΔG corresponds to the Gibbs free energy. In practice this potential, called the open circuit potential (OCP), is significantly lower than the theoretical potential, usually lower than 1 V. The primary losses that contribute to a reduction in cell voltage are:

 ✓ **Ohmic losses** contribute only when a current flows. They are a result of the combined resistances of the various components of the fuel cell. This includes electronic resistance of the electrode materials, the ionic resistance of the electrolyte membrane and the resistance of various interfaces. Generally,

thinner membranes are advantageous because they keep the anode electrode wet by "back" diffusion of water from the cathode, where it is generated, towards the anode.

✓ **Activation losses** are the largest losses at any current density. They associated with slow electrode kinetics. The higher the exchange current density, the lower the activation polarization losses. These losses happen at both anode and cathode, however, oxygen reduction requires much higher overpotentials and is about 100 times slower than that of the reaction at the anode. When the current density is low, the activation overpotential is the main loss mechanism [15].

✓ **Concentration losses** occur when reactants are rapidly consumed during operation (also referred to "mass transport"). As the current density continues increasing, the mass transport limitation results from the reduction of the concentration of hydrogen and oxygen gases at the electrode. For example, following the reaction new gases must be made immediately available at the catalyst sites. With the build-up of water at the cathode, particularly at high currents, catalyst particles can become flooded, restricting oxygen access. It is therefore important to remove this excess water, hence the term "mass transport".

Fuel crossover and internal currents have a dramatic effect at open circuit potential or when the fuel cell operates at very low current densities. Fuel crossover and internal currents are a result of fuel that crosses directly through the electrolyte, from the anode to the cathode without releasing electrons through the external circuit, thereby decreasing the efficiency of the fuel cell.

In practice the voltage-current dependence can be obtained from equation (2-5) describing the main loss terms:

$$V_{cell} = E^0 - IR - \left| V_{A,act} + V_{A,mt} \right| - \left| V_{C,act} + V_{C,mt} \right| \qquad (2-5)$$

where $V_{i,act}$ corresponds to activation overpotentials, IR to Ohmic resistance, $V_{i,mt}$ to mass transport limitations and subscript A refers to the anode and C to the cathode. These losses are most often shown in a Tafel plot or polarization curve where the cell potential in volts is plotted versus the cell current density in amperes per square centimeters [16]. The current density basically represents how fast the reaction is taking place (it is the

number of electrons per second, divided by the surface area of the fuel cell electrolyte face). Each of the described overpotentials dominates at different current density regions. There is a continuous drop in voltage as current increases, and this is due to linear, Ohmic losses in the ionic conduction through the electrolyte. At very high current densities, mass transport causes a rapid drop-off in the voltage s. Fig.2.
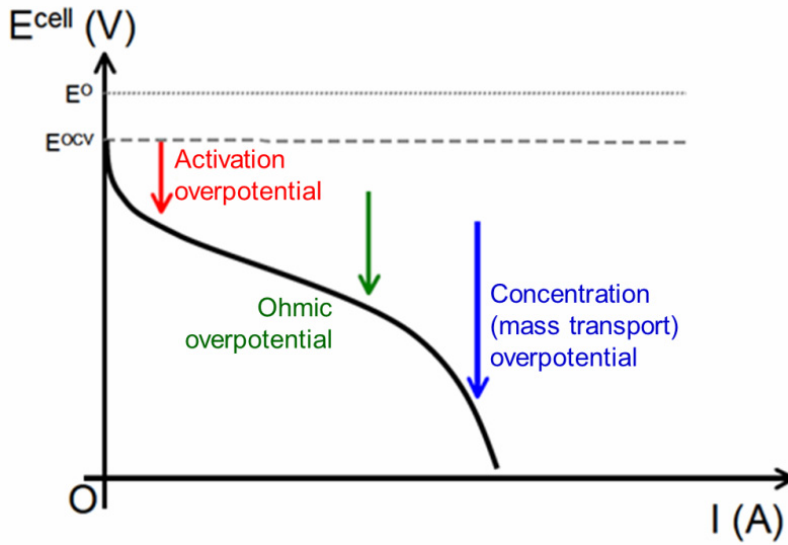
Figure 2: Schematic PEM fuel cell polarization curve [17]**.**

Fuel cell efficiencies

Besides the above mentioned objectives for a fuel cell the useful energy output is the electrical energy produced, and energy input is the reaction enthalpy of hydrogen with oxygen. Assuming that all of the Gibbs free energy can be converted into electrical energy, the maximum possible thermodynamic efficiency η_{th} can be given as:

$$\eta_{th} = \frac{\Delta G}{\Delta H} = \frac{\Delta H - T\Delta S}{\Delta H} = 1 - \frac{T\Delta S}{\Delta H} \qquad (2\text{-}6)$$

At standard conditions, ΔH for the hydrogen/oxygen reaction is -285.83 kJ mol^{-1}, and ΔG is -237.14 kJ mol^{-1}. The theoretical thermodynamic efficiency of a system can be in excess of 80%, which is comparatively high compared to a system producing electricity alone. The Faradaic efficiency η_F is defined as:

$$\eta_F = \frac{I}{I_{th}} \qquad (2\text{-}7)$$

I is the observed current from the fuel cell and I_{th} is the theoretically expected current on the basis of the amount of reactants consumed, assuming that the overall reaction in the fuel cell proceeds to completion [18].

A measure of the quality of a fuel cell - apart from operational life, weight, cost and other parameters - is the electrochemical efficiency and electrochemical kinetics of the electrodes. The electrochemical efficiency η_{el} is also termed voltage efficiency and is defined as:

$$\eta_{el} = -\frac{nFE_K}{\Delta G^0} = \frac{E_K}{E^0} \qquad (2\text{-}8)$$

where E_K is the operating potential and E^0 the standard electrode potential. Electrochemical efficiencies observed in H_2/O_2 fuel cells are as high as 0.9 at low current densities and decrease only slowly with increasing current drawn from the cell until a limiting value is reached.

Fuel cell systems are often used as co-generation systems, and the overall efficiency can be calculated as product of thermodynamic, Faradaic and electrochemical efficiency:

$$\eta_{tot} = \eta_{th} \cdot \eta_{el} \cdot \eta_F \qquad (2\text{-}9)$$

Exact data depend on the system design and can only be obtained experimentally [19]. Generally, fuel cells may operate above 90% when operated with pure hydrogen.

Additional information about the fuel cell may become available by plotting the power density as a function of current density [20]. Such a plot shows that there is a maximum power density a fuel cell may reach. It does not make sense to operate a cell at a point beyond this maximum, because the same power may be obtained at a lower current and higher potential.

Generally, the decrease in cell voltage is directly equivalent to a reduction in efficiency. The overall goal is to minimize the polarization losses by the development of more suitable materials, e.g. different electrode structures, membranes with enhanced conductivity, or better catalysts. Another approach is the modification of the cell

operation conditions, e.g. application of higher pressures, higher operation temperatures, or changes in the gas composition. In the latter case one always has to find a compromise between the application of more extreme operating conditions and the stability and durability of the fuel cell components. This problem is best explained by the variations in the operating temperature. With increasing temperature both reaction rate and mass transfer rate increase, the electrolyte resistance decreases (due to higher ionic conductivity) and the tolerance towards impurities increases. However, with increasing temperature catalyst sintering and electrolyte degradation as well as electrolyte loss due to water evaporation are also accelerated.

2.1.2   Fuel cell components

2.1.2.1   Electrodes

A fuel cell electrode is essentially a thin catalyst layer pressed on the ionomer membrane and electrically conductive substrate. Due to the fact that there are three kinds of species that participate in the electrochemical reactions the reaction can take place at the three-phase boundary, namely ionomer, active catalyst layer and void phase. It is very important that the catalysts particles are electrically connected to the substrate in order to minimize the cell potential losses. On the other hand, during the fuel cell operation protons travel through ionomer, therefore the catalyst must be in contact with the ionomer. Furthermore, the electrodes must be porous because the reactant gases must reach the interface between the electrodes and the membrane. Due to the fact that the electron transport resistance is normally negligible compared with the proton transport resistance, the limiting factors for electrochemical reaction in a PEMFC are the interfacial electron transfer kinetics, the gas (oxygen) transport resistances in the catalyst layer and backing diffusion layer, and the proton transport resistance in the catalyst layer. Significant improvement of cell performance has been achieved by introducing ionomer in the catalyst layer. The ratio between the catalyst area covered by ionomer to catalyst area contacting the electrical support is very important. In an extreme case the entire catalyst surface may be covered by a thin ionomer layer, excepting some allowance for electrical contact. Pioneering work was done by Raistrick and co-workers [21] who first introduced Nafion$^{®}$ into the catalyst layer by impregnating it with a Nafion$^{®}$ solution. The loading of platinum required was greatly reduced by this method without lowering cell performance. *Zawodzinski et al.* have shown that there is an optimum amount of ionomer in the catalyst layer around 30% by weight [22]. Because humidified gases are used the catalyst layer must be sufficiently hydrophobic in order to prevent the pores from flooding. This hydrophobicity can be provided by introducing PTFE as a binder, in combination with Nafion$^{®}$.

Currently state of the art catalysts utilize nano-sized platinum particles (4 nm or smaller) finely dispersed on the surface of carbon powder with mesoporous area (> 75 m^2 g^{-1}) [23]. While platinum provides the catalytic activity, the carbon provides the electrical

conductivity necessary to harvest or deliver electrons to the active sites. Generally, the metal active surface should be maximized, for which the Pt content should be as small as possible. The key to improving the PEM fuel cell performance is not in increasing the Pt loading, but rather in increasing Pt utilization in the catalyst layer. The carbon-supported platinum (Pt/C) structure offers a high catalytic surface area, significantly reducing the required platinum loading (generally less than 0.5 mg Pt cm^{-2}). The high surface area carbon support is susceptible to corrosive processes limiting the lifetime of the cathode, and Pt catalyst have been suspected to accelerate the rate of carbon corrosion under conditions relevant for fuel cells [42].

The required metal loading is determined by the amount of catalyst per active area and the ionomer content of the electrode. It can vary between 5-20 weight percent, depending on the application requirements.

2.1.2.2 Membranes

In a PEFC an ion exchange polymer membrane functions as an electrolyte offering a path for the ionic species and separating the reactants from each other. In order to be a suitable candidate for the fuel cell the membrane should conform to several requirements set by the operating principle of a fuel cell combined with the aggressive operating environment. The essential requirements for polymer membrane electrolyte materials include:

- ✓ chemical and electrochemical stability under the fuel cell operating conditions
- ✓ low gravimetric and volumetric water-uptake from water vapour and liquid water and stable dimensions over a range of operating conditions. In currently used membranes the proton conductivity depends significantly on the membrane water content
- ✓ high mechanical strength and durability with low dependency on water-uptake
- ✓ low gas permeability of the membrane and high proton conductivity combined with low area resistance, a value of $0.18 \, \Omega \, cm^2$ has been suggested for the membrane at the operating temperature of the cell [14, 24]
- ✓ low cost and good recyclability

Perfluorosulfonic acid membranes, in particular Nafion® produced by DuPont [25], have been the material of choice and the technology standard in PEMFC for many years. Its chemical homologues have been developed and sold as either a commercial product by other manufacturers such as Asahi Glass (Flemion) Asahi Chemical (Aciplex) or Dow Chemical, and more recently Solvay-Solexis (Hyflon). W. L. Gore & Associates have developed a composite membrane made up of a Teflon-like material providing mechanical strength and PFSA component providing proton conductivity [16]. Another type of existing polymer membranes contains inorganic additives, i.e. polysiloxanes [26], and zirconium phosphates [27]. Some of the possible advantages of incorporating inorganic compounds into composite membranes include enhanced proton conductivity, water retention at high temperatures and mechanical support.

The high cost of the fluorinated polymers urges the development of alternative proton-conducting polymers, such as nonfluorinated ionically, covalently and covalet-ionically cross-linked polyaryl-blend membranes [28, 29, 30]. The commercially available membranes show good performance under moderate conditions, considerable deterioration in the conductivity and the mechanical strength takes place above the glass transition temperature (ca. 110°C), which makes them unavailable for the use in mid-temperature fuel cells.

Chemical degradation mechanism in a fuel cell environment is also an important issue that plays a significantly role for the fuel cell membrane [31, 32]. However, there are also activities to develop new proton conducting polymers, e.g. based on polyaromatic high-performance polymers.

2.2   Nafion, a commercial proton exchange membrane

2.2.1   Background

A majority of commercially available proton exchange fuel cell systems today use the Nafion[®] polymer as a fuel cell membrane [33]. The chemical structure of Nafion[®] is shown in Fig. 3. As can be seen, Nafion[®] membranes consists of polytetrafluoroethylene (PTFE) backbones with a fully fluorinated pendant chains terminated with a sulfonic acid group.
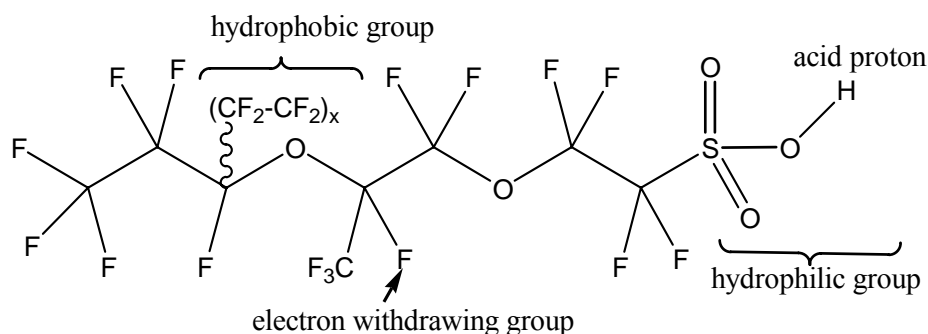

Figure 3: Chemical structure of Nafion[®] [34].

Nafion[®] is prepared by the free radical copolymerization of tetrafluoroethylene and the sulfonated comonomer. The ratio of polar to nonpolar material in the membrane is defined in terms of its equivalent weight (EW), which is the mass of dry polymer (in grams) which contains 1 mol of sulfonate groups. About 13 mol % of the vinyl ether containing a pendant sulfonyl fluoride is employed to afford the best equivalent weight for fuel cell applications (usually 1100 meq/g). The sulfonyl fluoride is subsequently hydrolyzed to the sulfonic acid once the polymer has been converted to the membrane form.

Nafion[®] has many characteristics that make it suitable for use as a membrane in fuel cells, most importantly, when hydrated it exhibits high intrinsic proton conductivity and it is chemically and electrochemically stable in an acidic oxidizing environment. One reason for the high ion conductivity is that, at low-temperatures and high relative humidity, Nafion[®] conducts protons very efficiently, with about 87 mS cm^{-1} (data for Nafion[®] 112) [35, 36]. In order to reduce the Ohmic losses in the fuel cell DuPont

produces a set of Nafion® membranes with different thicknesses - Nafion® 112, 115 and 117. The third digit in the code-name denotes the membrane thickness in mils. Nafion® 112 (50 μm thick) presents the lowest Ohmic loss. Recently, DuPont has introduced an even thinner membrane, Nafion® 111 (25 μm). However, such ultra-thin membranes begin to present significant problems including increased reactant-gas cross-over, reducing the cell potential and the mechanical stability, and leading to poor resistance and to hot-spots.

Nafion®-based membranes show high proton conductivity and chemical stability when operated in a water-swollen state. This means that in order to ensure high performance of a fuel cell, vast amounts of water have to be provided and handled by a complex water-management subsystem. The mechanical and temperature stability of the commercial perfluorosulfonic acid based membranes has considerably improved during the last years. From a fuel cell system point of view the dependence on a constant level of humidification of the feed gases is still a permanent cause of instability and a main reason for the reduced long term stability of existing stacks. Proton conductivity of standard Nafion® at 30% relative humidity (RH) is less than 10% of the value at 80% RH (Fig. 4).
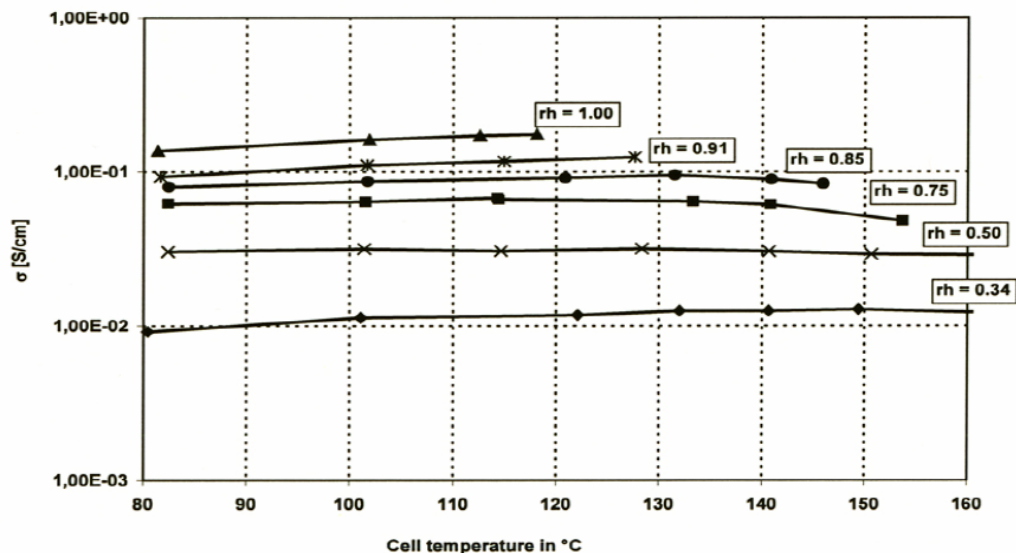

Figure 4: Conductivity of Nafion® 117 as a function of temperature / relative humidity [37].

26

Furthermore, PFSA-based membranes lose mechanical strength at temperatures above 80 °C particularly under the plasticizing influence of water in the polymer, thereby seriously reducing the durability of the membrane and the fuel cell far below the automotive industries target of approximately 5500 h fuel cell operation within 10 years of vehicle operation. This is similarly true for the chemical degradation of the polymer, e.g. by peroxyl-radical attack [31]. However, mechanical as well as chemical failure mechanisms are still poorly understood and in consequence also require investigation.

2.2.2 Morphological characterization

It is well known that Nafion® is not a homogeneous material, but in the presence of water consists of phase-segregated hydrophilic and hydrophobic regions [4]. Over the last 10 years, a wealth of morphological information has been reported in an attempt to define precisely the structure of Nafion® in a variety of physical states. The proposed structural models were based on results of X-ray and neutron small angle scattering. These techniques allow investigating the membrane complex structure at different scales: from angstroms to micrometers [38].

One of the first detailed studies was performed by Gierke *et al.* [39]. Based on small angle X-ray scattering (SAXS) investigations the authors suggested that the morphology of Nafion® consists of ionic sulfonate clusters that are approximately spherical in shape and resemble reverse micelles of 4 nm diameter.
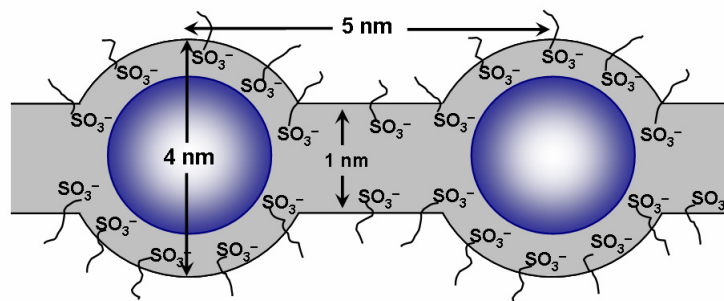
Figure 5: The Gierke cluster-network model of hydrated Nafion® [39].

These structures were thought to be connected by 1 nm channels lined with sulfonate groups that permit the migration of protons or positive ions (see Fig. 5) [40, 41]. This model has endured for many years as a conceptual basis for rationalizing the properties of Nafion® membranes, especially ion transport and permselectivity [42].

Mauritz and Moore have reviewed the extensive experimental database on the morphology of Nafion® membranes [4]. In the past several decades there have been many modifications of this simple explanation [43 - 48]. Gebel *et al.* proposed a conceptual description for the membrane swelling and dissolution process. When the water content decreases, the structure becomes similar to that proposed by Gierke. At very high water content there is a "structure inversion" and the membrane dissolves into a colloidal solution of rodlike particles [48]. Yeager and Steck proposed a three-phase model based on their studies of the diffusion of various ions [49]. This model is significantly different from that of Gierke *et al.* The clusters do not have a strict geometrical definition and their geometrical distribution has a lower degree of order. Most importantly, there are transitional interphases between hydrophilic and hydrophilic regions. Roche and co-workers studied the morphology of Nafion® membranes in the acid and neutralized forms with a range of water contents [50, 51]. In order to highlight the scattering features of the water swollen ionic domains the authors used contrast matching methods of small angle neutron scattering (SANS). According to the Yeager model a crystalline phase, ionic clusters, and an inhomogeneous matrix phase were found. This concept is becoming increasingly accepted. Additionally, the organization of crystalline domains in Nafion® was investigated by Starkweather using X-ray diffraction analysis [52]. The authors developed a model for the crystalline structure of perfluorosulfonate ionomers which consist of a bilayer of hexagonally packed planar zigzag chains with the side chains extending outward on both sides into the clusters.

The best available small angle X-ray scattering (SAXS) data were recently reanalyzed by Schmidt-Rohr and Chen [53]. Using arguments of symmetry, the authors described the proton conducting network in Nafion® as cylindrical channels with diameters between 1.8 and 3.5 nm, which are parallel-oriented over ca. 100 nm but random on a larger length scale. The strong molecular interactions between the polymeric backbones make the cylindrical walls stiff and stable. Moreover, the locally aligned polymer matrix is able to swell perpendicular to the bundle direction when water is sorbed. The ions can thus diffuse easily in this tubular nanostructure. This model is in agreement with the observed

variation of the scattering intensity as a function of the amount of contained water and could allow for the anisotropic optical and mechanical properties.

With respect to the morphological characterization of Nafion[®], it is important to note that the information obtained using a variety of scattering methods is inherently indirect and is limited by the fact that Nafion[®] yields only a single, broad SAXS scattering maximum on a sloping background that is attributed to characteristic dimensions of the ionic domains. Additional reflections obtained with normal X-ray diffraction are broad and relatively weak due to low degrees of crystallinity of PTFE-like crystallites in Nafion[®]. Consequently, it has proven difficult to obtain a detailed view on the nm scale of the distribution of active channels and clusters on the membrane surface using such techniques as TEM, X-ray scattering and SEM.

2.2.3   AFM measurements in tapping and phase imaging mode

High-resolution imaging of the ionic and crystal domains in Nafion[®] was achieved using tapping mode atomic force microscopy (AFM) and phase imaging AFM methods. It was demonstrated that in the unswollen membrane under ambient humidity conditions, domains in the size range of 4-10 nm are present. When the membranes were soaked in water, domains of 7-15 nm were observed and the domains developed a more continuous character, forming large channels of an ion rich phase [54]. The first study of the surface ionic activity of Nafion[®] was carried out by Bard's group using electrochemical scanning microscopy [55]. More recently, O'Hayre *et al.* applied an AFM impedance imaging technique to evaluate the ionically active domains [56]. Hydrophilic domains with a size on the order of several hundred nanometers were resolved. Buratto *et al.* reported that a large fraction of the proton channels at the surface of a Nafion[®] membrane are inactive [57]. Furthermore, Nguyen *et al.* found that the ion conductivity distribution vs. current follows approximately a Gaussian function, with the peak and half width values increasing exponentially with relative humidity [58].

While the exact morphology of the water containing regions in the ionomer is still under debate it is clear that there is a continuous aqueous network containing sulfonic acid groups, which is responsible for its unique ion transport properties.

For improving performance in PEFCs, the current density distribution on all scales is of high interest. For this purpose local probes (such as atomic force microscopy, AFM) have proven to be powerful tools.

2.2.4   Swelling properties and water management

Water management is the most critical issue for high proton conductivity in Nafion® [59]. Generally, the water present in the membrane is considered to exist in different states, such as strongly bound to the sulfonate group, weakly bound, and free. The water profile across the membrane is governed by the water diffusion coefficient and the electro-osmotic drag coefficient. When water fills the pore network, the number of water molecules transferred through the membrane is approximately 3 per proton and increases with increasing water content and increasing temperature [60]. This effect becomes more pronounced at high current densities, while the proton current through the membrane leads to cathode flooding and depletion of water at the anode, resulting in an increased membrane resistance, which can seriously reduce PEMFC performance [61]. The drag coefficients increase also with temperature due to diminishing water-polymer interactions. Moreover, flooding can also take place at lower current densities, if the gas flow rate and temperature (i.e. equilibrium vapor pressure) are low. One way of improving the water management is to control the humidity of the gases. With appropriate stack design, liquid water accumulated in the cathode can be drawn across the membrane to the anode by a concentration gradient, and removed in the fuel stream. This method of water management, "anode water removal", can significantly reduce parasitic loads associated with the oxidant side of the fuel cell, and results in a totally new approach to fuel cell system design. Another type of water management can be found in the direct hydration of the membrane by mounting porous fibre wicks [62, 63].

The water content in the membrane is usually expressed as grams of water per gram of polymer dry weight, or as a number of water molecules per sulfonic acid groups present in the polymer. Water uptake results in the membrane swelling and changes its dimensions, which is a significant factor for fuel cell design. For Nafion® the dimensional changes are in the order of magnitude of 10%.

2.3   Proton conductivity

2.3.1   Fundamentals

Proton conductivity is one of the key properties of a polymer electrolyte membrane. It strongly impacts the fuel cell performance in terms of Ohmic loss. Experimentally, it is well established that ion conductivity in polymer membranes based on sulfonic acid groups is strongly dependent on the ion exchange capacity and the ability to take in water [64, 65]. Also, the external conditions, for example temperature and water activity, influence the membrane conductivity [66].

Generally, water is needed to solvate the protons from the acid groups, where they are bound by electrostatic forces, while the number of the sulfonic acid groups as well as the interactions between themselves and with the water molecules affect the formation of hydrophilic channels, through which the protons are transported [67]. At low water contents not all acid groups are dissociated and the interaction among water molecules via hydrogen bonding is low, resulting in a low rate of proton transfer, which is limited primarily to the surface region. At high water contents the properties of water in Nafion[®] approach those of bulk water, so that proton mobility in fully hydrated membrane is only one order of magnitude lower than the proton mobility in aqueous sulfuric acid solution. It is reported that dry Nafion[®] equilibrate with liquid water can absorb as much as 22 water molecules per sulfonic group, whereas the maximum water uptake from the vapour phase is about 14 water molecules per sulfonic group [68]. Kreuer *et al.* demonstrated the significance of the phase separation in Nafion[®] in providing a better-connected hydrophilic network within the ionomer for enhanced proton diffusion. Based on a comparison with a homogeneously sulfonated polyaromatic ionomer, it was shown that the phase separation in the Nafion[®] membrane produced an order of magnitude enhancement in both proton and water mobility. In general, the proton mobility can be enhanced by the change of the size of hydrophilic channels in the membrane [69, 70]. However, raising the sulfonic acid content to too high values can compromise the mechanical properties of the membrane, allowing it to absorb too much water [4].

2.3.2 Proton conduction mechanisms

Due to the inability of experiments to directly observe the dynamics of the conductive domains at the molecular level, the transport of protons and water in a proton exchange membrane has been modeled by numerous groups at various levels of complexity [71, 72]. Here, the predominant Nafion[®] conductivity was also assumed to be a consequence of the extensive nano-phase separation [54, 73, 74]. Taking into account the morphological descriptions of Gierke *et al.* many authors modeled the transport phenomena of water and protons within cylindrical single pore of fixed geometry [75]. Simulation studies have included calculations of the role of side chains of Nafion in effecting proton transfer [69, 76], molecular dynamics (MD) simulations of hydrated Nafion[®] [77 - 79], mesoscale modeling of the morphology of the hydrated membrane, and statistical mechanics modeling of Nafion pores [80, 81]. All of this theoretical work reflects the multiscale nature of transport processes in polymer membranes.

Kreuer *et al.* have reviewed transport in proton conductors for fuel cell applications with changes in the level of hydration [82]. Two principal mechanisms describe proton diffusion in the following way:

- at high water content protons move by transferring within hydrogen bonds from one water molecule group to another, the hopping or Grotthus mechanism becomes dominant [83, 84]. In this case, there is a pronounced local dynamics of the proton environment, which in addition includes a reorientation of water molecules. This results in the formation of an uninterrupted path for proton migration.

- at low hydration levels most of the water molecules and H_3O^+ hydronium ions are bound to the sulfonate groups and protons migrate by the vehicle or "surface" transport mechanism i.e. that they are transported through the membrane attached to water molecules. The relevant rate for the observed conductivity is that of vehicle diffusion. When the protons are located close to the pore surface they experience Coulomb energy barriers for transport along the aqueous/polymer interface in the membrane network. This mechanism is a significantly activated process and proton transport is therefore slower [85].

However, these two systems may be viewed as limiting or extreme cases in the range of hydration of the polymer. In practice, the transport of protons in a hydrated polymer is considerably more complex due to the heterogeneous nature of the polymer and the nano-confinement of the water around $-SO_3^-$ groups.

Because of the complexity of hydrated PEMs, a fully molecular theoretical treatment of proton transport is impractical. The Grotthus transport mechanism has been incorporated into the atomistic description of aqueous pores in the network by using a simplified empirical valence bond model, which allows the systematic variation of thermodynamic conditions (water content, temperature) and also material properties such as SO_3H-group density.

In most studies, the proton-transfer process was modeled quantum mechanically, where proton transport involves both Grotthus and vehicular diffusion of hydronium ions.

Since the conductivity increases with temperature, protons are transported faster. At higher temperatures the hydrogen bonding between the water molecules becomes weaker, rendering the proton hopping involved in the Grotthus mechanism less favourable and, consequently, increasing the contribution of the vehicle mechanism to the proton transport. The results showed that the activation energy of proton transport was independent of water content down to a $\lambda = 4$ (i.e. 4 water molecules per sulfonate group). It was then speculated that the experimentally observed increase of Activation Energy (AE) could be due to fluctuative bridging or, more generally, changes in polymer structure, which would lead to a higher AE as a consequence of a change of the rate-determining step from elementary proton-hopping of structural diffusion to the formation of an aqueous bridge.

Paddison and Elliott have concluded that proton transfer to water is possible at a hydration of less than three water molecules per sulfonate when two sulfonate groups are present close to each other in contrast to the three water molecules needed when sulfonate groups are far apart [71].

Additionally, the effect of partial dehydration of the proton-conducting membrane was simulated by Eikerling et al. [86]. The obtained current-voltage plots demonstrate the existence of a critical current at which the potential drop across the membrane increases dramatically due to membrane dehydration, in particular near the anode.

The way in which the nano-phase-separated regions interact and act upon other substances is of great interest.

34

2.3.3 Macroscopic conductivity studies

Precise knowledge of the local membrane resistance is key information for understanding and interpretation of current density distributions. There are several well-known and broadly used methods for macroscopic conductivity measurements such as electrochemical impedance spectroscopy (EIS) of fuel cell stacks [87-89] and their components [90], current interruption [91] and four-point probe measurements [92]. Among the wide range of experimental possibilities EIS has the ability to differentiate between the contributions of each individual component, such as the membrane and the gas diffusion electrode, to fuel cell performance. The obtained information is only meaningful if the parameters of interest can be assumed homogeneous over the cell. However, transport inhomogeneities are strongly amplified when a high power is drawn from the cell. It is conceivable that the EIS-relevant information differs greatly along the flow field channels between the inlet and the outlet of the gases. Recently, Scherer *et al.* developed a cell with a segmented cathode plate and used it for simultaneous recording of conductivity on a fuel cell under operating conditions [93]. It was demonstrated that the membrane resistance increased with decreasing humidity. This method has the advantage that there is no time delay of the information between the segments, and therefore the data are less affected by drifts.

Compared to EIS the current interruption method has the advantage of relatively straightforward data analysis [94]. But, there are some difficulties in precise separation of the Ohmic and activation losses. In contrast, four-point probe measurements provide precise data for the proton conductivity of the membrane, eliminating the interfacial effects between PEM and electrode which are typical for the *in situ* methods.

The macroscopic proton conductivity has been investigated for different humidities and various temperatures. It was shown that the specific conductivity of the membrane is not only determined by the mobility of the ions, but largely by the interaction of the ions with water and with the microscopic membrane channel structure [95]. In addition, a variety of environments has been employed, including $1 M H_2SO_4$, water vapor, and humidified gases at temperatures from 20 to 95 °C. The impact of such a wide range of factors on the conductivity of the Nafion membranes has resulted in a wide range of

published proton conductivities. These existing conductivity data reflect the importance of the handling and pretreatment of the membrane.

Taking into account the membrane thickness l [cm] and following Ohm's law, the specific conductivity σ [S cm^{-1}] can be determined:

$$\sigma = \kappa \cdot l \tag{2-5}$$

Anantaraman and Gardner made conductivity measurements on Nafion$^{®}$ using a coaxial probe reflectance technique [96]. They found a sharp upturn in conductivity near 100% relative humidity, indicating that those last molecules of loosely bound water play an important role in determining high conductivity at high water contents.

Another set of experiments was performed where the membranes were exposed to a humidity gradient. Zawodzinski *et al.* compared transport properties focused on protonic conductivity, diffusion coefficient of water, and electro-osmotic drag coefficient. It was shown that increasing the water content of a membrane lead to an increase of the conductivity.

The production of the polymer membranes with optimum performance requires a detailed knowledge of the nanoscopic chemical structure as well as a molecular level view of proton transport inside the membrane. It was shown that macroscopic proton conductivity strongly depends on the pretreatment of the membrane and the operating parameters [97, 98].

Thus the effects of temperature and relative humidity on ionic conductivities of the membranes were measured in a two-electrode cell, where the membrane was squeezed between Pt electrodes of 3 mm in diameter. The complete impedance spectra were recorded in the frequency range of 1 to 900 kHz while the range of 5 to 85 kHz was typically utilized to evaluate the resistance of a membrane by extrapolating the data in the Nyquist plot to the real axis. The conductivity was calculated from this resistance, the thickness of the membrane, and the area of the electrodes [99].

The membrane conductivity above certain values of temperature and relative humidity was investigated by two-probe impedance measurements under controlled applied pressure on the electrodes by Alberti *et al.* [100, 101].

2.4   Atomic Force Microscopy

2.4.1   Theoretical Background

Atomic force microscopy (AFM) is a specific member of the family of scanning probe microscopy (SPM). It was first developed in 1985 [102]. The invention of the AFM solved one of the most intriguing problems in surface science: it is able to image surfaces with high spatial resolution. The rapid propagation and continued success of SPM in laboratories around the world led to the award of the Nobel Prize in Physics to Binnig and Rohrer in 1986.

The AFM can be compared to the electron beam techniques, such as the SEM or TEM but they are both quite limited in the surface properties to which they are sensitive. Furthermore, the length scale of an AFM overlaps nicely with the SAXS/SANS spectroscopy. Fig. 6 shows the comparison between the length scales of several imaging techniques. Often, AFM is combined with an optical microscope and with this combination it is possible to have a field of view from mm to nm.
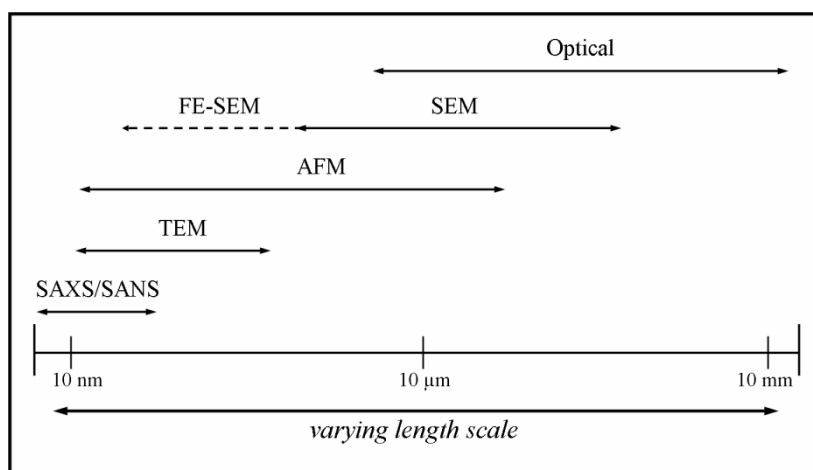

Figure 6: Comparison of the imaging length scale. AFM can resolve features in the dimensions of a few nanometers with scan ranges up to a hundred micrometers. [103].

The AFM is able to measure far more than surface topography. It is possible to observe almost any physically phenomena at the nanometer scale such as conductivity, dielectric constant, magnetization, and others, through the use of suitably chosen probes and signal processing.

37

2.4.2   Operation modes

In atomic force microscopy there are three main operating modes to image and characterize a sample: contact, non-contact and intermittent-contact modes. All of them are based on the same working principle: a sharp tip (typically silicon or silicon nitride) scans over the surface of interest and the final topography, adhesion or stiffness map is created of point-by-point measurements of the interaction between tip and sample. In contact mode the deflection of the cantilever is measured, and in vibrating mode the changes in frequency and amplitude are used to measure the force interaction. The different modes operate in distinct force regimes as can be seen in Fig. 7.
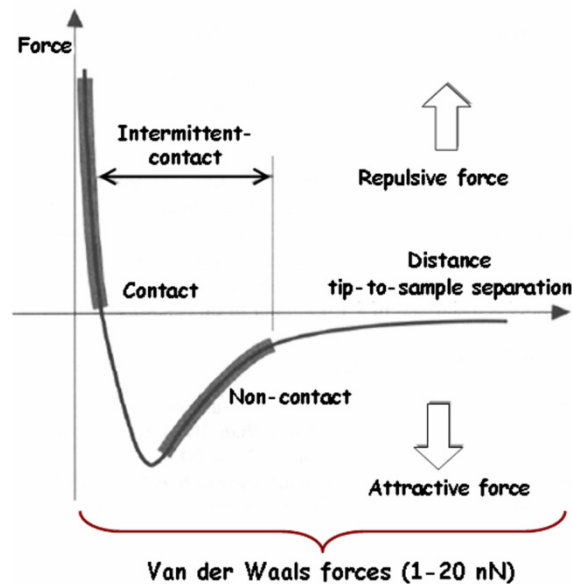
**Figure 7:** Lennard-Jones potential [104].

This behavior can be associated with specific ranges of the Lennard-Jones potential. The potential is only dependent on the distance between the molecules or atoms and is described as:

$$V = -E_m \left\{ \left(\frac{r_m}{r} \right)^{12} - 2 \left(\frac{r_m}{r} \right)^{6} \right\}$$

(2-9)

where E_m is the depth of the potential well and r_m is the distance at the minimum of the potential at which the interparticle potential is zero and r is the distance between the particles. The $\left(\dfrac{1}{r}\right)^{12}$ term describes repulsion and the $\left(\dfrac{1}{r}\right)^{6}$ term describes attraction.

2.4.2.1 Contact mode

In contact (repulsive) mode an AFM tip is always in soft physical contact with the sample. Fig. 8 illustrates the block diagram of an atomic force microscope. Here, the force between the tip and the surface is measured with a force sensor, the output of the force sensor is then sent to a feedback controller that drives a Z motion generator.
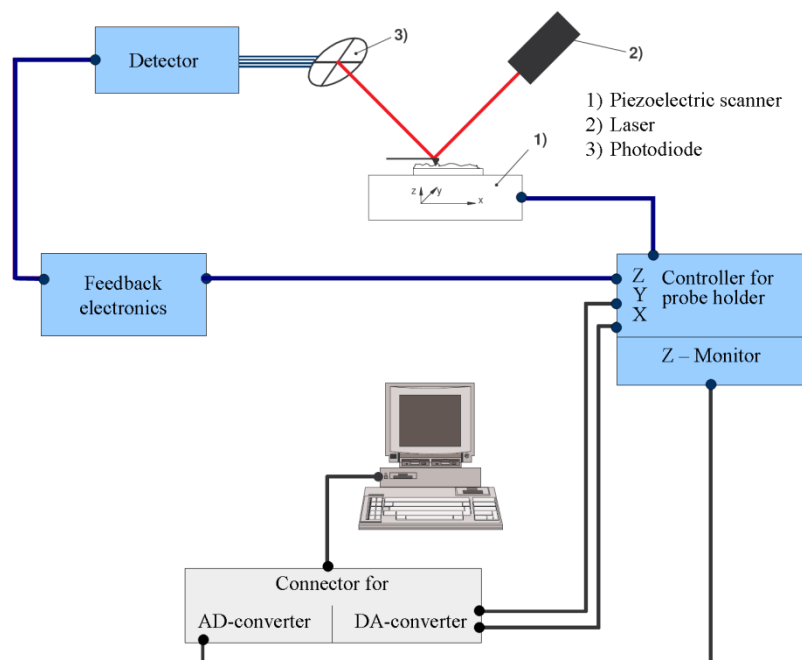
Figure 8: Basic block diagram of an experimental setup for constant force mode. The feedback control system is represented in blue. The force between the tip and the surface is kept constant during scanning by maintaining a constant deflection [103].

The feedback controller uses the force sensor output to maintain a fixed distance between the probe and the sample. X-Y motion generators move the probe over the surface in the X and Y axis. The motion of the probe is monitored and used to create an image of the surface. A feedback mechanism is employed to adjust the tip-to-sample distance to maintain a constant force between the tip and the sample. Traditionally, the sample is mounted on a piezoelectric tube, which can move the sample in the z direction for maintaining a constant force, and the x and y directions for scanning the sample. As the scanner gently traces the sample under the tip, the contact force causes the cantilever to bend to detect changes in topography. Typically, the deflection is measured using a laser spot reflected from the top of the cantilever into an array of photodiodes.

The forces applied to the surface by the probe in contact mode are given by Hooks law:

$$F = -k \cdot D \tag{2-10}$$

where k is the force constant and D is the deflection distance. Depending on the situation, forces that are measured in AFM include mechanical contact force, Van der Waals forces, capillary forces, chemical bonding, electrostatic forces, magnetic forces etc.

In contact mode, the cantilever is scanned over a surface at a fixed deflection, and a constant force is applied to the surface while scanning. If the tip were scanned at a constant height, there would be a risk that the tip would collide with the surface, causing damage.

The slope of the van der Waals curve is very steep in the repulsive or contact regime. As a result, the repulsive van der Waals force balances almost any force that attempts to push the atoms closer together. In AFM this means that when the cantilever pushes the tip against the sample, the cantilever bends rather than forcing the tip atoms closer to the sample atoms. Even if one designs a very stiff cantilever to exert large forces on the sample, the interatomic separation between the tip and sample atoms is unlikely to decrease much. Instead, the sample surface is likely to deform.

In addition to the repulsive van der Waals force described above, two other forces are generally present during contact AFM operation: a capillary force exerted by the thin water layer often present in an ambient environment, and the force exerted by the cantilever itself. The capillary force arises when water wicks its way around the tip, applying a strong attractive force (about 10^{-8} N) that holds the tip in contact with the surface. The magnitude of the capillary force depends upon the tip-to-sample separation.

The force exerted by the cantilever is like the force of a compressed spring. The magnitude and sign (repulsive or attractive) of the cantilever force depends upon the deflection of the cantilever and upon its spring constant.

As long as the tip is in contact with the sample, the capillary force should be constant. It is also assumed that the water layer is reasonably homogeneous. The variable force in contact AFM is the force exerted by the cantilever. The total force that the tip exerts on the sample is the sum of the capillary plus cantilever forces, and must be balanced by the repulsive van der Waals force for contact AFM. The magnitude of the total force exerted on the sample varies from 10^{-8} N (with the cantilever pulling away from the sample almost as hard as the water is pulling down the tip - see Force vs. distance curves), to the more typical operating range of 10^{-7} to 10^{-6} N.

In the present work, the microscope is based on the tip-sample interaction forces which are a function of the tip-sample distance. To map the three-dimensional surface topography (x,y,z), the tip is raster scanned along x and y over the surface and the interaction force is measured at each raster point. The measured force can be used to map the surface topography qualitatively or fed into a feedback circuit to map the surface topography quantitatively. In the second mode, the tip-sample distance is controlled and the force between tip and sample remains constant.

The Electrochemical Atomic Force Microscopy (ECAFM) is not just suitable to measure local topography but also, and more importantly, represents a tool to map local electrochemical reactivity, to induce localized electrochemical surface modifications, or to investigate heterogeneous and homogeneous kinetics.

Electrochemical AFM is a variant of AFM, where a sharp conducting tip is able to map simultaneously the topography and conductivity of a surface with high spatial resolution [105, 106].

Chapter 3

3   EXPERIMENTAL METHODS

3.1   Description of experiments

All experiments were performed using a commercial AFM [Nanoscope III, Digital Instruments (DI), Santa Barbara, USA] equipped with an electrochemical cell and a potentiostat used as a voltage source. All experiments and ECAFM measurements were performed at the University of Applied Science, Esslingen. The AFM instrument can be used in ambient air, in vacuum and also in a liquid. The probe head was equipped with a sample scanner that facilitates a maximum scan range of 10×10 µm. A closed fluid cell was employed for all measurements. Electrical contact was provided via metal spring clamps of a commercial fluid cell holder (DI) which rested on the Pt covered probe.

The contact force between the AFM tip and the sample was typically in the range of 5-20 nN. The current was measured via the conductive AFM cantilever (25 nm layer of platinum coating on both sides of the probe, spring constant $k = 0.2$ N m^{-1}, NanoWorld®) and a homebuilt current amplifier (0.5-10 MΩ) Fig. 9. It was recorded directly via an auxiliary input using a signal access module (DI) that allows the simultaneous acquisition of current and topographical data by the AFM microscope.

The obtained AFM images (512 x 512 pixels) were processed with the NanoScope software and with the programs WSxM and Matlab version [107].

Rectangular cantilevers with integrated Pt coated tips and force constants of ~0.06 N m^{-1} were used (NanoWorld®, 25 nm platinum layer). Scanning was performed at ~1.5 Hz in the topographic and conductive mode at a minimum loading force typically in the low 10-15 nN range.
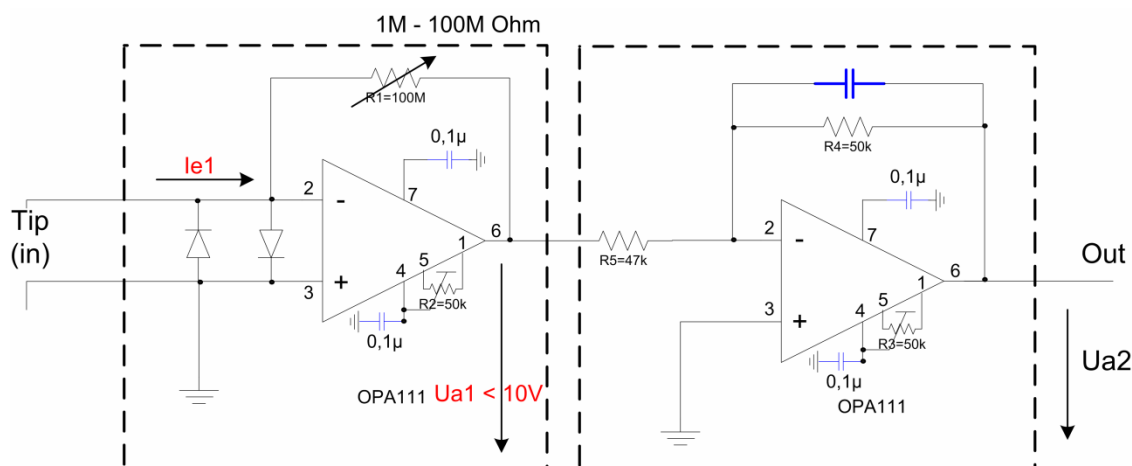
Figure 9: Basic block diagram of an experimental homebuilt current amplifier.

All experiments were performed on a single-side coated Nafion® 112 membrane. The electrode consists of commercial Pt catalyst (1.0 mg cm^{-2}). This back Pt-electrode served as anode. Measurements on the uncoated membrane surface are obtained by moving the Pt-coated AFM probe in contact mode. It served as a counter electrode (cathode) necessary for conductivity measurements and as a probe of surface morphology. The atmosphere is identical on both sides of the membrane and consists of air at well-defined humidity that is held constant in a climate chamber. A voltage is applied that makes the cantilever tip the cathode and the catalyst layer the anode. In this setup the anode reaction is water oxidation. The protons take their way through the membrane, where they neutralize at the electrode and in principle form hydrogen, but in presence of oxygen this yields directly water via the normal fuel cell oxygen reduction reaction at the cathode. This and the additional water that is transported to the cathode by osmotic drag is evaporated by the considerable heat of reaction of water formation. It prevents that a water droplet builds up at the AFM tip that would have a detrimental effect on resolution. The applied voltage has to exceed the threshold value that is determined by the activation of the electrode reactions, ca. 0.7 V for the given set-up.

I-t-curves were measured with a fixed tip position on the conductive area, and the data were recorded directly on a PC equipped with data acquisition card (*Lab-PCI-6035E, National Instruments Corp. Ltd., U.K.*) using software written in-house. The measurement was normally started by recording a topographic image. The applied voltage could be changed when the AFM tip was positioned on top of a conductive area

on the sample, and the feedback control was switched off. At the end of the measurement the voltages were set to their original values and the automatic control was switched on again.

At present two kinds of force sensors are available, the cantilever and needle sensor, the latter is generally referred to as the tuning fork. Cantilevers are typically made out of silicon and silicon nitride, whereas the tuning fork is made out of quartz. In this work only rectangular cantilevers were used.

Force-versus-distance curve

The force-distance curves can be used to measure the long range attractive or repulsive forces between the probe tip and the sample surface, elucidating local chemical and mechanical properties like adhesion and even thickness of adsorbed layers. Force-versus-distance curves show the deflection of the free end of the AFM cantilever as the fixed end of the cantilever is brought vertically towards and then away from the sample surface. This technique provides information from the amount of force acting on the cantilever as the probe tip is brought close to a sample surface [108].

In Fig. 10 the blue horizontal line represents the starting line before the tip is in contact with the surface. As the tip is brought very close to the surface, it jumps (due to the high humidity) into contact with the membrane (black line). Once the tip is in contact with the surface, cantilever deflection increases and the force is raising proportional to the traveling way of the tip (the slope is linear). After having pushed the cantilever down up to a desired force value, the process is reversed. A key measurement of the AFM force curve is the point at which the adhesion is broken and the cantilever comes free from the surface. This can be used to measure the rupture force required to break chemical bonds or the magnitude of adhesion forces. There is a clear difference in the path of the curve during lowering and retracting the tip, besides the final jump caused by an adhesion force. At the end the tip again reaches the initial position.
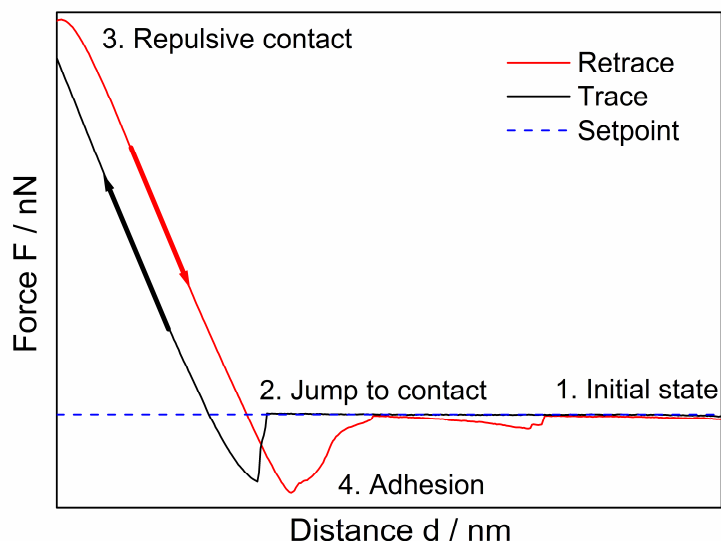
Figure 10: Original force versus distance curve as observed by AFM at the Nafion surface and the corresponding cantilever deflections during approach and retraction.

Force measurements were used to demonstrate similarly capillary forces for samples in reduced humidity or high humidity environments.

3.2 Membrane preparation

Generally, there are two ways of preparation of a membrane electrode assembly. The first way is to deposit the catalyst layer onto the porous substrate (gas diffusion layer) typically carbon cloth, and then hot-press it to the membrane. The second method is application of the catalyst directly onto the membrane. A gas diffusion layer may be added later in a process of stack assembly.

The membrane consisted of Nafion 112 and was coated with commercial Pt-catalyst (1.0 mg cm^{-2}) dissolved in a mixture of 20% Polytetrafluorethylen (PTFE), applied by the dry layer preparation method at the German Aerospace Center (DLR, Stuttgart) on the side opposite to the AFM probe [109]. In practice, the thickness of the catalyst layer is about 10 μm.

3.3   Electrochemical Atomic Force Microscopy

3.3.1   Measuring principle

Probe head and cell were kept in an environmental chamber with controlled humidity as the only source of water during measurements. The experimental setup is shown in Fig. 11.
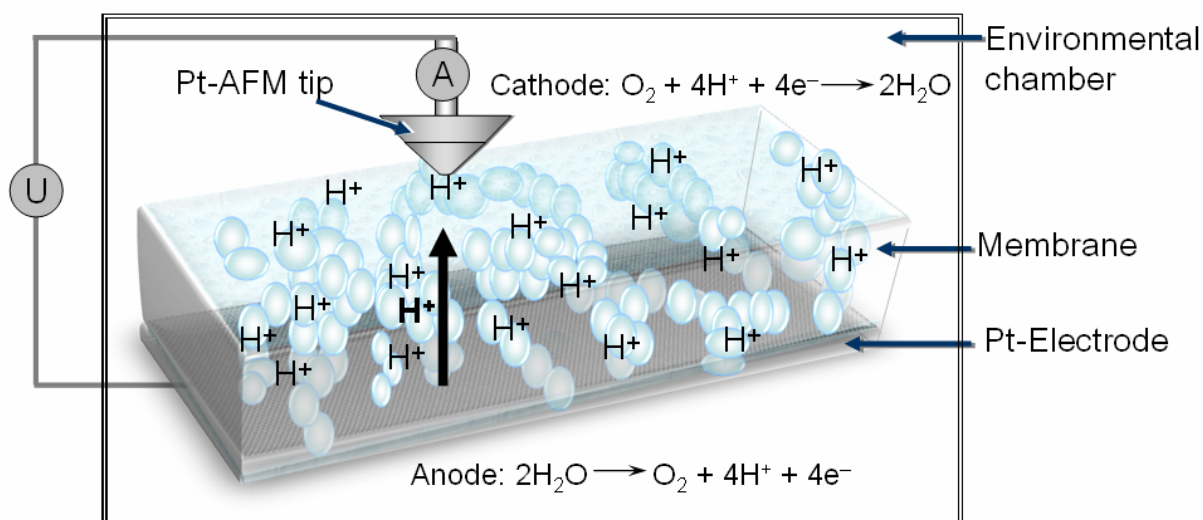
Figure 11: *In-situ* method for measurement of the proton conductivity in the Nafion$^{®}$ membrane using electrochemical AFM. The applied voltage induces water oxidation at the anode. The protons are transported through the membrane when the conductive AFM tip contacts an ion channel. These protons are used for the oxygen reduction reaction at the AFM tip [110].

Both electrodes were exposed to the same atmosphere. The catalyst-covered side of the membrane served as the anode, the Pt-coated conductive AFM tip as the cathode. When the supplied voltage is stepped up and exceeds a certain value, water starts to be oxidized at the anode under evolution of oxygen. At the same time, protons are set free. When the tip is located on top of a proton conductive channel, the protons are transported through the channels to the cathode whereas the electrons travel through the electric curcuit. At the cathode they recombine with oxygen and the protons back to water. Because water formation is exothermic, the product water is vaporized. When the tip is located on the

hydrophobic phase, nearly no current is measured. In the absence of hydrogen fuel gas the process corresponds to water electrolysis which goes along with hydrogen production at the cathode. However, in a humidity and temperature controlled air atmosphere the hydrogen at the cathode recombines with the abundant oxygen before it is set free from the catalyst surface. The necessary energy to split water and to cross the activation barrier imposed by the anode overpotential, is provided by the voltage that is applied by the potentiostat, while the heat generated by the formation of water at the cathode is dissipated.

This and the additional water that is transported to the cathode by osmotic drag is evaporated by the considerable heat of reaction of water formation (-241.8 kJ/mol). It prevents that a water droplet builds up at the AFM tip that would have a detrimental effect on resolution.

An electrochemical current is detected only when the EC-AFM tip on the membrane surface is in contact with a proton conductive area that is connected to the ionic network in the membrane. No current is measured in contact with hydrophobic regions, and only a transient one in case of isolated acidic water clusters.

Fig. 12 shows a photo of the environmental chamber and the fluid cell of the AFM.
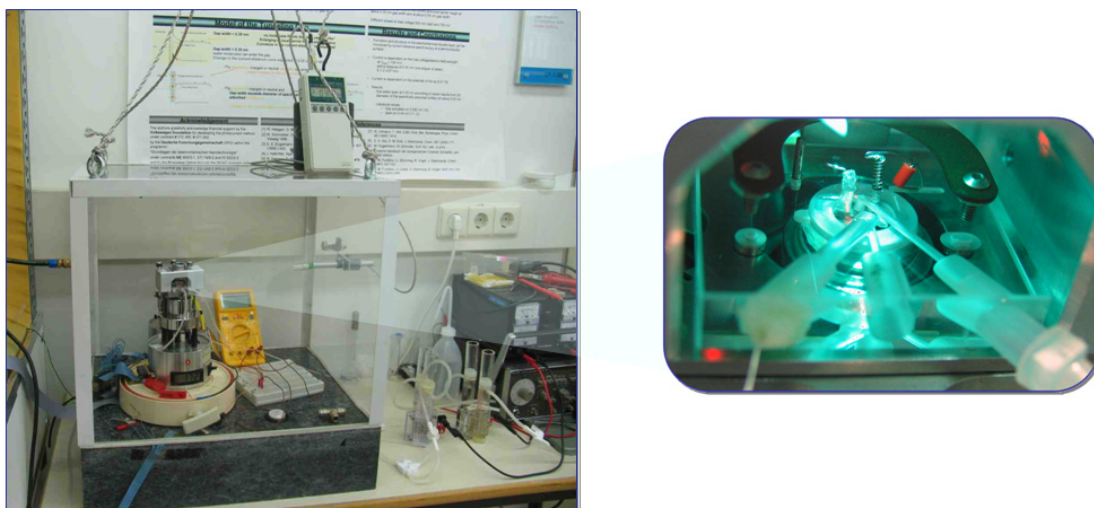
Figure 12: Experimental setup for the electrochemical AFM conductivity measurements. ECAFM measurements were performed at the University of Applied Science Esslingen

Chapter 4

4   RESULTS AND DISCUSSION

In this chapter experimental results are presented. The experimental data are discussed in the first two subchapters, whereas the time dependent measurements are discussed at the end of the chapter.

4.1   Time dependence of current

4.1.1   *I-t*-curves

All experiments have been conducted by keeping the Pt-tip in the contact with a conductive area of the Nafion® membrane. The experiment is understood best by inspection of the response following a potential step, as displayed for a typical example in Fig. 11a, where the voltage at the anode is stepped from +1.33 V to +1.63 V. This leads to an immediate current increase, reaching I_{max} = 0.7 nA and then decaying over approximately 1.3 s with a half-life of 0.3 s to a constant value (steady-state current $I_{DC} \cong$ 0.07 nA). This time constant is large compared to the case of a conventional, flat, free Pt electrode. It shows that its origin is not related to a reversal of the electrical double layer and indicates that diffusion processes are involved. A convection-free diffusion layer is enforced by the presence of the conductive network in the Nafion® membrane which has a thickness of 50 µm in the present case. For comparison, diffusional proton transport in bulk water would take 0.2 s for a root-mean-square displacement that corresponds to the membrane thickness. However, the entire ionic network that is connected to the monitored ion channel is involved in water transport through the membrane so that the influence of the membrane network effective path length must exceed the membrane thickness significantly. A second complication in comparison with the situation of a conventional set-up using flat, free Pt electrodes relates to the fact that the anions are

49

bound to the Nafion polyelectrolyte and cannot adjust to a changing proton concentration to maintain electro-neutrality. The consequence of this needs further investigation.
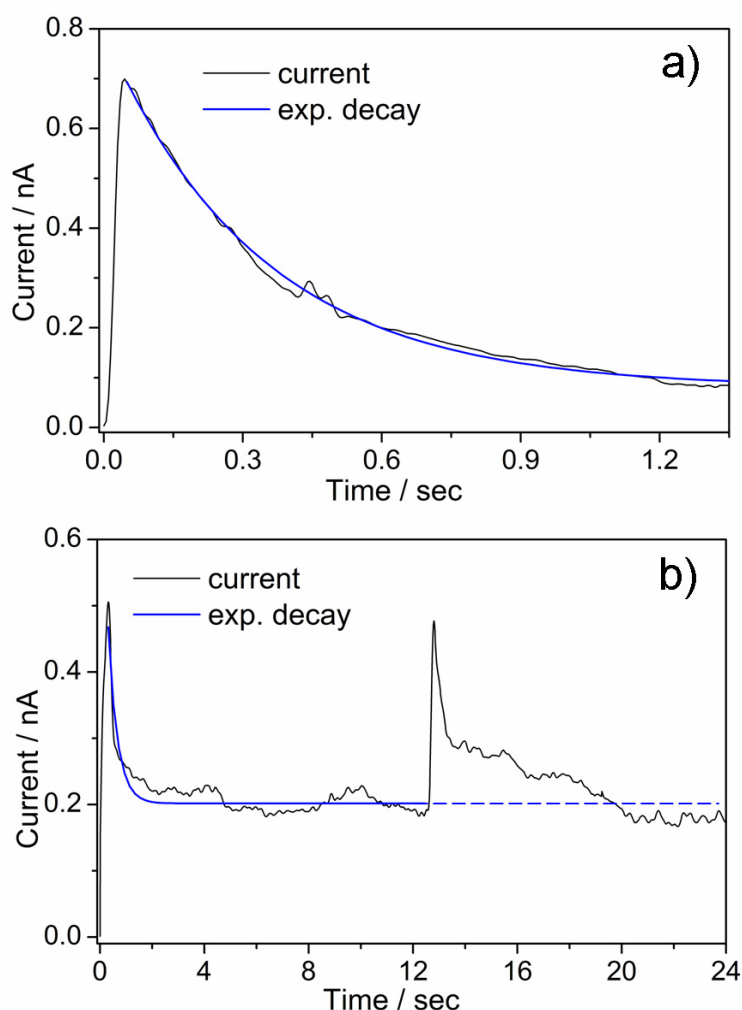
Figure 13: a) Time dependent current following a voltage step from +1.3 V to +1.6 V. The corresponding decay over 1.3 s is exponential with a half-life of 0.3 s; $I_{DC} = 0.07$ nA. b) Time dependent current after the potential step displayed over 12 s with a half-life of 0.3 s and $I_{DC} = 0.2$ nA. The measurements were done at relative humidity of 58% [118].

Fig. 13b) shows measurements at a different position on the membrane and over longer time intervals in the range of approximately 12 s between two subsequent potential steps. After the first voltage step the current curve over the first 1.5 s corresponds to an exponential decay with a half-life of 0.3 s, as in Fig. 13a), but in this case the peak and the steady state currents amount to $I_{max} = 0.5$ nA and $I_{DC} \cong 0.2$ nA, respectively. From the diagram it is clearly seen that I_{DC} remains almost constant, apart from small current

alterations which may be explained by a membrane drift, initiated by the enhanced proton and water transport and the dispersal of product water in the membrane network. The differences between Fig. 13a) and 13b) can be explained by the structural inhomogeneity of the ionic network inside the membrane. In particular, the different DC components mean that the proton conductivity depends on the location of the membrane surface. After the second voltage step in Fig. 13b) the changes in water and proton concentration exert a considerable influence on the current behavior. In this case, the decay is more distorted, suggesting a superposition of different factors, including local water and proton diffusion through the channels and membrane drift. However, both the peak and the steady state currents adopt the same value as in the first decay. From further experiments it looks as if there is some systematics in the increasing irregularities following the first, second and further decays, but it is too early to draw conclusions from this behavior.
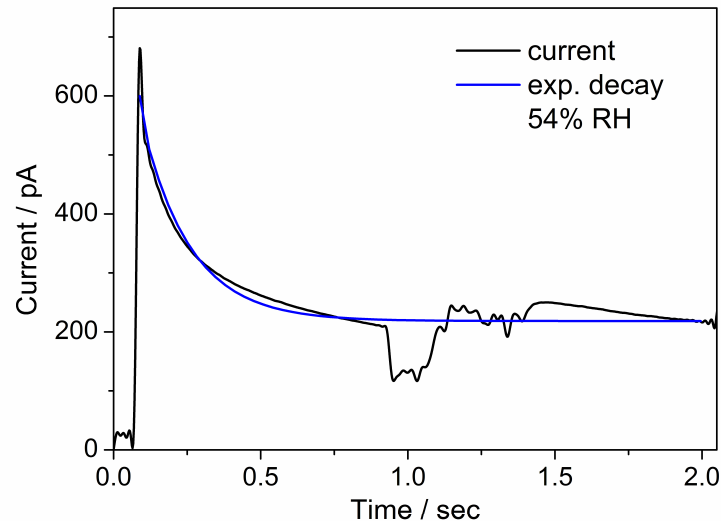
Figure 14: Time dependent current following a voltage step from 0 V to +0.8 V. The corresponding decay over 2.0 s is exponential with a half-life of 0.3 s; I_{max} = 0.7 nA, I_{DC} = 0.2 nA [110].

Furthermore, it was observed that a measured current depends on the time spent on top of a scanned conductive area. In order to understand the process involved an *I-t*-curve was measured (Figure 14). The voltage at the anode is stepped from +0.0 V to +0.8 V, which leads to an immediate current increase, reaching I_{max} = 0.7 nA and then decaying over approximately 2 s with a half-life of 0.3 s to a constant value (I_{DC} = 0.2 nA). Current

51

alterations may be explained by a membrane drift, initiated by the enhanced proton and water transport and the dispersal of product water in the membrane network. The obtained information is very important for the calculation of average pore conductivity and may also be used as input for detailed theoretical modelling of proton conductivity.

4.1.2 Prediction of the channel size based on the calculated pH-value

Presumably, also the heat generation at the AFM tip can contribute significantly to inhomogeneities during operation. The heat of reaction is estimated by integration of the transient current in Fig. 13a, which gives 1.6×10^9 electrons, corresponding to the formation of 8×10^8 molecules or 1.34×10^{-15} mol of water over a time interval of 1.3 s. Based on the standard enthalpy of formation, $\Delta_f H^0(H_2O, \text{liquid}) = -285$ kJ mol^{-1}, this corresponds to an energy of ca. -0.38 nJ. This energy is sufficient to heat up 6×10^{12} water molecules by 50° which, for comparison, is the water volume in a channel of 10 nm radius and 0.6 μm length. Some of the heat of reaction will of course be dissipated by conduction through the AFM cantilever, and perhaps another fraction is used to evaporate water and lead to local changes of humidity. It is conceivable that such effects contribute to the current instabilities which were discussed above. The above integral of the transient current means that 1.6×10^9 protons have been discharged at the cathode. On the basis that there are about 10 water molecules per proton in the channels of Nafion, these protons represent a reservoir of 1.6×10^{10} water molecules or a water volume of 4.8×10^8 nm^3. If we place this water in channels of 10 nm radius, as assumed above, this volume corresponds to a length of 1500 μm or 30 times the thickness of the membrane! On a macroscopic basis at a current density on the order of 1 A cm^{-2} all protons in the membrane are exchanged approximately once a second [111].

The measured current is proportional to the local proton concentration at the AFM tip. The decrease after a voltage step thus corresponds to the build-up of a concentration gradient over the membrane. Indeed, the diffusion time across the 50 μm membrane is on the order of the decay time, based on the proton diffusion coefficient in bulk water,

which is actually known to be a good approximation [85]. Thus, the first part of the decay curve represents the local response of the proton conducting network and should be understood as hemispherical proton diffusion into a point sink (the AFM tip), while the stationary value invokes the protons which are generated continuously at a flat source (the electrode) opposite to the AFM tip. In this context it is of interest that the protons represented by a transient decay can be counted. For the top panel of Fig. 13 a) these are 0.27 nC, or 1.6×10^9 protons, which is roughly 1000 times all the protons which are contained in a single cylindrical straight pore of 4 nm diameter through the entire membrane. This demonstrates that proton conductivity does not occur through single straight pores; rather, it has to involve an extended network within the membrane. Furthermore, since the anionic charges of the sulfonic acid groups are bound to the backbone and held in place, the depletion of a membrane domain by 10^9 protons demonstrates that charge neutrality is severely violated and that large capacitive potentials build up before proton production at the anode sets in and leads to a steady state. In this context, the local dielectric constant plays an important role. In sufficiently hydrated moieties it may be close to its bulk value ($\varepsilon = 81$) which can shield charges on a length scale of 0.7 nm, whereas in the hydrophobic fluorocarbon regimes with $\varepsilon \approx 2$ the length scale for shielding increases by a factor of 40.

The peak current represents the local equilibrium proton concentration $[H^+]$, which is quite well known for the given content of acid groups and of water in the membrane. A typical value for ambient humidity is 10 M (pH = -1, corresponding to λ=10). We use the following two definitions for the conductivity σ:

$$\sigma = \frac{\ell}{AR} = \frac{\ell I}{AU} \qquad\qquad \sigma = [H^+]\Lambda_{H+} \qquad\qquad (1)$$

where ℓ is the length of the conductor (here the thickness of the membrane, 50 μm) and A its area (the cross section of the conducting pore). R is the resistance, which for Ohmic behavior can be replaced by U/I (the voltage divided by the current). The alternative definition relates σ to the proton concentration and the proton equivalent conduction, Λ_{H+} = 350 cm^2 Ω^{-1} mol^{-1} (the value for bulk water at 298 K). Setting the two definitions equal and solving for the pore cross section we obtain 7.8 nm for the apparent diameter

of a cylindrical pore from the upper panel of Fig. 13 a), and 5.9 and 6.4 nm from those of the lower panel. The same numbers are obtained when the calculation is based on the value of the stationary current, since the local proton concentration scales down by the same factor. These pore diameters exceed the range derived from the most extensive and recent analysis of scattering experiments by Schmidt-Rohr, who quotes 1.8 − 3.5 nm [53]. It is not excluded that the present measurements sometimes reflect the unresolved conductivities of small bundles of channels, but it should also be stressed that the present analysis is approximate; nevertheless it gives further support and credibility to the extent of understanding of the experiment.

4.2 Imaging and characterization of ionically active regions

Figure 15 shows two examples at different magnification of the topography of the Nafion[®] membrane which were recorded at a relative humidity of 58% simultaneously with the corresponding current images. The shown areas are 330×500 nm^2 and 2×3 µm^2.

The topographical and current images were stable under constant humidity and voltage despite continuous scanning at 1.5 Hz per line. The 1.5 Hz scan rate has no pronounced influence on the image quality, the shape and size of individual pores. The images are very sensitive to changes in the voltage and the humidity, as the membrane expands both vertically and laterally, due to swelling or drying out. The expansion of Nafion[®] has been reported previously by several authors using macroscopic studies [112, 113]. It was therefore essential to maintain stable conditions in experiments monitoring the same membrane area.
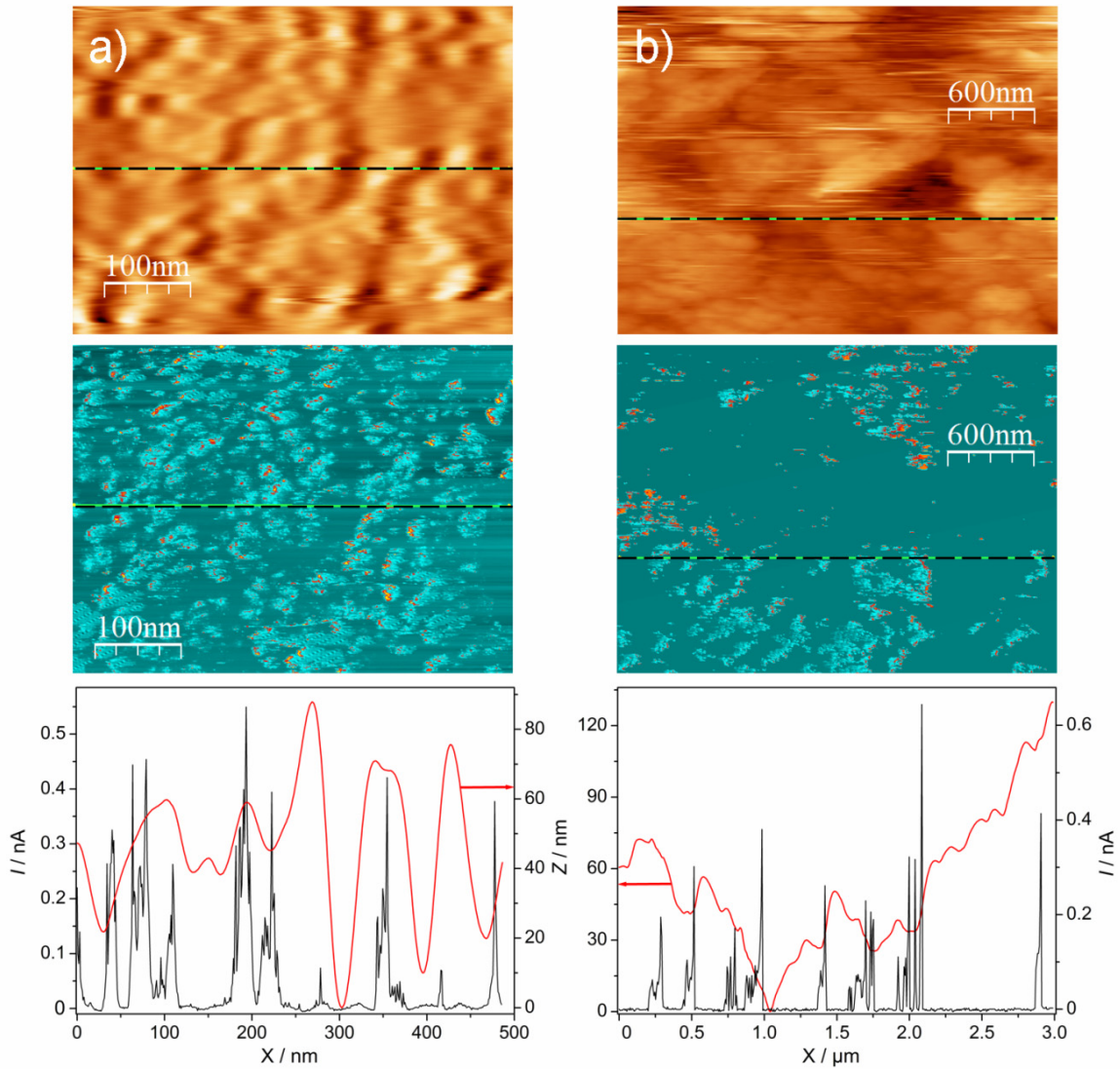
Figure 15: Simultaneously recorded AFM topography (upper) and current (middle) images of the Nafion 112 membrane coated from one side with 1.0 mg cm^{-2} Pt catalyst (scan rate = 1.5 Hz, RH = 58%, scan size: a) 330×500 nm^2, and b) 2×3 μm^2 (307×512 pixels)); and line profiles of topographic (red) and current (black) images [118].

From the observed topographical image (Fig. 15 upper images) hydrophilic and hydrophobic domains cannot be distinguished. Comparison with the simultaneously recorded current images permits to identify ionically conductive regions (Fig. 15, middle images). The bright areas in the current image indicate where a current flow is detected. The red dots correspond to the maximum detected current on the surface. These areas are directly related to ion rich regions at the membrane surface which are connected to the ionic network in the membrane body, and the dark areas are attributed to hydrophobic

regions. From the current image it is clearly seen that there is a marked heterogeneity in the conductivity. The conductive regions reflect the ends of channel structures with a diameter of 9-25 nm in width, which agrees well with the interpretation of tapping mode AFM studies of hydrated Nafion[114, 115]. A small fraction of conductive regions has a cluster size in the range of about 40 nm. They probably correspond to a collapsed form of ionomer channels that was suggested recently [116]. Zooming into one of these large conductive clusters reveals that it consists of an agglomerate of smaller channels which are incompletely resolved. On a larger scale the conductive regions sometimes display a rope-like structure, but not all of them are connected with each other at the surface. In contrast, the maximum distances at the surface between the conductive areas are in the range of 60 - 80 nm. The narrowest current peaks have a diameter of ca. 10 nm, which could be interpreted as the actual resolution limit of the tip or already the width of the narrowest channels. The distance between the conductive areas in the 2 x 3 μm^2 current image is ca. 1 μm, which is inconceivably large. According to the Nafion there must be many SO_3^- groups in this area, but at lower RH they are probably not connected to the ionic network in the membrane.

In general, there is no lateral ion conductivity across the hydrophobic barriers at the membrane surface, even at high relative humidity. Based on the present measurements it was verified that at a RH of 58% only 63% of the membrane area contributes to the conductivity. To obtain optimal fuel cell performance most of the active catalyst particles should be in contact with the aqueous nanoponds at the surface so that a Pt/water/fuel-gas three phase boundary can be formed.

Line profiles across both images (broken line) are shown in the lower part of Fig. 15. Analysed data suggest that there is no simple correlation between the structures observed in the current image and topographical features. This may have been expected because the topography represents the morphological features of the surface, which depends on the membrane manufacturing process. The cross-section analysis of these structures demonstrates that the conductive regions have a mean diameter of approximately 20 nm, which corresponds to the ion cluster size at the surface of the Nafion membranes.

4.3   Distribution of the conductive regions

4.3.1   Analysis of conductivity image

The conductivity image shown in Fig. 16 was recorded at an applied voltage of +0.9 V in humidified air at 53% RH. The conductivity image shows enormous lateral inhomogeneities. The distance between conductive areas is in a range of up to 900 nm.
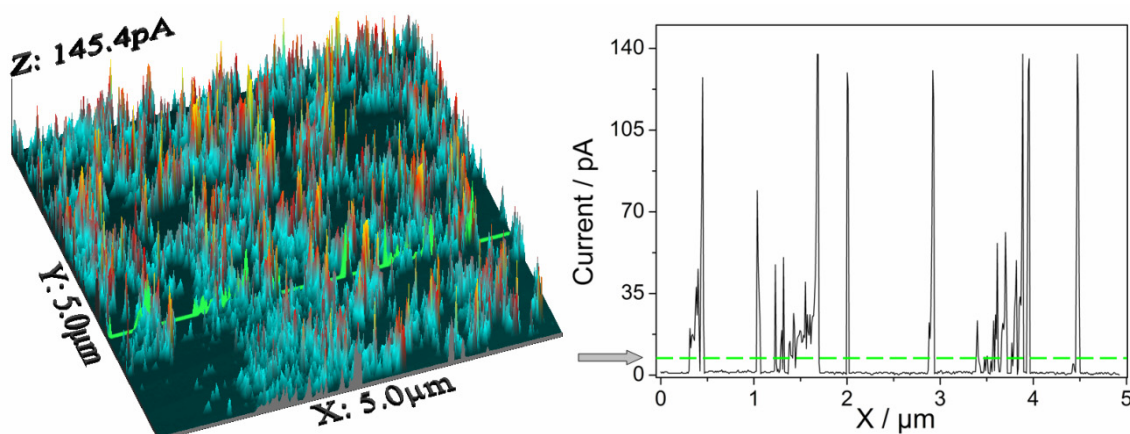
Figure 16: A typical 3-D current image obtained at 53% RH, applied voltage of 0.9 V, scan rate of 1.5 Hz (left) and current profile along the bright line in the conductivity image (right). For further analysis a threshold (shown as a dotted line in the profile) was chosen at 10 pA [117].

The important information can be more easily seen from the current profile across the image (marked as a dotted green line). The significant current peaks are separated by gaps with essentially zero conductivity. As mentioned before, it is not conceivable that there are no sulfonic acid groups in this area. According to the nanostructure of the Nafion polymer the average spacing between neighboring sulfonic acid groups is only about 4 nm. This means that a large fraction of acid groups is inactive in these non-conducting regions and does not contribute to the membrane conductivity. Such current inhomogeneities may give rise to enhanced local dissipation of heat of reaction that may lead to 'hot spots' at places with very high reactant turnover, which can accelerate membrane degradation [5].

57

The low conductivity between peaks demonstrates that there is no lateral proton conductivity on the surface of the membrane across these presumably dry, hydrophobic regimes. With fresh membranes it is only at RH >90% that the peaks obtain clear peak shoulders which indicate that a surface water film is formed and in-plane conductivity sets in [110].

Additional experiments showed in-plane conductivity at the polymer surface already at 70% RH. Typically, such behaviour was observed with Nafion membranes which had been used previously and had been stored in water for several days. This can probably be explained by the structural changes due to further water uptake and structure changes of the ionomer.

In order to analyse the distribution of conductive channels resulting from the current image a threshold of 10 pA was chosen (see Fig. 16), just above the background current that was in the range of typically 8 pA (see below). A top-view 500×500 nm^2 image of the lateral current distribution at the cut-off level is displayed in Fig. 17. This image is produced using the Matlab software with the z-scale maximum at 135 pA, which is represented by the yellow/red color. Here, the numerical resolution is only about 10 nm, but the observed conductive areas often exceed this resolution and may represent the unresolved cross section of bundles of pores. It is shown elsewhere that in high resolution images obtained with fresh probe tips structures of the order of a few nanometers can be resolved, suggesting that individual channels can be mapped [130]. Furthermore, the conductive spots shown in the image are not at all circular, rather they are of irregular shape and often a bit elongated in the scanning direction. This elongated shape may indicate a water droplet (which is partly produced at the opening of a conductive channel during the measurement) that the probe tip drags along.

On a larger scale the conductive regions sometimes seem to group to a rope-like structure, although often incompletely connected at the surface. Here, only 39% of the surface area contributes to the conductivity. Of additional significance is the observation that the conductive domains with a smaller diameter (typically in the range of 7–11 nm) conduct higher current values. According to a performed study these high-current regions are distributed extremely inhomogeneously over the membrane surface [117].
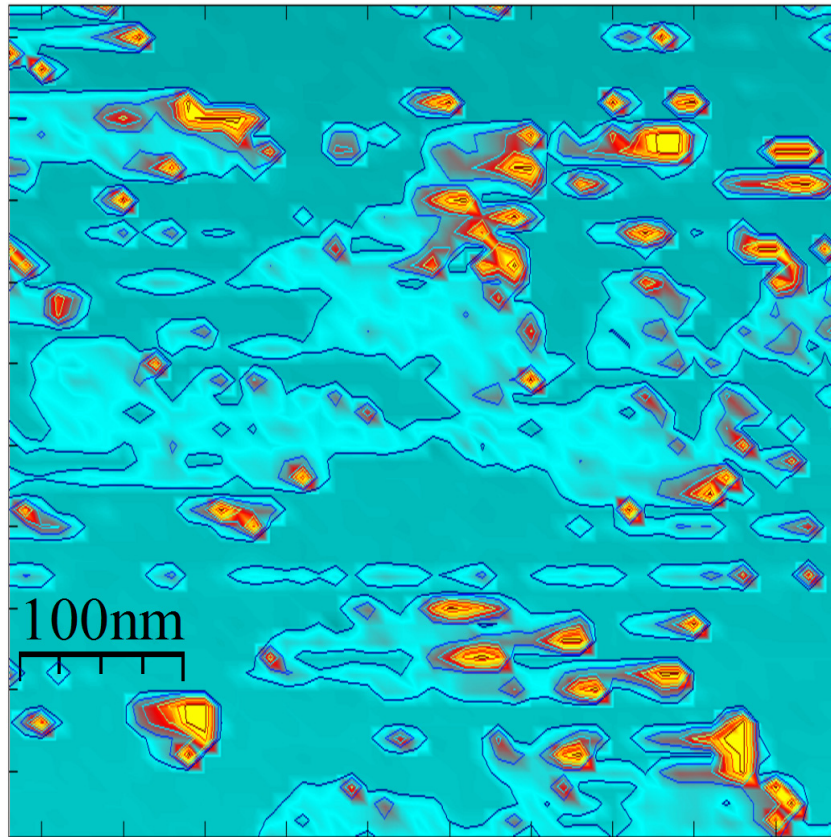
Figure 17: Zoom of ca. 500×500 nm^2 into the conductivity image indicated by the white square in Figure 16. The conductive regimes are represented as contour lines with current values above the threshold shown in Figure 16 with the z-scale maximum 135 pA represented in yellow [117].

The maximum current that is detected per pixel with an area of 95 nm^2 is $\geq$130 pA, which translates into current densities of 137 A cm^{-2}. This is remarkable and suggests that the proton transport in the narrow channels is particularly efficient, indicating a special conduction process. This is partly a transient effect. As was shown previously [118], following a voltage step with the AFM probe on top of the channel, the current relaxes to a steady state which is about one-tenth of the initial peak value, but even the steady-state currents are impressive. This transient behavior was investigated further, and it was found that the maximum current depends on the total time which the AFM probe spends on top of the conductive channel [118]. Obviously, the measurement influences the local conditions which are responsible for conductivity. In this context it is important

also to note that the measured maximum current significantly depends on the applied voltage and on the relative humidity in the environmental chamber.

Another interpretation could be that the current distribution images may reflect nothing but the distribution of catalyst particles at the anode, and the justification that is given is that these catalyst particles have a diameter that is typically below 10 nm, just the same as the conductive spots. This statement is in conflict with the fact that the membrane thickness amounts to 50 μm, which is close to four orders of magnitude larger than the catalyst particles. It is hard to imagine that the channel systems would permit a clear mapping over such a long distance. The 10^9 protons which are contained in a transient curve (Fig. 13a) correspond to all protons in of the order of 1000 straight channels through the membrane. This demonstrates that an extensively connected network exists, as was suggested already by Gierke [42, 39]. The observed fraction of conductive pixels increases strongly with humidity, but the number of catalyst particles does not change.

4.3.2 Effect of relative humidity

A common theme in PEM research is to investigate membrane performance as a function of the level of membrane hydration. Water solvation partially screens the proton charge, thus lowering the activation energy for migration. Therefore, water management and proton conductivity are critical issues for efficient fuel cell operation [119]. In order to investigate the effect of membrane hydration on the conductivity, experiments were performed under well-defined relative humidities. Four 1 μm^2 3-D current images obtained over a humidity range of 40–50% are shown in Fig. 18a) - d). The light blue and yellow-red areas correspond to the current that is plotted in z direction, and the dark areas are related to zero current. The images a) and b) were recorded at different positions on the membrane but under the same conditions and serve to verify the homogeneity over a larger length scale. Indeed, the peak current differs only by 20%. The areas monitored in the images b)-d) are nominally identical, but it is important to note that the changes of the RH cause a strong membrane drift. Nevertheless, certain common structures can still be identified. To indicate the extension of the non-conductive areas the same structure has been circled in the images b)-d). At the lower RH (40% in Fig. 18a) only 28% of the

membrane area is ionically active. At 50% humidity (Fig. 18d) the Nafion membrane is more hydrated, and as much as 53% of the total area contributes to ionic conductivity. These measurements reveal a notable increase of the conductive area with increasing RH and show that the proton conductivity is proportional to the water content of the membrane (Fig. 19). This observation agrees with earlier, macroscopic studies.
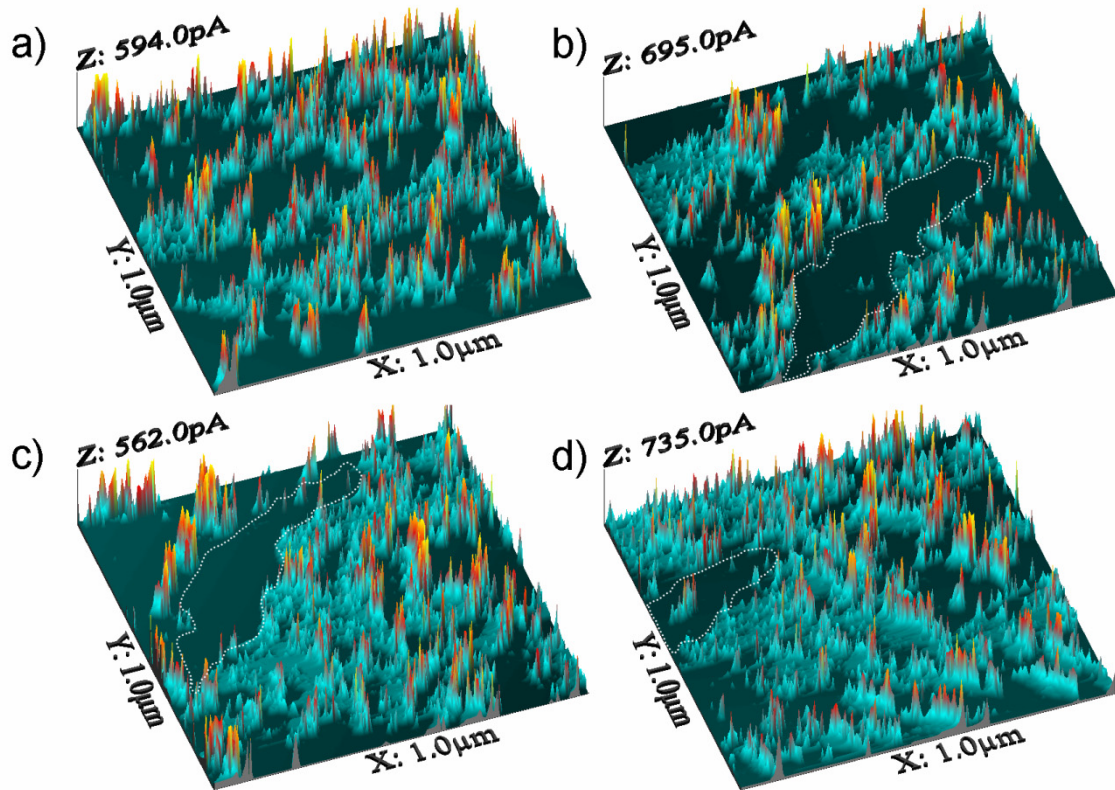
Figure 18: 3D current images of the Nafion 112 membrane recorded at a) 40%; b) 42%; c) 46%; d) 50%. The scan size is 1 μm × 1 μm, and the applied voltage at the lower electrode is 1.55 V relative to the AFM tip [118].

The results indicate that the swelling and redistribution of ionic clusters is a dynamic process. Extrapolation of Fig. 19 shows that the conductivity goes to zero at a RH close to 32% RH, indicating that there is a percolation limit below which the membrane behaves like an insulator. Other work shows that the conductivity at around 30% RH is no longer linear, and in reality it is possible to measure a certain conductivity down to 20% RH [120]. Finally, the number of conductive areas decreases with increasing RH, revealing that some channels expand and merge, leading to a distribution of the SO_3^- groups with fewer clusters in the more hydrated polymer. This is in good agreement with

earlier AFM studies [115]. It was furthermore suggested that at lower hydration levels the structure of the ionic phase is that of an inverted micelle, and percolation of hydrophilic regimes should occur in swollen membranes. However, the precise mechanism of cluster swelling and reorganization on increasing humidity is unknown. The present results can demonstrate only the changes at the membrane surface and bear no information on the spatial reorganization of the ionic network inside the membrane, but the expansion of the conductive channels at the membrane surface with increasing the RH is evident.
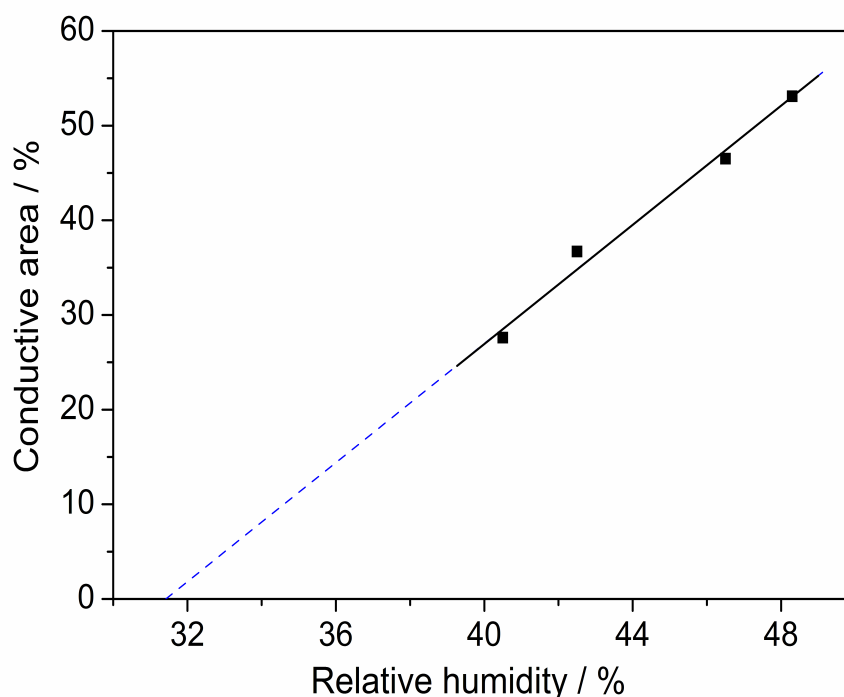
Figure 19: Influence of relative humidity on the size of conductive area (linear fit), for 1 μm^2 current images of Nafion 112 at 40 – 50% RH (evaluation of Fig. 18).

In addition, the effect of relative humidity on the size of conductive areas was investigated at higher RH (Fig. 20). Due to the strong membrane drift at high relative humidity > 90% it was not possible to obtain a stable image. Nevertheless, with increasing relative humidity an increase of the number of conductive areas could be detected. At high RH the increase of conductive area is no longer linear. Moreover it goes into saturation showing strong RH dependence of proton conductivity.
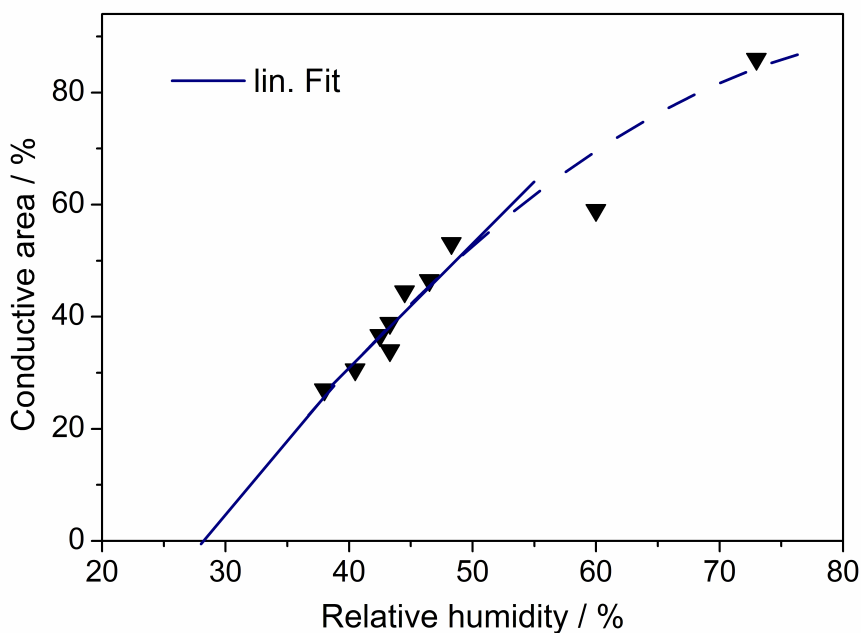
Figure 20: Influence of relative humidity on the size of conductive area.

According to these investigations, the surface conductivity (coming from the formation of the water film on the membrane) appears at 95% RH. This leads to a variation of the current offset. Therefore, the observation of the different current regions and the redistribution of the SO_3^- groups with fewer clusters in the fully hydrated polymer was impossible.

4.3.3   Influence of applied voltage

The electrochemical reactions at the electrodes are generally governed by two main effects: the RH and the potential due to the applied voltage. The measurement influences the local conditions which are responsible for conductivity. In this context it is important also to note that the measured maximum current significantly depends on the applied voltage and on the relative humidity in the environmental chamber. On the one hand, increasing the potential to higher values represents an increase of the driving force for proton transport and leads to an increase of the reaction rates. On the other hand, the proton transfer along the pore is closely related to water transport in the membrane,

because only solvated protons can be transported through the ionic channels (electro-osmotic drag). Consequently, proton transport will be accompanied by a reorganisation of the polymer. In order to observe the expansion of the conductive channels at the membrane surface the applied voltage was varied. Fig. 21 shows representative 3-D current images of the membrane at 48% humidity. The images were scanned using the same cantilever. Unfortunately, smaller areas (500 x 500 nm^2) tend to drift away because of membrane swelling or drying out. With the intent to detect always the same membrane area, the selected scan size was expanded to 3 x 3 μm^2.
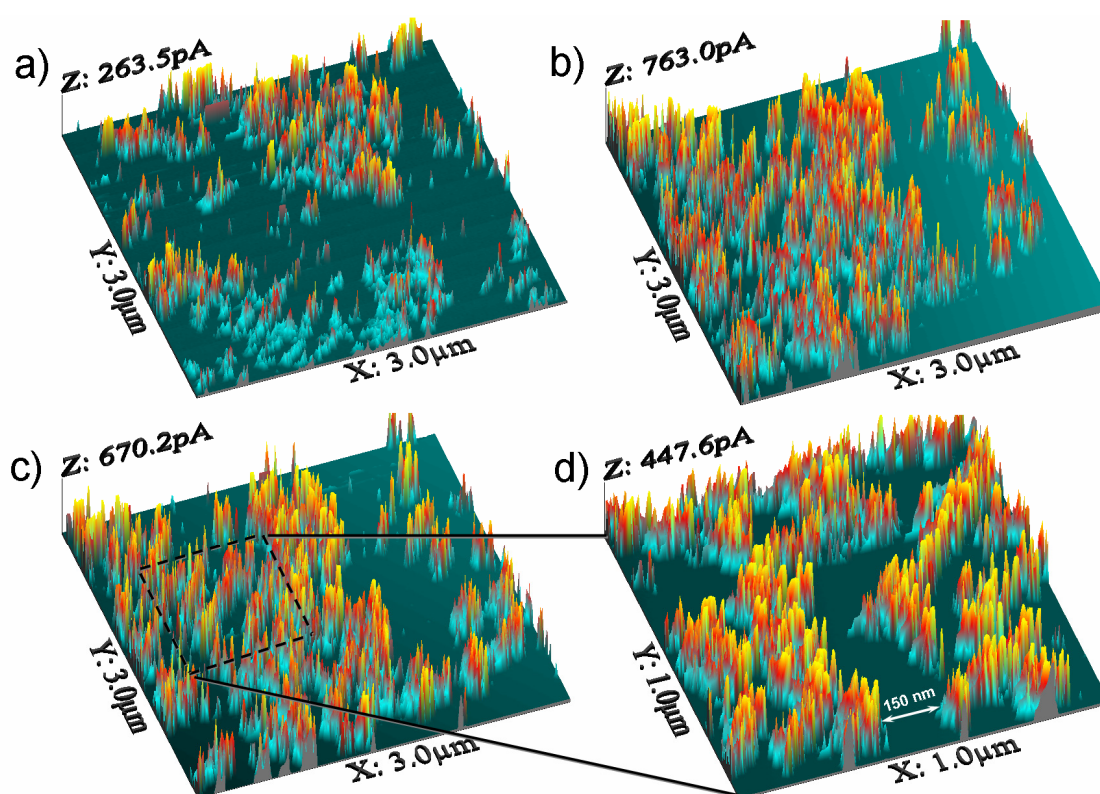
Figure 21: 3D current images of the Nafion 112 membrane recorded at 48% RH, scan size 3 μm × 3 μm, applied voltage at the AFM tip a) +0.7 V; b), c), d) +0.9 V. Image b) is the result after increasing the voltage from +0.7 V to + 0.9 V, nominally at the same position. Image d) represents a zoom into image c) and is an independent measurement [118].

The image represented in Fig. 21 a) was obtained at an applied voltage of +0.7 V relative to the cathode. Here, small conductive areas are evidently separated in distance by more than 1 μm. Fig. 21 b) shows the changes on increasing the voltage to +0.9 V. In contrast

64

to Fig. 21 a) there are clearly more ionically active areas, so that 48% of the membrane surface is now active, compared to 23% in Fig. 21 a). These measurements confirm that additional ionically active channels are formed in areas which were inactive at the lower voltage. The peak current in Fig. 21 b) was measured to be 760 pA, approximately three times more than the value of 230 pA in Fig. 21 a). The repetition of a current image recorded under the same experimental conditions is shown in Fig. 21 c).

The image is reproducible with respect to shape and size of conductive areas which does not vary with time. Furthermore, the connectivity of the pore network persists under constant operating conditions despite a current drop to 670 pA which can probably be explained by a drying out of the anode side. Generally, the reduction of the three-phase boundary could lead to a significant deactivation of active catalyst centers, and the hydration of the protons can be affected as well.

Generally, the current images reveal a consistent structure with relatively ordered domains, with a rope-like organization that is possibly related to a string of polymer backbones. Zooming with AFM into one of these domains reveals the image shown in Fig. 21 d). Here, a non-conductive surface area with a size on the order of 120 to 230 nm^2 is clearly seen.

4.4   Image and current distribution analysis

For further analysis of the conductivity the probability distribution of current values measured for the different pixels was plotted. Fig. 22 provides the evaluation of the images corresponding to the Fig. 21.

At the lower applied voltage of +0.7 V (Fig. 22 a) a pronounced maximum is found at 0.23 nA and a less pronounced and much broader one at 0.02 nA. Upon increasing the voltage to +0.9 V (Fig. 22b) the dominant peak moves to a higher threshold of 0.65 nA. In the repetition of the experiment in Fig. 22 b) this peak comes at 0.58 nA (Fig. 22 c), demonstrating the extent of reproducibility. Fig. 21 d) represents a zoom into Fig. 21 c). It may therefore be confusing that the analysis in Fig. 22 d) is so different from that in Fig. 22 c). However, this is only an artifact of resolution, and for the explanation we refer

back to Fig. 13. The measured current depends on the resting time of the tip at the scanned area.

An important distinction between the two images 22 c) and 22 d) is the different resolution: for 1 mm^2 area in Fig. 22d) we have 2.6 x 10^5 pixels, but in Fig. 22 c) there are only 2.9 x 10^4 pixels. During the measurements, the AFM tip spends in total nine times more time in Fig. 22d) than on the same area in 22 c). Since the channel exits are connected via the ionic network inside the membrane, they are not independent. Drawing current from one exit depletes the concentration partly also in the environment.
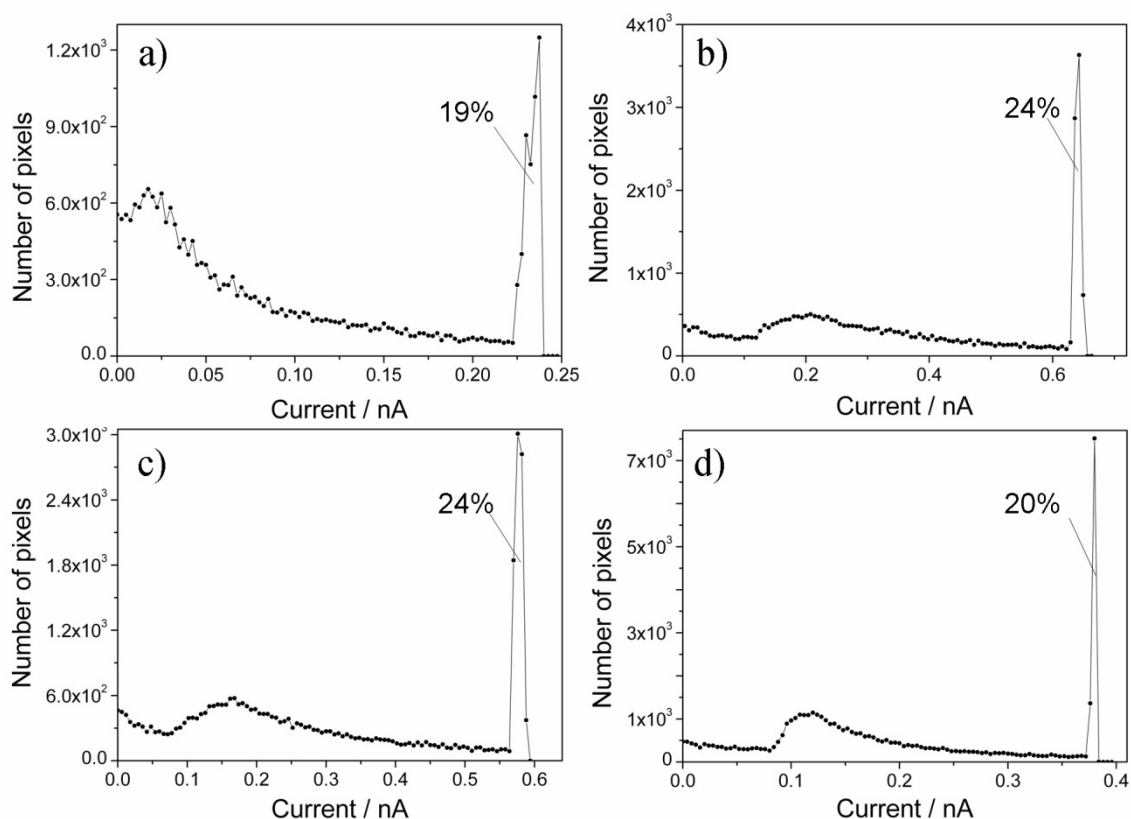
Figure 22: Histograms of number of conductive pixels for the Nafion 112 membrane against current threshold values for the relative humidity of 48% (evaluation of images in Fig. 21). The calculated percentages of the conductive areas for the sharp current peak are indicated [118].

When the AFM tip arrives at the next channel this partial depletion has not yet fully relaxed (from Fig. 13 it was demonstrated that these processes occur on the order of a second), and the measured value is somewhere between I_{max} and I_{DC}. This results in

lower average current values at the higher resolution, which is more easily seen in Fig. 22 than in Fig. 21. Nevertheless, this aspect has no significant influence on the size of the conductive regions.

The extremely sharp peaks in all four probability distributions of Fig. 22 are remarkable and to some extent unexpected for a polymeric material that is normally thought of to be amorphous. This is not an effect of a cut-off by the electronics. The peaks mean that there are a large number of channel ports through which exactly the same proton number per unit time is transported to the surface. This could mean that Nafion forms with a high probability a preferred structure that can conduct exactly a given amount of current. This behavior could be interpreted as a reflection of different conduction processes inside the membrane.

Eikerling *et al.* [121] developed a phenomenological random network model of a microporous proton-exchange membrane (PEM), comparable to the model proposed by Gierke *et al.* [39]. They assumed a hydrated morphology and were able to demonstrate the importance of the connectivity of the pores and the coordination of the water in the pores to the overall conductivity of the membrane. They also found a difference from 'bulk water'. In the center of large pores, proton transport is efficient and based on the Grotthuss mechanism, whereas in small pores which do not contain bulk water protons migrate by the vehicle mechanism via water molecules which are attached to the pore walls, interspersed between the sulfonic acid groups which exert a strong electrostatic attraction.

The origin of the observed peak is not yet entirely clear. The sharp peaks consist not only of a single histogram bin; on an expanded scale it can be resolved into a band which is probably the Gaussian distribution that was reported also by Xie et al [122]. In this experiment the measured current values can be close to the same when the AFM probe contacts any exit of a communicating channel system. It means that the same performance of an extended part of the ionic network is probed at each channel exit. Alternatively, the peak could represent the critical current density that was predicted by Eikerling *et al*. who described the water and ion conduction phenomena occurring within the membrane, including the capillary action and electro-osmotic drag [86]. Their model predicts the water content profiles and the voltage–current plot for medium current densities, which revealed evidence for the existence of a critical current. At this current density a dramatic drop in the water content is predicted near the anode of the membrane.

It was concluded that increasing the proportion of microscopic pores in the membrane could induce an increase of the membrane conductivity. The option of a critical current density will be evaluated in more detail in section 4.5.1.

Generally, water content affects not only the pore distribution on the membrane surface but also the proton transport inside the membrane. In our experiments, the broad current distribution loses importance with decreasing humidity [118]. Only the sharp peak remains, and increasing RH leads to a shift of it to higher values, which probably corresponds to a lower resistance due to the connection of further channels to the conducting polymer network and to the swelling of channels. In theoretical models a similar behavior was explained on the basis of the morphological variations of hydrophilic channels, as proposed in the cluster model [76]. An important conclusion of our measurements is that at a discussed RH the main fraction of ionomer channels conduct approximately the same number of protons per unit time, indicating direct connectivity between measured pores.

Having analyzed the sharp current peak in Fig. 22 it remains to be explained what the remaining fraction in the broad peak and background means. From the 3-D conductivity images it is clearly seen that the conductive area increases with increasing voltage. The calculated percentage of conductive pixels in Fig. 22, which is indicated at the sharp peak, rises only slightly (from 19% in Fig. 22a) to 24% in Fig. 22b,c) and the ratio between the background and sharp peaks remains almost constant. This observation indicates that the entire network swells and restructures equally when the applied voltage changes.

As a result of the analysis, it is highly probable that the peaks are a consequence of the channel network which has the effect that the same current is observed no matter at which exit the network is probed. In view of the discussion in the previous paragraph this is the more likely explanation; no explanations of these peaks in terms of artefacts have previously been found. However, due to the fact that the EC-AFM method images only the pore exits at the surface it is difficult to comment on the quantitative connectivity of the hydrophilic paths within the membrane.

4.5   Time-resolved AFM measurements

Local changes in the polymer morphology are intimately related to the distribution of hydrophobic and hydrophilic areas at the membrane surface. These changes may have a significant impact on the long-term performance of the fuel cell, since they affect the proton transfer through the membrane. The distribution of the conductive regions reflects the distribution of current and of the Ohmic and reaction heating. Time resolved mapping of the proton transfer at the nanoscale can therefore reflect structural reorganizations of the ionically active areas and may contribute to a better understanding of the necessary microstructure and the proton conduction mechanism of Nafion.

4.5.1   Multi-scan-line profiles

In order to obtain a time resolved conductivity image, we performed repeated scans along a nominally identical line over a distance of 400 nm. The measurements are recorded at 57% RH with a constant scan rate of 1.45 Hz with 512 scans across three major, one intermediate and a few minor proton conducting pores. They are displayed in the conductivity image from the top to the bottom of Fig. 23. It is clearly seen that there is a membrane drift by about 70 nm over the entire scanning time. This may be due to changes in membrane swelling, perhaps as a consequence of the water that is attracted locally at the anode due to osmotic drag by the protons. It is likely that much of this transported water evaporates at the cathode by the heat dissipated by the cathode reaction. For further discussion we distinguish between two conductive regions I) and II) as indicated at the bottom of the figure. The size of the hydrophilic domains can be calculated from the single-line profile shown on the right of Fig. 23. After 84 s scanning time two conductive areas with average widths of 35 and 26 nm are detected in region I), at the same time in the region II) only one channel with a width of 35 nm is seen. After 260 s continuous scanning both conductive channels in region I) have a mean diameter of approximately 27 nm, which is significantly different from the size observed at 84 seconds. In contrast, the size of the conductive channel in region II) remains almost

constant. We suggest that these variations correspond to a rearrangement of the water distribution in the ionic network. It is significant that the calculated integral current in both regions stays relatively constant over the measuring time of ca. 280 s, indicating that these channels are directly connected with each other or at least to the same membrane network. A second observation is that shortly after the 260 s the current breaks down dramatically and remains at a low value until it recovers ca. 50 ns later. This break-down at a critical current density may be attributed to an excessive drying of the membrane during the measurement, as predicted by Eikerling *et al.* [83].
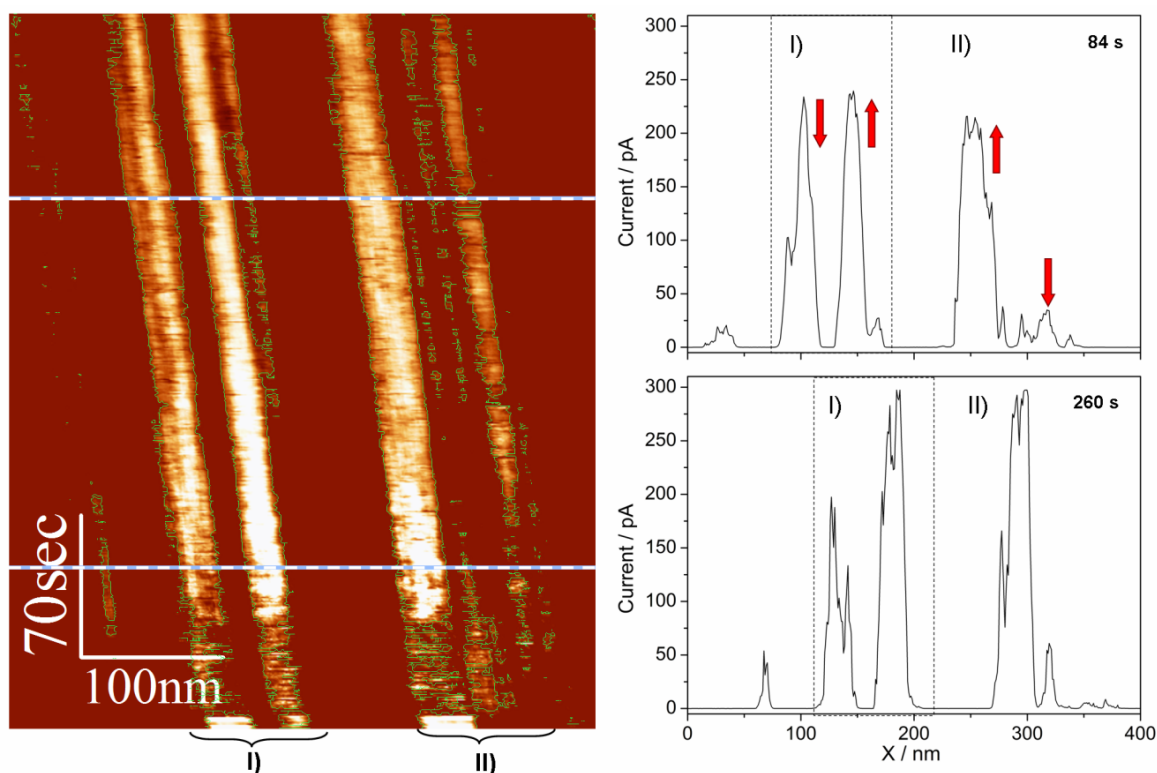
Figure 23: Time depended current distribution obtained at 57% RH at the Nafion 112 surface in the single-line-scan mode. The data was recorded from the top to the base. Dotted lines represent the cross-section-profiles detected after 84 s and 260 s [117].

We suggest that the reason for this current drop is an abrupt collapse of the channel, caused by the drying out of the pore, which in turns strongly depends on the scan speed and on the number of the scan cycles. The results demonstrate again that the bulk water content of the membrane is a key parameter that influences the transport properties.

4.5.2   Calculated current density

Figure 24 illustrates the current developments with time corresponding to the time interval of 350 seconds shown in Figure 23. The black curve represents the measured current in the right channel of region I), the green line the current in the left channel of region II).
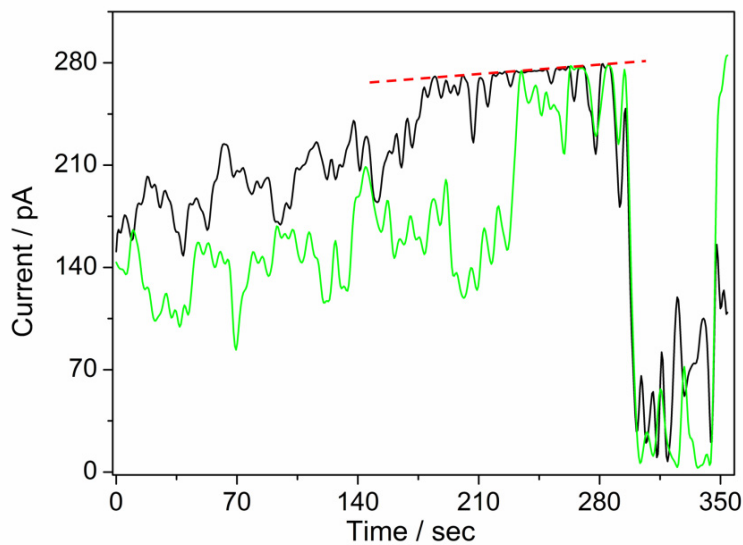
Figure 24: Temporal variations of the proton conductivity (evaluation of Fig. 23) measured through the channels in the region I) (black curve) and II) (green curve) with the scan rate of 1.45 Hz per line [117].

There are obvious current fluctuations, which we assign to changes in the nanostructure of Nafion and in the water content in the ionic network. Moreover, the diagram shows clearly that these two currents show an opposite behavior: an increase in region I) leads to a decrease in region II) and *vice versa*. Superimposed on the fluctuations there is a slight net increase, until the currents seem to reach an upper limit that cannot be exceeded, as indicated by the red line. The break-down then occurs simultaneously in the three major pores at a current of ca. 280 pA. Assuming circular pores of an approximate diameter of 30 nm as derived above from the widths of the peaks we obtain a critical current density of ca. 40 A cm^{-2}, i.e. of the same order as derived above from Fig. 4. These are peak values; as mentioned before the steady state value is about one order of magnitude lower. With these assumptions the critical current derived from the present experiments is of the same order of magnitude as predicted by Eikerling, who gave a

value of ca. 2 A cm^{-2}. Even though the conditions of the present experiment are not exactly the same as in the theoretical simulations the order-of-magnitude agreement is more than encouraging and supports the suggested interpretation. Nevertheless, it would need a significant effort in modeling to clarify these issues.

4.5.3   Influence of the applied force and scan rate

Generally, the surface topography and measured proton current of the Nafion membrane depend on the scan rate and on the applied force between the AFM tip and polymer surface. The application of stronger contact forces (> 100 nN) induces significant deformation on the polymer surface, especially for highly hydrated Nafion. The Fig. 25 demonstrates typical surface morphology at 92% RH. In order to prevent strong membrane drift, the scan rate was selected to 5 Hz. The increased scan speed considerably influences the quality of the obtained topography and the current image. Artificial horizontal lines in the scan direction can be seen in the topographic and the current image. Here, the corresponding current profile cannot be properly resolved.
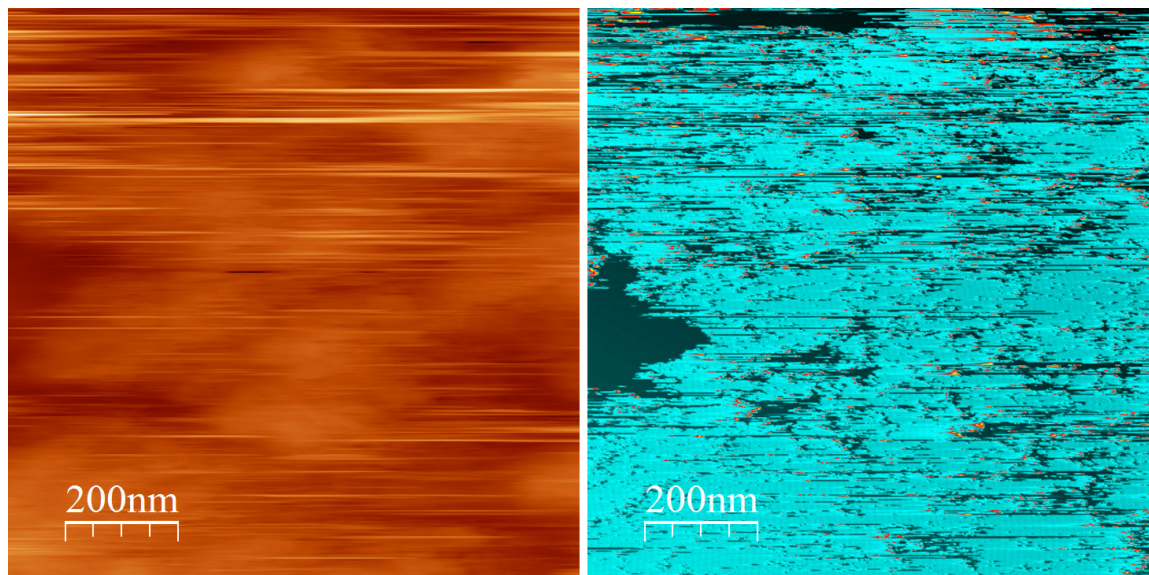

Figure 25: Simultaneously recorded AFM topography (left) and current (right) images of the Nafion 112 membrane (scan rate = 5 Hz, RH = 92%, scan size: 1 × 1 μm^2, applied force= 11 nN).

The obtained current image demonstrates higher noise signals. This effect was observed on the high scan rate and reduced relative humidity, ca. 50%. Therefore, in order to prevent the unwanted surface deformation of the Nafion membrane the scan rate in this work was limited to approximately 1 - 1.5 Hz.

In measuring the topography of Nafion, the strong interaction between tip and sample can cause a lateral deformation at the membrane surface. The deformations can be different in the regions with different mechanical and chemical properties: e.g. at hydrophobic and hydrophilic areas. Furthermore, the deformations will cause an error in topography measurement. One representative example of the influence of the applied force between the AFM tip and polymer surface is shown in Fig. 26. Here, the overlapping effect of the high scan rate and strong tip-to-sample forces lead to an error in the lower part of the image marked by arrows. The remarkable current sensitivity of the AFM tip allowed detecting the current for a short period even after the tip was in the error mode.
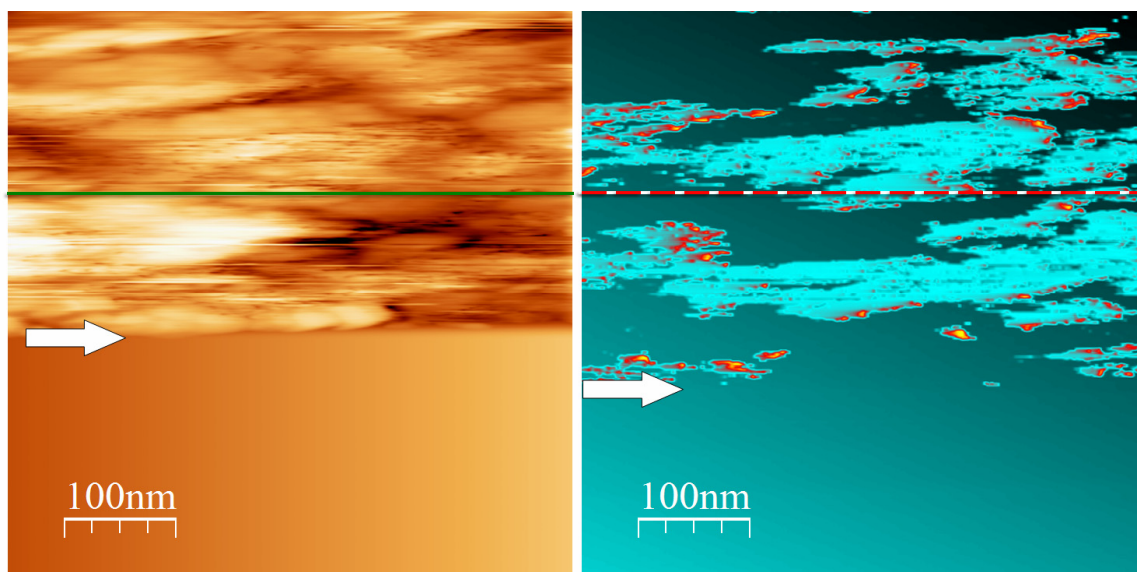
Fig 26: Simultaneously recorded AFM topography (left) and current (right) images of the Nafion 112 membrane (scan rate = 5 Hz, RH = 76%, scan size: 500×500 nm^2, Force = 53 nN Green and red dotted line represents the cross section profiles. The easurement error is marked by white arrows.

Figure 27 demonstrates the basic correlation between detected current and topography. In contrast to the Fig. 15 the high current peaks appear at deepest surface domains or cavities. This phenomenon can be explained by taking into account the tip shape and surface topography.
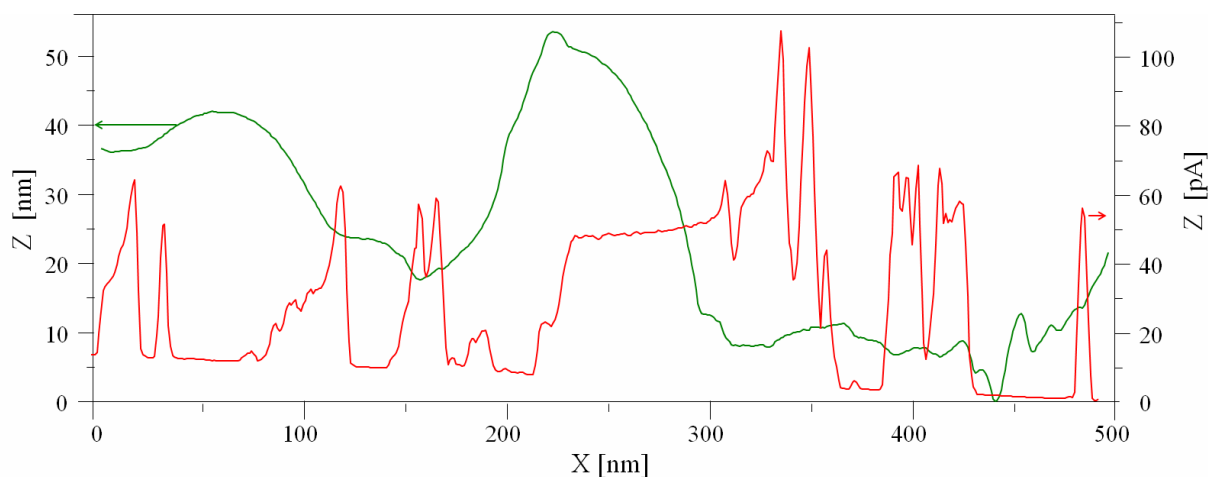
Figure 27: Correlation of the line profiles of topographic (green) and current (red) images.

Figure 28 represents a cross-section through the topography of Figure 26 and schematic AFM tip, drawn in the same elongated height scale. The AFM tip is positioned at the location where forces of the hydrophilic domain were expected.
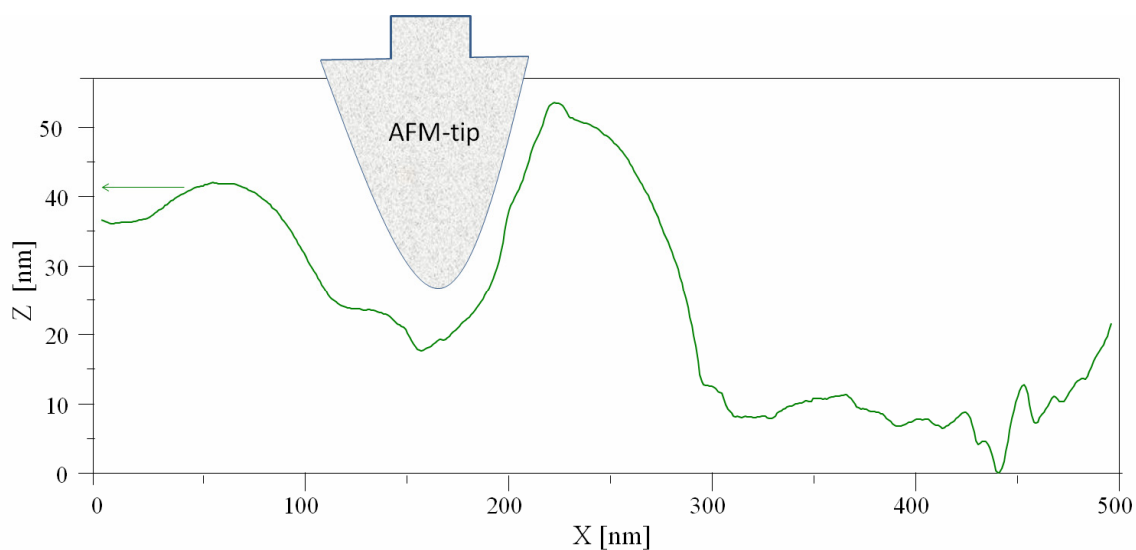
Figure 28: Cross section of the topography related to tip radius. The cross section profile represents the dotted line from the topography image in Fig. 26.

Figure 28 shows that an AFM tip with the radius (estimated from SEM measurements) barely fits into the cavity above the polymeric domain. In case the cavity surface involves hydrophilic domains covered with surface water, the surface topography would contribute to additionally attractive forces. This means that as the tip gets closer to the polymer surface, the interactions get stronger. It is certainly not unlikely that the attractive interactions on the polymer surface are not van der Waals interactions, and can be dominated from the neighboring hydrophilic parts covered with surface water. At this

point it is important to mention, that this effect does not play a role on the

topographically higher located hydrophobic domains. This observation is particularly important but leaves the question about the quantitative distribution of the surface water unanswered.

Furthermore, these results suggest that the physical distance over which current measurements were done are strongly dependent on the applied force. The formation of a water meniscus at high relative humidity between the tip and the sample would serve to increase the overall apparent size of the hydrophilic Nafion domains. However, in this work the effect on the applied force closer to the point of error was not examined. In contrast, no significant effects were observed at relative humidity lower than 60%. Generally, reduced relative humidity and slow scan rate enabled stable topography and current imaging on the nano-scale with reduced measurement error.

One additional point to note is the stability of the conductive Pt coating on the AFM tip, which is in the range of 25 nm. High applied force may lead to the abrasion of the conductive layer, as shown in the Fig. 29. The consequence is the increased tip radius and lower sensitivity.
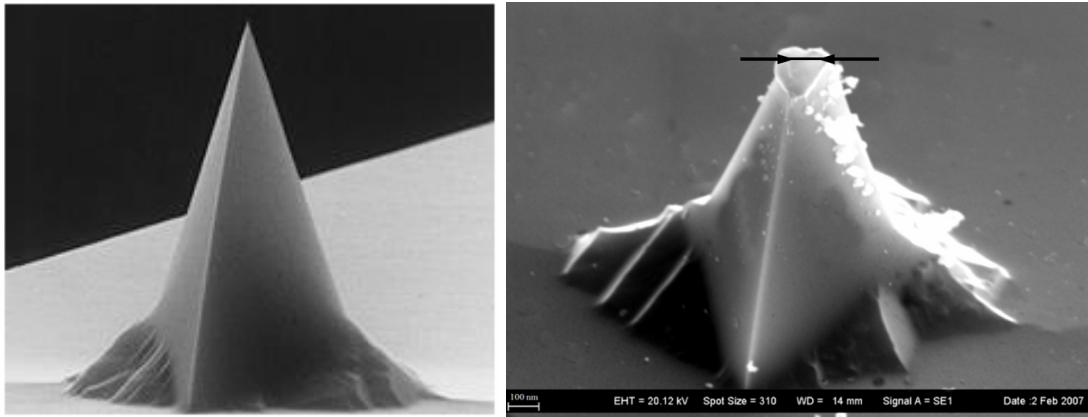
Figure 29: left: SEM image of the Pt coated AFM tip. Right: the top of conductive coating is damaged and the radius is in the range of 60 nm.

It was important to ensure that the applied force was not damaging the Pt coating, thus indirectly influencing conductive behavior. Force curves were measured over the surface under conditions similar to the experiment (1 Hz, with an applied force of 10 nN). It is clear from the measured force curve (shown in Fig. 10) that no discontinuities or significant adhesion events occurred after the application of 10 nN force.

4.6 Pore size analysis and conductivity properties

As already mentioned in the previous chapters, the macroscopically measured proton conductivity of a Nafion membrane is strongly correlated to its microscale properties, e.g. pore size, connectivity, and tortuosity. Of special importance is the correlation of the nanoscale measurements with the macroscopic results. In the past, the Nafion polymer has been intensively investigated by different bulk techniques e.g. impedance spectroscopy, dielectric spectroscopy, mechanical stress analysis, X-ray, high-resolution ^{13}C NMR and neutron scattering methods. Additionally, the spatial distribution of clusters in water-swollen Nafion was investigated by Dreyfus and co-workers [123]. For evaluation of the macroscopic data, varieties of theoretical approaches were developed. Similar to the Gierke model, most approaches assume hydrophilic domains, whose approximate size can change from 1 to 5 nm with increasing water content, and smaller hydrophilic channels, that enable the transport of ions between different water pools [124, 125]. But several other structure models have been proposed, such as the sandwich-like model by Haubold *et al.* and the polymer-bundle model by Rubatat *et al.* [126, 127].

To get a better understanding and examine the dynamics of the pore distribution at the polymer surface high resolution current images were recorded. The Fig. 30 shows a current image of a 250 x 250 nm^2 surface recorded at 63% RH. The right image represents a zoom into the dotted square with a threshold current of 120 pA. As described in the previous chapters, the image shows a particularly homogeneous distribution of the conductive areas. However, it must be pointed out that there is one fundamental difference to Fig. 17 – the conductive areas with low current flow are clearly separated from each other by nonconductive areas of a few nanometers. Additionally, the cross-section profiles demonstrate a reduced variation in the current values at a given relative humidity.
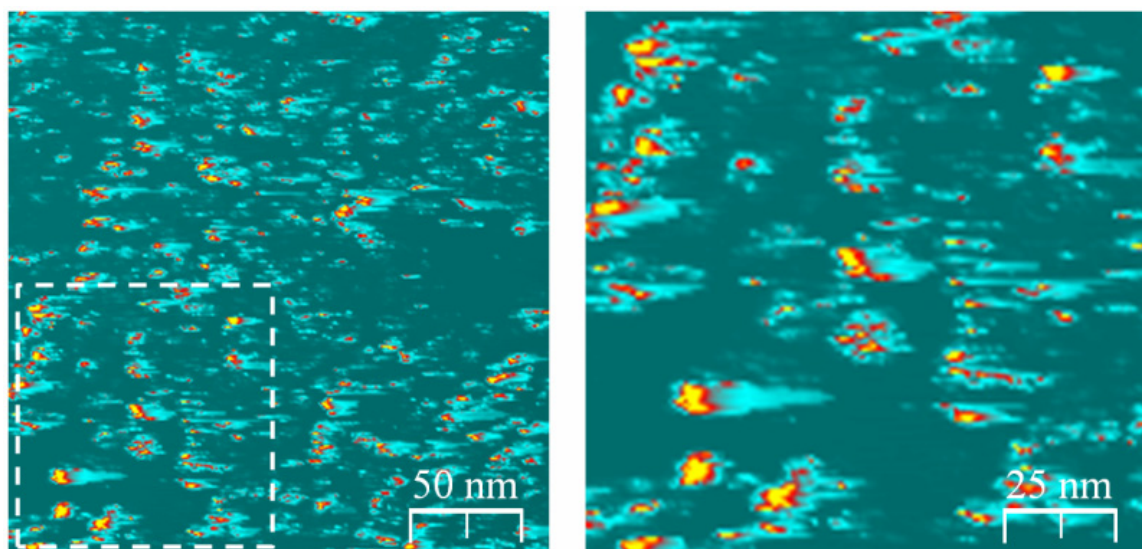
Figure 30: current images of the Nafion 112 membrane recorded at 63% RH and 1Hz scan rate. The scan size is 250 x 250 nm^2, and the applied voltage is 0.9V. The right image with a scan area of 125 x 125 nm^2 represents a zoom (shown as a dotted square) with a current threshold of 120 pA.

The cross-section profiles shown in Fig. 31 allow the identification of individual channels and conductive bundles.
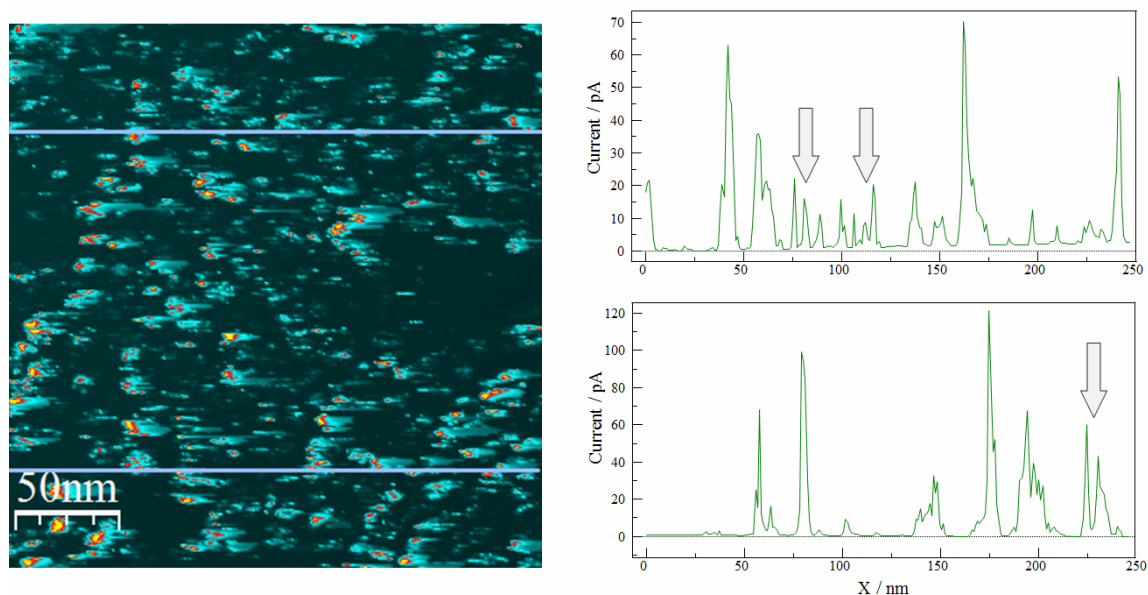
Figure 31: Variation of current-channel in diameter along the scan line. Cross-section profiles with resolved bundle (marked by arrows) of the conductive areas.

78

A closer look into the distribution of conductive areas at the surface gives an average diameter of 10-15 nm (evaluation of the Fig. 31). The smallest conductive area was in the range of 9 nm. Referring back to the comparison of the literature models with the structures of the high-resolution current images, the model of Schmidt-Rohr and Chen [53], which is based on SAXS neutron scattering and high-resolution ^{13}C NMR, is in reasonable good agreement. An important feature is that the conductive areas with similar diameter show equal current values. The higher current values come from the bundle of the conductive areas. However, the resolution is limited to the AFM tip diameter.

The calculation of Schmidt-Rohr *et al*. was performed for 19.4% water content, resulting in a RH of 95%. The authors postulated the existence of cylindrical inverted micelles represented in Fig. 32 a-c. The diameter of these cylinders varies between 1.8 and 3.5 nm, with an average of 2.4 nm. They are formed by the quite rigid back bones of the PTFE molecules. The hydrophilic sulphonic groups are located inside, and they are filled with water and provide conductive pathways for the proton flow under humidified conditions. A schematic drawing is shown in Fig. 32 b).
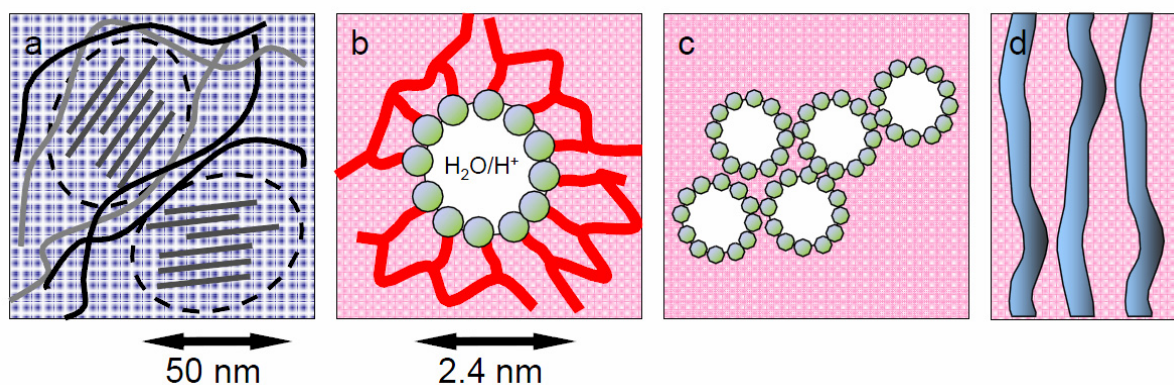
Figure 32: a) Model of the Nafion nanostructure according to Schmidt-Rohr *et al.* b) inverted micelle formed by sulphonated polymer molecules with inside water channel; c) aggregation of inverted micelles; and d) a sketch of the side view on parallel water channels [53, 128].

These inverted micelles are clustering together to form larger assemblies as shown in the Fig. 32 c) and provide water channels for the proton flow (Fig. 32 d). According to Schmidt-Rohr and Chen small PTFE-like crystals with a mean diameter of 5 nm are embedded in the membrane. The assumption of inverted micelles as the conductive channels in Nafion is in agreement with obtained EC-AFM results, in size as well as in their tendency to form agglomerates such as clusters or chains. A direct comparison of their model structure with an image of the nanostructure at the similar scale is given in Fig. 33 as a high-resolution current image.
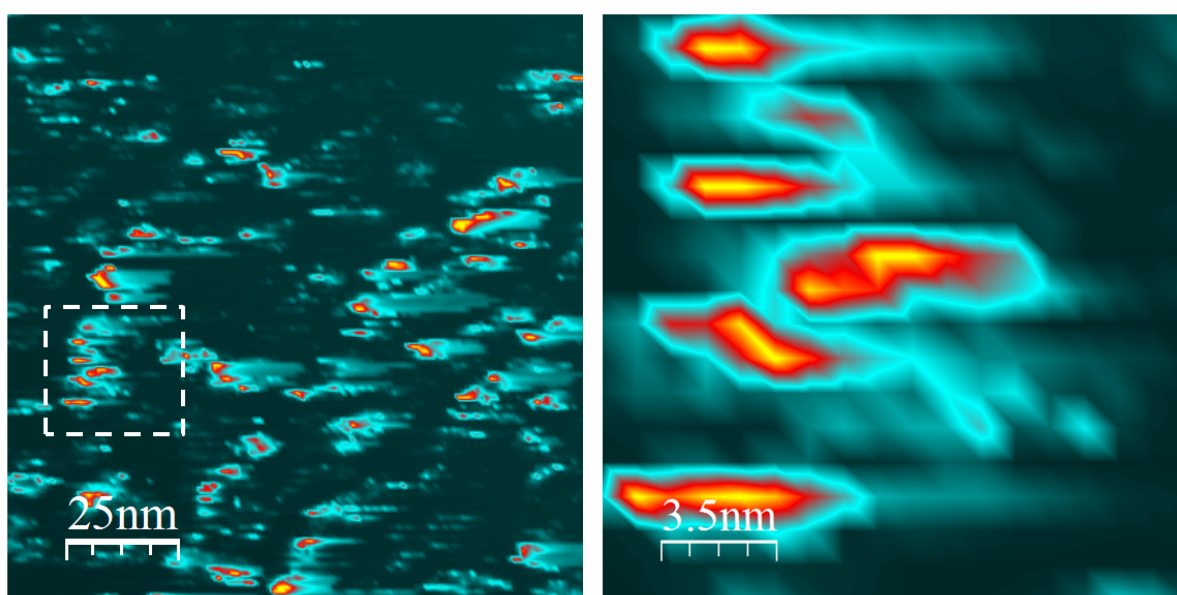
Figure 33: Left image is a high-resolution current image with the scan area of 125 x 125 nm^2. Right image is a zoom into the dotted area created using WSxM program. The red color bundles represent the current value of ca. 95 pA.

The Figure 33 shows two examples at different magnification of the current distribution on the Nafion surface which were recorded at a relative humidity of 63%. The scanned area is 125×125 nm^2 and the zoomed image 26 x 26 nm^2.

The probability distribution of current values for the different pixels was plotted against measured current values. The analysis is shown in the Fig. 34. Selected colors represent the same value as in Fig. 33. This kind of analysis was chosen in order to show that a huge amount of pixels do not contribute to the conductivity (dark color). Compared to Fig. 22 the histogram displays a peak current at higher values.

The histogram indicates how much of the surface is covered by proton conductive regions that are effectively connected through the bulk of the membrane. Generally, the detected current can be divided into four main parts: regions with a current close to zero, regions with a peak current in the range of 83-95 pA, and higher than 95 pA. In the middle of the histogram, there are only points in the range of 5-40 pA. This observation indicates that there might be different conduction processes inside the membrane. Such statistical evaluation of current values cannot provide reliable information of the reorganization process in the membrane, but gives valuable information about the dynamics at the surface.
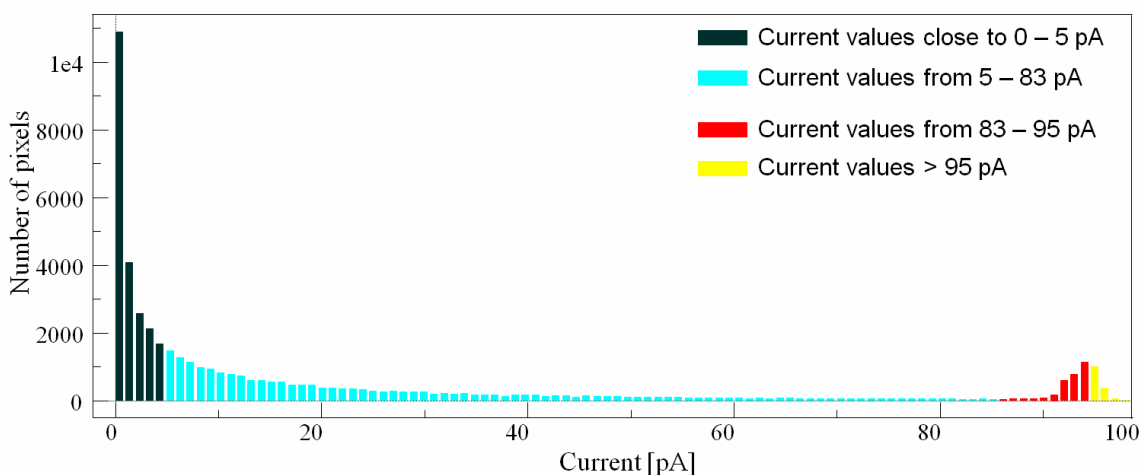
Figure 34: Histograms of number of conductive pixels for the Nafion membrane against current threshold values for the relative humidity of 63% (evaluation of Fig. 33).

From the obtained results, no direct information about the interconnection of the water channels can be derived, but the existence of a close interconnection is evident from a dynamic behavior of the active current domains, which change easily even at room temperature and given relative humidity [128].

The corresponding topography image is shown in the Fig. 35. The bundle of the conductive areas can be simply identified, marked as a few red spots with a size of a few nanometers, form a structural cluster of about 8 nm in diameter. These areas represent high current flow regions at the membrane surface. The size of bright areas is consistent with the size of inverted micelles according to the model of the Nafion nanostructure from Schmidt-Rohr *et al*. Fig. 32.

As a visualization of this model, a possible configuration of inverted micelles drawn on a measured current cluster is shown in Fig. 32 b). These current clusters are composed of highly conductive spots and frequently intersected by small (1 to several 10 nm) dark regions. As no current is detected here, these areas are probably hydrophobic polymer backbones (PTFE semi-crystals).
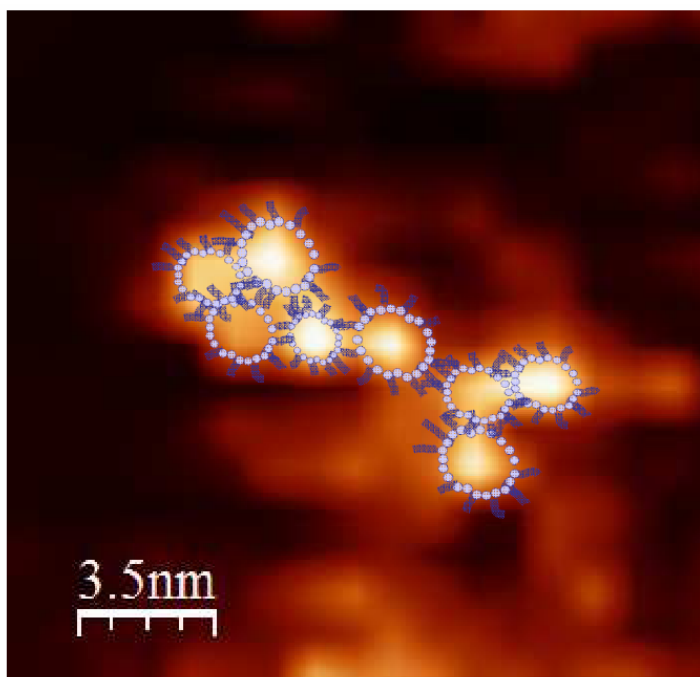
Figure 35: High-resolution image with schematic drawing of inverted micelles.

In one respect, this observation differs from the model by Schmidt-Rohr *et al.* where only cylindrical parallel water channels without connecting pathways are considered. In addition, the model does not include formation of higher order structures by clustering on different length scales; however, such super-structures are constantly observed during experiments. The formation of superstructures on different length scales has been postulated by Elliott *et al.* [112]. On the basis of small-angle X-ray scattering data from swollen and oriented perfluorinated ionomer membranes, the authors conclude that the statistically most probable scattering model for Nafion, based on a maximum entropy analysis of SAXS data, consists of an ion clustered morphology with a hierarchical structure. The smallest scale is composed of a three-dimensional array of roughly spherical, rigid ionic clusters, arranged with a mean separation and spatial coherence,

which are dependent on the processing conditions. This interpretation is consistent with EC-AFM measurements.

4.6.1   Correlation of the membrane structure and transport properties

In order to improve the transport properties of a polymer membrane it is important to understand the morphology and reorganization process of Nafion at the molecular level. Many investigations have focused on understanding the correlation of membrane structure and elucidating its role in the performance and conductivity characteristics of fuel cell membranes. However, the experimental and theoretical framework for developing a complete picture of proton transport in polymers, especially at the Nafion membrane has not been realized. It is well-known that the polymer conductivity is characterized by a nanophase separation during the wetting process between hydrophilic and hydrophobic domains. Generally, the proton transport mechanisms in a Nafion membrane are rather complex and could be affected by various factors in the complex operating environment of a PEM [82]. In this part only the relation between existing theory and measured current results will be discussed.

In the literature, the proton conduction process about the sulfonate domains in Nafion was found to proceed largely through the Grotthuss mechanism. In bulk water, protons may transport via two different mechanisms: the "vehicle mechanism" and "structure diffusion". For the vehicle mechanism, classical hydronium ions (H_3O^+) are the carriers of protons, and both water and protons diffuse at a similar rate. For the structure diffusion, protons migrate via a highly concerted process involving breaking and forming of hydrogen bonds and proton translocation within the "Zundel" and "Eigen" ions [83].

A decomposition of the hydronium ion shows that the overall diffusion process is a highly correlated exchange between diffusion through vehicular diffusion of the transient dominant state and the fluctuating bond topology, resulting in a relatively small net diffusion.

In total, the sulfonate ion significantly influences the diffusion of the protonic defects in a hydrophilic pocket of Nafion. As the transiently dominant hydronium state diffuses away from the sulfonate ion, the fluctuating bond topology "resets" the position of the dominant state back to some mean position relative to the adjacent sulfonate ion. The sulfonate ions effectively act as proton "traps", limiting the hydronium diffusion primarily to the long time correlated ion pair motions.

4.7 Electrode imaging and current distribution

In order to compare Nafion membrane activity with an electrode performance on image analysis of a Pt-coated electrode surface was performed. For this purpose a Nafion membrane double-side coated with carbon supported Pt-catalyst (1.0 mg cm^{-2} containing a mixture of 20% polytetrafluorethylen) was analyzed. A representative AFM topography image and the corresponding current distribution are shown in Fig. 36.
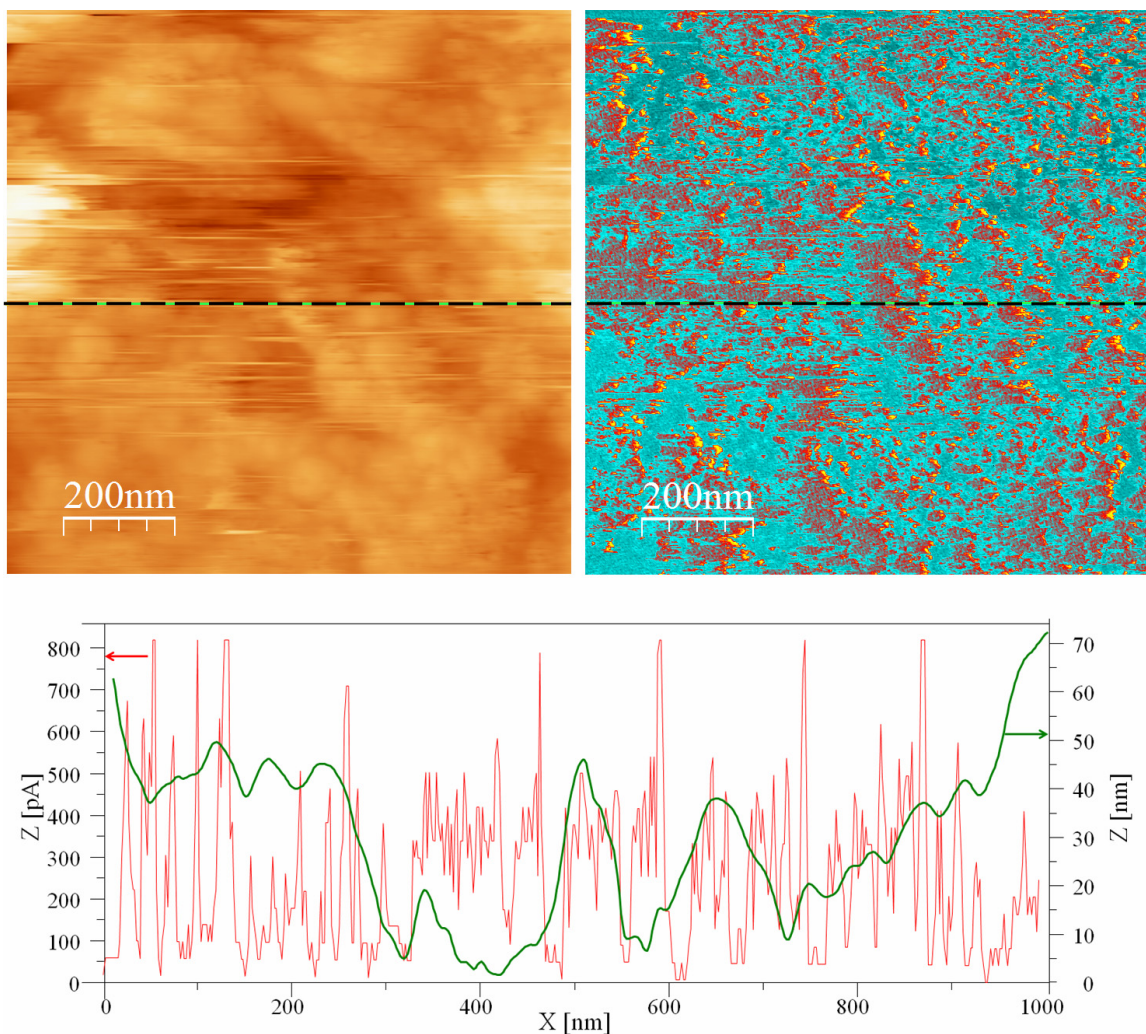
Figure 36: Simultaneously recorded AFM topography and current images of the Nafion coated membrane with 1.0 mg cm^{-2} Pt catalyst (scan rate = 1.5 Hz, RH = 42%, scan size 1×1 μm^2, +0.38 V). Corresponding line profiles of topographic (green) and current (red) images.

85

The topography image shows typical carbon grain structures with rounded shapes. Here, the electrode is composed of a carbon supported commercial fuel cell catalyst with a Pt particle size of 1-2 nm diameters [109]. Pt particles are homogeneously distributed on the surface of the carbon support. Carbon particles are connected with each other in a straightforward network with Nafion. From the topography image the size and position of active Pt particles located at the surface cannot be determined. The distinction between carbon support and Nafion part is not possible. In this regard, the current image provides more detailed information. It can be seen that measured current shows a relatively homogeneous distribution over a wide range. In contrast to the current distribution at the surface of the Nafion membrane where the nonconductive area was in the range of several hundred nanometers (Fig. 15), the electrode image demonstrates very fine and relatively sharp current peaks. At relatively low humidity of 42% RH, there are only few areas with zero current over the entire 1 x 1 μm^2 area. Due to the complexity of electrode composition, the interpretation of the observed current is quite challenging. On the one hand, the measured current cannot only be attributed to the Pt particles at the electrode surface. Most probably, high current peaks appear directly from Pt particles sitting at the top of the surface. Furthermore, a network of conductive carbon support may contribute to the homogeneous current distribution. On the other hand, the Nafion presence in the electrode can lead to an increased three phase boundary, which in turns determines better distribution and homogeneous arrangement of active areas. To summarise, one might say that measured current reflects a complex network performance over an entire electrode surface.

Nevertheless, some spots drops to the zero current. These nonconductive areas can be explained by coverage of active Pt catalyst particles and carbon support with hydrophobic, nonconductive phase of Nafion polymer. Additionally, agglomerations of catalyst particles and an ageing process can also contribute to a presence of nonconductive areas.

Due to the lack of information about interfacial connections, the results of the electrode imaging does not directly ensure the fuel cell performance. In order to provide a full picture, more detailed investigations and analysis of a complex relationship between chemical structure of Nafion and electrochemical performance of Pt catalyst would be required.

86

4.8   Potential and limitations of the experimental method

The EC-AFM method is suited for a qualitative mapping of the distribution of proton conductivity at the ion channel exits with a nanoscale resolution on the surface of polymer electrolyte membranes, while is not possible to make any statement about this distribution inside the membrane and thus to distinguish between different micro-morphological models such as, e.g., the ones by Gierke [42] and by Schmidt-Rohr [53]. However, the indirect evidence can be obtained from ECAFM measurements. A quantitative interpretation of absolute conductivity values and of the details of size and shape of conductive areas has to be carried out with caution. It depends on many factors and needs to take into account the following effects:

I) A step-like change of the applied voltage with the cantilever tip at the exit of a conductive channel gives rise to a transient current which relaxes with a decay constant on the order of one second to a steady-state current that is typically an order of magnitude lower than the initial peak current (Fig. 13). Neither the timescale nor the amount of transient current (typically equivalent to 10^9 protons, far more than the amount of charge that can be stored on the tip, based on a double layer capacity of a few tens of $\mu F \ cm^{-2}$ for Pt [52]) are compatible with a capacitive effect. It must therefore represent electrochemical transformations and has been ascribed to the build-up of a proton concentration gradient around the tip due to diffusion constraints inside the membrane. The following four observations support this interpretation.

a. The proton diffusion time through the 50 μm membrane is of the order of 0.1 s and agrees with the decay time of the transient current. The protons which are produced at the counter electrode arrive with this time constant to support the steadystate current.

b. The initial current of the transient converts to approximately the local pH value near −1 that is also obtained from the number of protons (i.e. sulfonic acid groups) and the amount of water in the membrane.

c. Integration of the current density over the entire area of an image and corrected by an order of magnitude to represent the steady-state current gives a typical

    current density that is obtained by conventional integral conductivity measurements, e.g. by impedance spectroscopy.

  d. If the AFM tip contacts the membrane outside a conductive spot the applied voltage step leads to a transient current which is unresolved and confined to essentially a single channel of the time histogram (20 ms in a typical experiment). This may possibly represent the capacitive effect but is hard to distinguish from an instrumental response to switching the voltage.

II) The measured current depends on the contact area of the AFM tip with a water layer on the surface of the membrane. At least initially, this is a function of the contact force between the probe and the sample, the AFM probe geometry and the extent of surface wetting. However, the amount of water that is formed at the tip is substantial. For example, the 10^9 protons represented by the transient shown in figure 8 correspond to 10−15 mol of water that is formed within one second, which is a hemispherical droplet with a radius of 200 nm. This could heavily impair the spatial resolution of the technique, but fortunately most of this water and even much of the additional water that is transported to the surface by electro-osmotic drag is evaporated by the heat of reaction, as rationalized in section 3.3, and some of it may also be reabsorbed by the membrane. The heat of reaction of water formation at the cathode is provided by the equivalent electrical work that is spent for water cleavage at the anode.

It can be expected that the conducting AFM technique presented in this work will clarify mechanisms of polymer structure and transport of protons. The through-plane proton conductivity measurement would be a supporting tool for analysis of the fuel cell membranes more precisely, even though there is still room for improvement in reproducibility and reliability [117].

4.9   Conclusion and outlook

4.9.1   Nanostructure of Nafion

The present work demonstrates nanoscale current measurements of the Nafion 112 membrane obtained using electrochemical atomic force microscopy. It is useful as a technique which allows the determination of the distribution of ionically active domains at the membrane surface. The obtained results provide valuable nanoscale information, but it is not thought to be a method to compete with conventional measurements of integrated absolute proton conductivity.

The fact that hydrated Nafion does not phase separate into dry polymer and liquid water shows that it is favorable for the sulfonate groups to be hydrated. Then, in constructing or considering structural models of Nafion, the main constraint is the ~3.6 nm dimension of two Nafion molecules packed back-to-back. At all but extremely low water contents, any point in the polymer, apart from ~10% of crystalline material, should be within ≤ 3.6 nm/2 = 1.8 nm from the nearest polymer-water interface. This thickness constraint excludes thick polymer bundles or large spacings between water channels. On the other hand, thick layers of water or varying diameters of water channels are possible.

At relatively high humidity (hydration level) the non-conductive areas are unexpectedly large compared with the conductive spots at the surface. Nevertheless, the results appear to broadly support the phenomenological model of a nanoscopically phase separated ion-cluster morphology predicted by Gierke et al [39, 42] or by Schmidt-Rohr and Chen [53]. However, there remain important differences, including the fact that the shape and size of the active ionic domains are quite variable and may change with the environmental influence. The necessary resolution of around 1 nm for a stringent test has not quite been reached. For the given relative humidity there is an appreciable peak current. This peak current is collected from conductive spots which have a similar average diameter.

Since the tip spends about 300 ms on top of a pore the current values will be affected to some extent by transient effects [39, 40]. At higher humidity a water droplet may be dragged along by the AFM tip, as suggested by the observed elongated structures, which may lead to higher apparent values for the channel size. These experimental aspects will

be investigated in the course of the further development of this technique. The measured current reflects the distribution of the conductive areas at the surface. The time resolved conductivity mapping provides indirect insight into the connectivity of the hydrophilic paths, their dynamic behavior, including diffusion processes within the pore network. The origin of the critical current that depends on the pore size and pore distribution should be further investigated, towards a quantitative verification of theoretical predictions. The obtained information is expected to be of significant importance in respect of optimizing water management and membrane conductivity in fuel cells. First results of analogous measurements on polyaromatic membranes have been obtained, and it is interesting to compare them with those obtained with Nafion [49]. The objective of this effort is to discern the microscopic morphology from the proton conductivity, which would benefit the development of membrane casting procedures and of durability studies of PEM fuel cells.

In recent years, a wide range of articles were published covering electrochemical AFM investigations on the fuel cell membranes and this trend will probably continue. The high attention factor for this investigation technique reveals the importance for a new synthesis development and improvement of the conductive polymers. The results from EC-AFM technology have increasingly served the fields. The influence of microphase separation of the multiblock and random copolymers on the conductivity was intensively examined [129, 130]. For multiblock copolymers it was founded that phase separation increase proton conductivity without increasing swelling behavior. The content of nonconductive surface affects the interfacial connections. An additional improvement of the EC-AFM technique was reached in regard to the measurements of impedance spectra with high spatial resolution by Hink *et al.* [131]. The first evidence of a potential dependent electrolyte resistance was discussed. The analysis of the polarization curves shows a typical exponential increase according to the Buttler-Volmer kinetics in the low overpotential regions. In the supplementary work, results obtained from the EC-AFM investigation on the related Nafion membranes suggested different micro-phase separation depending on the manufacturing process.

4.9.2   Consequences for the fuel cells

In order to improve the membranes and membrane electrode assemblies, it is essential to understand factors which might be key determinants of fuel cell performance. One of the key parameters is the improving fuel cell performance by increasing Pt utilization in the catalyst layer [22]. The second key parameter is the membrane resistance, including interfacial resistance between the membrane and the electrode. Therefore, enhancing proton conductivity without increasing water uptake or membrane thickness is a major task of the researchers. But changing the polymer properties always affects the interfacial connection with the electrode. This effect is due to an increase in the non-conductive surface area that might act as barrier to mass transfer. Hence, an optimized membrane thickness and Nafion content in the catalyst layer are necessary for good performance, and should depend on the platinum loading and the fabrication method.

At present, a proton-conducting ionomer is required in the catalyst layer of PEM electrodes to extend the triple contact line between the reactant gases, the electrolyte and the catalyst so as to enhance the electrochemical reaction Fig. 36 [16, 68]. Nafion ionomer in the catalyst layer also helps to retain humidity and prevent membrane dehydration, especially at high current densities. The content of Nafion ionomer affects simultaneously the gas permeability, the catalytic activity, and the ionic resistance. Therefore, the correlation between membrane surface activity and fuel cell operating conditions (e.g. humidity, applied voltage, real electrode coating) was investigated using a Nafion membrane. The EC-AFM method makes it possible to distinguish the active proton conductive regions of the polymer membrane surface by simultaneously collecting the topographic, and proton conduction images with high resolution.

The proton conductive regions on the membrane surface were successfully observed by using electrochemical atomic force microscopy. The obtained current distribution revealed a strong dependence of the hydrophilic/hydrophobic microphase-separated structure.
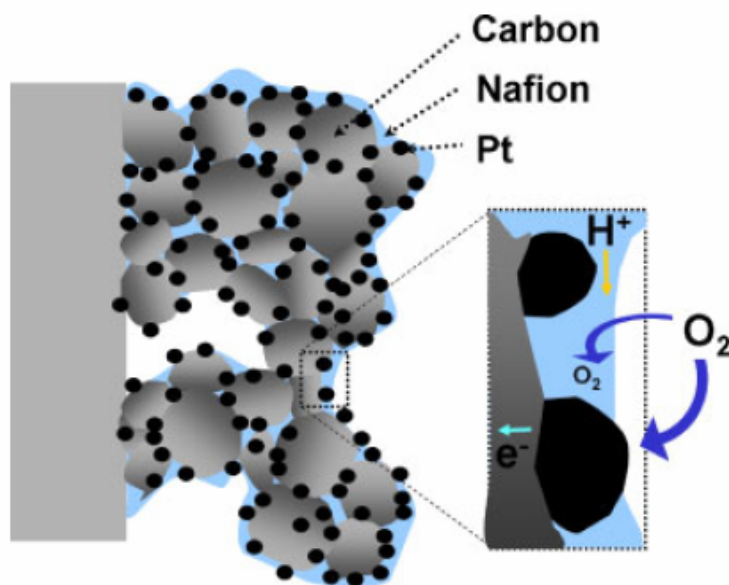
Fig 37: Schematic electrode microstructure, shown in particular for the cathode. The inset shows the magnification of a single catalyst particle in contact with its carbon support, the electrolyte, and the gas phase [128].

The results of this study, especially the observation of the large nonconductive areas, suggest the necessity for further improvement of the polymer membrane by optimizing the casting conditions and molecular design of the polymer. Furthermore, the electrode/electrolyte interface can be optimized. A three phase boundary where all important physico-chemical processes occur can be optimized. Correspondingly, the possibilities for improvement in electrode performance and Pt utilization, by refining the optimum Nafion content and molecular architecture especially for electrodes with low Pt loadings could be investigated. Additionally, the influence of the membrane activation processes can be analyzed.

There is still a pressing need for experimental analysis that can provide more detailed information about membrane transport properties at the nanometer scale and the complex relationships between chemical structure, physicochemical properties, and electrochemical kinetics.

Chapter 5

5   SUMMARY

In general two achievements have been made in this work, which have not been part of the common understanding of the membrane conductivity analysis and PEFC research: First, the development and successful application of the EC-AFM measurement method to observe simultaneously the topographic and the active proton conductive regions of the Nafion surface at the nanometer-scale; and second, the impact of the relative humidity and applied voltage on distribution of pore size and conductive regions at the membrane surface.

The earlier research describes the structure of a hydrated Nafion by a microphase separation of hydrophobic and hydrophilic groups. According to the Gierke model based on the small-angle X-ray scattering data sulfonic groups form hydrophilic domains which are connected by ca. 3-5 nm pathways to the ionic channels which are responsible for the high proton conductivity.

In this work the EC-AFM method uses conventional AFM [Nanoscope III, Digital Instruments (DI), Santa Barbara, USA], and conductive Pt-coated AFM-tip for measurement of the proton conductivity at the membrane surface. By applying a voltage between the tip and the single-side Pt-coated membrane protons and electrons will be produced from water electrolysis. When the tip is located on the conductive area, the protons can be transported through the channels and react back to water. The produced water will be directly evaporated, due to the exothermic reaction. In this manner the resolution of the observed current image remains relatively high. The maximum distances at the surface between the conductive areas are in the range of several hundred nm and depend strongly on the relative humidity. The conductive regions represent the ends of channel structures with a diameter of 10-40 nm in width. The observed size of active areas depends on the contact area of the AFM tip with a water layer on the surface of the membrane. The results appear to broadly support the phenomenological model of a

nanoscopically phase separated ion-cluster morphology predicted by Gierke *et al.* or by Schmidt-Rohr and Chen

The analysis of the current profile across the conductivity image shows that current peaks are separated by gaps with conductivity close to the zero. According to the nanostructure of the Nafion polymer this means that a large fraction of acid groups is inactive in these non-conducting regions and does not contribute to the entire membrane conductivity at room temperature. Furthermore, a comparison of the line profiles across simultaneously obtained topographic and current images shows that there is no simple correlation between the observed current and morphological structure. This result has been expected because the topography represents the morphological features of the surface which depends on the membrane manufacturing process.

Generally, the conductivity image analysis demonstrates that the proton flux is extremely inhomogeneous on the nanometer-scale and depends strongly on the relative humidity. Extrapolation of the results suggests that the conductivity goes to zero at a RH of less than 32% RH. This observation gives a hint that there is a percolation limit below which the membrane shows a high resistance. Conductivity images obtained from the different relative humidity measurements display a notable increase of the conductive area with increasing RH. Furthermore, the results show that the proton conductivity is proportional to the water content of the membrane. At RH > 95% the increase of conductive area is no longer linear and reaches saturation. An estimated macroscopic conductivity was calculated by integration of the spatially resolved images. Taking into account the steady state current at 40% RH the obtained macroscopic conductivity reaches a value of 2.1 A cm^{-2} and at 50% RH a value of 3.4 A cm^{-2}.

The time-dependent response after an applied potential step is investigated while the AFM-tip is located on the conductive area. The observed transient behaviour is presented in *I-t* curves. The monitoring of a time dependent current response following a potential step indicates that the ionic network must be connected inside of the Nafion membrane and involved in water and proton transport through the membrane. Quite important for further understanding is the prediction of the channel size based on the calculated pH-value from the observed time response curve. The initial current of the transient converts to approximately the local pH value near −1 that is also obtained from the number of

protons (i.e. sulfonic acid groups) and the amount of water in the membrane. This analysis give a strong indication that the conductive spots at the membrane surface represent the exit ports of sulfonic groups. The detected peak current represents the local equilibrium proton concentration, which is quite well known for the given content of acid groups and of water in the membrane. On a macroscopic basis at a current density on the order of 1 A cm^{-2} all protons in the membrane are exchanged approximately once a second. It is probable that the present measurements reflect the unresolved conductivities of small bundles of hydrophilic channels.

In addition to the relative humidity the applied voltage influences local conditions at the membrane surface, hence influencing the maximum measured current. The higher potential difference at the electrodes represents an increase of the driving force for proton transport across the membrane. In consequence, the proton transport is accompanied by the reorganization of the polymer structure. Nevertheless, the measured 3D current images showed a consistent structure with a rope-like organization that was attributed to a string of polymer backbones. A typical size of a non-conductive surface area was in the order of 120 to 230 nm^{2}.

For a better understanding of the data, the probability distribution of current values measured for the different pixels was analyzed. The extremely sharp peaks in probability distributions are spectacular and unexpected for a Nafion material that is normally thought of to be amorphous. The sharp current peaks consist not only of a single histogram bin; on an expanded scale it can be resolved into a band which is probably the Gaussian distribution that was reported also by Xie *et al.* In this work the peaks were interpreted as bundles of channel ports through which exactly the same proton number per unit time is transported to the surface. This fact means that Nafion forms with a high probability a preferred structure (or channel size) that can conduct exactly a given amount of current. At the same time, this behavior could be interpreted as a consequence of different conduction processes inside the membrane. Eikerling *et. al.* predict a difference from 'bulk water' in conduction process. In the center of large pores, proton transport is efficient and based on the Grotthuss mechanism, whereas in small pores which do not contain bulk water protons migrate by the vehicle mechanism via water molecules which are attached to the pore walls, interspersed between the sulfonic acid groups which exert a strong electrostatic attraction. As a result of this analysis it is highly

probable that the peaks are a consequence of the channel network which has the effect that the same current is observed no matter at which exit the network is scanned.

Further, the model of Eikerling *et al.* predicts the water content profiles and the voltage–current plot for medium current densities, which revealed evidence for the existence of a critical current. Therefore, in order to observe structural reorganizations of the ionically active areas time resolved mapping of the proton transfer were performed as repeated scans along a nominally identical line over a distance of 400 nm. The current developments demonstrate an obvious fluctuation, which can be assigned to changes in the nanostructure of Nafion and in the water content in the ionic network. The break-down then occurs simultaneously in the three major pores at a current of ca. 280 pA. By the recalculation a critical current density of ca. 40 A cm^{-2}, almost the same order as derived from *I-t*-curves, were obtained. Taking into account the steady state value the critical current derived from the described experiments is of the same order of magnitude as predicted by Eikerling, who gave a value of ca. 2 A cm^{-2}. Although the conditions of the experiment are not exactly the same as in the theoretical simulations the order-of-magnitude agreement is more than encouraging and supports the suggested interpretation. Nevertheless, it would need a significant effort in modeling to clarify these issues.

In addition, measurements with a double-side coated membrane (Pt/C-catalyst 1.0 mg cm^{-2} dissolved in a mixture of 20% polytetrafluorethylen) were performed. From a topography image the distinction between carbon support and Nafion was not possible. The analysis of the current image provides a clear difference to the conductivity of the Nafion membrane. In contrast, the detected current at the electrode surface shows a relatively homogeneous distribution over a wide range. An electrode image demonstrates very fine and relatively sharp current peaks. Due to the lack of information about interfacial influence, the results of the electrode imaging does not directly ensure the fuel cell performance and the Nafion membrane resistance distribution. Under real operation conditions, the distribution of current will be determined by the distribution of the membrane resistance by means of the product water distribution (i.e. dry starting conditions). Therefore, a systematic analysis of the electrode is needed.

The EC-AFM is an invaluable tool for identification and spatially resolved characterisation of proton flux at the membrane surface in comparison with topography. The observable unprecedented spatial resolution of ca. 10 nm exceeds that of conventional methods by many orders of magnitude. The obtained results are consistent with those of conventional macroscopic measurements, confirming the reliability of the method.

- ✓ The observed current inhomogeneity gives rise to enhanced local dissipation of heat of reaction that leads to "hot spots" at places with very high reactant turnover, causing higher membrane resistance due to partial membrane drying at the anode side and initiating free radical formation, which can accelerate membrane degradation. The obtained information is expected to be of significant importance in view of optimizing water management and membrane conductivity in the fuel cell.

- ✓ The EC-AFM method can be extended to alternative proton conducting polymer membranes. It will be interesting to see in which respect they differ in their micromorphology and in their behavior at a nanoscale.

- ✓ It will allow careful analysis of the homogeneity, the nature and the consequences of microphase separation as well as the effect of humidity on novel alternative membranes, and it will thus be essential for tailored developments of new materials for fuel cell membranes.

For the future research, the know-how about ionomer structure and membrane transport properties can support the understanding of the nanophase segregation under fuel cell conditions and the complex relationships between physicochemical properties and electrochemical kinetics. Due to the importance of proton transport on fuel cell performance, further work will be performed to understand transport mechanism and to identify the limiting parameters.

6   ZUSAMMENFASSUNG

Die Polymer-Elektrolytmembran ist die Schlüsselkomponente einer Brennstoffzelle. Die meist eingesetzte Nafion-Membran, auf der Basis eines perfluorierten Polymergrundgerüsts, dient als Elektrodenträger und gleichzeitig als Separator für die Gase. Die Anforderungen schließen eine hohe Protonenleitfähigkeit ein, um den Ohmschen Widerstand der Zelle zu minimieren und den Wirkungsgrad zu erhöhen. Die elektrolytische Leitfähigkeit hängt von den Betriebsbedingungen der Zelle ab, insbesondere von der Feuchtigkeit sowie von dem Ausmaß der zyklischen Beanspruchung. Die Materialeigenschaften des Polymers haben eine entscheidende Rolle bei der Ausbildung der Ionenkanäle. Generell stellt man sich vor, dass diese Ionenkanäle durch eine Mikrophasenseparation von hydrophoben und hydrophilen Anteilen des Polymers entstehen.

In der Literatur ist die Morphologie von Nafion relativ gut untersucht. Die Analyse von Kleinwinkel-Röntgen- und Neutronen-Streuexperimenten weist auf die Bildung von Ionenclustern, die inversen Mizellen gleichen. Diese haben einen Durchmesser von ca. 4 nm und sind unter bestimmten Bedingungen durch Kanäle mit einem Durchmesser von ca. 1 nm verbunden. Mikroskopische Untersuchungen mittels Kraftmikroskopie (AFM) im "Tapping-Mode" zeigen Strukturen, welche Ionenkanälen zugeordnet wurden; direkte Information über Leitfähigkeit ist damit aber nicht verfügbar. Die Information über die Membranleitfähigkeit basiert überwiegend auf makroskopischen Impedanzmessungen. Prinzipiell bietet ortsaufgelöste Impedanzspektroskopie basierend auf Kraftmikroskopie einen Zugang zur Leitfähigkeit, bisher wurden damit aber keine überzeugenden Resultate erzielt, insbesondere waren der Kontrast und die örtliche Auflösung (ca. 100 nm) zu beschränkt, um einzelne Ionenkanäle abbilden zu können.

Das Hauptziel dieser Arbeit war mit Hilfe von elektrochemischer Rasterkraftmikroskopie eine auf nanometer-aufgelöste Darstellung der Protonenleitfähigkeit einer Nafion-Membranoberfläche zu gewinnen. Der Schwerpunkt lag hierbei auf der Untersuchung der Zusammenhänge zwischen Ionenleitfähigkeit und Nanostruktur einer Nafion Membran unter der definierten Luftfeuchtigkeit und angelegten Spannung. Außerdem wurde der zeitliche Verlauf des Stroms bei Anlegen von Potentialstufen ermittelt, um zu einem

besseren Verständnis der im Membraninnern stattfindenden Transportvorgänge zu gelangen.

Die elektrochemische Raster-Kraft-Mikroskopie (Electrochemical Atomic Force Microscopy, EC-AFM) ermöglicht nicht nur die Aufklärung der Topographie von Oberflächen durch Abscannen mit einer an einem Federbalken befestigten Spitze, sondern darüber hinaus auch die Visualisierung von dort vorhandenen ionenleitenden Bereichen mit einer außergewöhnlich hohen Auflösung von ca. 10 nm.

Das Messprinzip ist in der Fig. 11 dargestellt. Die auf einer Seite der Nafion-Membran aufgebrachte Pt-Katalysator-Schicht dient als Anode, an der beim Anlegen einer ausreichend hohen Spannung (> 700 mV) Wasser unter Sauerstoffentwicklung oxidiert wird. Dabei kommt es gleichzeitig zur Freisetzung von Protonen, die durch die Polymerelektrolyt-Membran zur Kathode, der Pt-beschichteten leitfähigen EC-AFM-Spitze, wandern und dort mit dem Sauerstoff der Umgebungsluft wieder zu Wasser reagieren. Bedingung für das Eintreten dieser elektrochemischen Reaktionen ist, dass sich die AFM-Spitze über Bereichen der Membranoberfläche aufhält, in denen die ionenleitenden Strukturen der Membran enden. Nur dann lässt sich ein Stromfluss detektieren.

Experimente wurden unter Verwendung eines kommerziell erhältlichen AFM-Messgeräts [Nanoscope III, Digital Instruments (DI), Santa Barbara, USA], das mit einer elektrochemischen Zelle (Fig. 12) und einem Potentiostat als Spannungsquelle ausgestattet war, in einer Klimakammer durchgeführt. Die an einem beidseitig Pt-beschichteten AFM-Federbalken (Federkonstante k = 0,2 N/m, Nano World®) befestigte AFM-Spitze lag mit einer Kraft von etwa 10 nN auf der Membranoberfläche auf. Der Strom wurde mittels eines selbstgebauten Stromverstärkers (0,5 MΩ bis 10,0 MΩ) gemessen und über einen Hilfseingang aufgezeichnet, wobei ein Signalzugangsmodul (DI) die gleichzeitige Aufnahme von Stromfluss und topographischen Daten ermöglichte.

Die in dieser Arbeit untersuchte Nafion-Membran wurde am Institut für Technische Thermodynamik des Deutschen Zentrums für Luft- und Raumfahrt (DLR) mit einem Pt-Katalysator (1,0 mg/cm^2) beschichtet.

100

Zur Untersuchung der Zeitabhängigkeit des durch die Membran fließenden Protonenstromes wurde die AFM-Spitze auf einem leitfähigen Bereich der Membranoberfläche positioniert und die Spannung stufenweise verändert. Die Regelung des Piezoelements wurde während der Messung abgeschaltet. Der zeitliche Verlauf des gemessenen Stromes ist in Fig. 13, 14 gezeigt. Unmittelbar nach dem Spannungssprung lässt sich ein plötzlicher Anstieg des Stromes bis zu einem Maximalwert I_{max} von 0,7 nA beobachten, gefolgt von einer Stromabnahme, die nach ca. 0,9 s mit einer Halbwertszeit von 0,3 s zur Einstellung eines beinahe konstanten Wertes I_{DC} von 0.2 nA führt. Der gemessene Stromanstieg wird durch die Ausbildung des Diffusionspotentials in der Membran begründet. Die Analyse der Zeitabhängigkeit des Stromflusses ermöglichte die Berechnung von realistischen Werten für die durchschnittliche Membranleitfähigkeit, sowie des pH-Wertes in der betrachteten einzelnen Pore. Dieser liegt für die gezeigte Pore bei pH= -1, mit einem Wert λ=10.

Die Topographiemessungen zeigen eine für Kunststoffe typische leicht gewellte Oberfläche. Anhand der aufgenommenen Strombilder lassen sich die ionenleitenden Gebiete, die mit dem leitfähigen Netzwerk im Innern der Membran verbunden sind, ermitteln (Fig. 15). Aus den Messungen geht deutlich heraus, dass die ionenleitenden Regionen keineswegs gleichmäßig über die gesamte Membranoberfläche verteilt sind. Vielmehr werden sie durch hydrophobe Bereiche getrennt. Bemerkenswert ist, dass die nichtleitfähigen Bereiche bei 58% Luftfeuchtigkeit so groß ausfallen, denn die Sulfonsäuregruppen im Nafion sind in einem Abstand von ca. 3 nm angeordnet [42]. Diese Tatsache schließt aus, dass in diesen Bereichen keine SO_3^--Gruppen vorhanden sind. Eine mögliche Erklärung wäre, dass diese Gruppen wegen eines zu geringeren Wassergehalts nicht mit dem ionischen Netzwerk der Membran in Verbindung stehen. Erhöht man die Auflösung, so werden hydrophile Bereiche erkennbar, die einen Durchmesser von 10 nm bis hin zu 70 nm besitzen und aus einer Ansammlung kleinerer Kanäle bestehen, die nicht mehr vollständig aufgelöst werden können. Der Durchmesser der einzelnen Kanäle beträgt 9 nm bis 23 nm, wie dem Linienprofil im unteren Teil von Fig. 15 zu entnehmen ist. Insgesamt wurden Ergebnisse erhalten, die gut im Einklang stehen mit theoretischen Überlegungen sowie den in anderen Studien gemachten Beobachtungen.

Vergleicht man die Linienprofile durch die Topographie- und Strombilder entlang der gestrichelten Linien miteinander (Fig. 15, unten), so lässt sich keine einfache Korrelation zwischen der Oberflächenstruktur und der Verteilung der leitfähigen Gebiete erkennen. Dies ist aber nicht überraschend, da die Morphologie der Membranoberfläche im Wesentlichen durch das Herstellungsverfahren bestimmt wird. Auffällig ist hier vor allem die Beobachtung unerwartet großer nicht leitfähiger Gebiete; möglicherweise sind die dort endenden Kanäle nicht mit dem ionisch aktiven Netzwerk der Membran verbunden.

Bei verschiedenen Luftfeuchtigkeiten durchgeführte Messungen (Fig. 18) ergaben eine Vergrößerung des leitfähigen Flächenanteils sowie der Porendurchmesser mit steigender Luftfeuchtigkeit auf Grund des erhöhten Wassergehalts der ionenleitenden Strukturen im Membraninnern. Trägt man die leitfähige Fläche gegen die prozentuale Luftfeuchtigkeit auf, wie in Fig. 19 gezeigt, so ergibt sich ein linearer Zusammenhang. Eine Extrapolation der Geraden lässt vermuten, dass bei einer Luftfeuchtigkeit von 32% keine Protonenleitung durch die Membran mehr stattfindet, was aber im Widerspruch zu anderen Studien steht, die auch bei 25% Luftfeuchtigkeit noch ein gewisses Maß an Leitfähigkeit nachweisen konnten. Erklären lässt sich dies durch die Beobachtung, dass unterhalb einer Luftfeuchtigkeit von etwa 30% der in Fig. 19 gezeigte lineare Zusammenhang nicht gültig ist. Ab ca. 80% der Luftfeuchtigkeit erfolgt die Zunahme der leitfähigen Bereiche ebenfalls nicht mehr linear (s. Fig. 20).

Bei Luftfeuchtigkeit >90% RH konnten die genauen Kanaldurchmesser nicht bestimmt werden, da die leitfähigen Gebiete nicht mit ausreichend hoher Auflösung abgebildet werden konnten und die Basis der Strompeaks oft stark in Scanrichtung verbreitert war. Bei relativ hoher Luftfeuchtigkeit wird ein großer Teil der Membranoberfläche mit Wasser benetzt, so dass auch eine bestimmte „Querleitfähigkeit" detektiert werden könnte, z.B. wenn die ionische Kanäle sehr nahe beieinander liegen. Die beschriebenen Verbreiterungen sind möglicherweise darauf zurückzuführen, dass Wasser an den Kanalausgängen an der AFM-Spitze haften blieb und von dieser ein Stück weit mitgezogen wurde, während die Auflösung im Allgemeinen sehr stark vom Zustand der Spitze abhängt.

Weitere Erkenntnisse über die Leitfähigkeit der Membran wurden durch die Betrachtung der statistischen Verteilung der Stromwerte über die untersuchte Fläche analysiert. Zu diesem Zweck wurden für die in Fig. 21 gezeigten Strombilder Histogramme erstellt (Fig. 22), in denen die Zahl der Pixel gegen die zugehörigen Stromwerte aufgetragen ist. Die dargestellten Histogramme weisen jeweils ein breites Maximum bei niedrigen Stromwerten sowie ein sehr viel schärferes Maximum bei den höchsten gemessenen Stromwerten auf. Die Tatsache, dass sich an einer relativ großen Zahl von Kanalausgängen exakt derselbe Protonenfluss detektierten lässt, worauf das Vorliegen des extrem scharfen Maximums bei hoher Stromstärke hindeutet, wird in der Literatur darauf zurückgeführt, dass die Nafion-Membran möglicherweise eine homogenere Struktur besitzt, als es eigentlich zu erwarten wäre. Alternativ wird eine starke Vernetzung der ionenleitenden Kanäle im Membraninnern als denkbare Ursache für das beschriebene Phänomen angeführt. Das Auftreten eines breiten Maximums bei niedrigerer Stromstärke ist vielleicht durch die Existenz einer Vielzahl von weniger stark vernetzten Poren zu erklären, die zum Porenausgang hin relativ schmal werden. Durch solche schmalen Porenteile kann ein Transport der Protonen nicht über den Grotthus-Mechanismus, sondern nur über die mit der Porenwand in Berührung kommenden, zwischen den Sulfonsäuregruppen verteilten Wassermoleküle, d.h. über einen Vehikel-Mechanismus, erfolgen. Der Protonen-Transport läuft auf diese Weise jedoch langsamer ab als ein Transport der Protonen anhand des Grotthus-Mechanismus. Aus diesem Grund kommen sowohl das beobachtete breite Maximum als auch der Hintergrundstrom möglicherweise durch das Vorhandensein einer Vielzahl engerer Porenausgänge auf der Membranoberfläche zu Stande.

Wie die Strom-Zeit-Diagramme Fig. 13, 14 zeigten, wird die Höhe des gemessenen Stromes durch die Dauer beeinflusst, für die die AFM-Spitze auf jedem einzelnen Messpunkt verweilt. Je länger sich die Spitze an einer bestimmten Stelle befindet, desto geringer ist der Stromfluss, der detektiert werden kann, da die Stromstärke mit einer Halbwertszeit von etwa 0.2 s exponentiell abnimmt. Somit ist es nicht verwunderlich, dass die höchsten Stromwerte bei der höchsten Scanfrequenz erhalten wurden und umgekehrt. Die leichte Abnahme der maximalen Stromwerte bei Erhöhung der Luftfeuchtigkeit von 60% auf 70% und gleich bleibender Scanfrequenz könnte dadurch zu Stande kommen, dass die Protonen bei einem Anschwellen der Membran etwas langsamer durch die Kanäle transportiert werden.

Eine Änderung der angelegten Spannung führt zu Veränderungen in der Leitfähigkeit einer Nafion-Membran (s. Fig. 21). Bei der Betrachtung der Größe der leitfähigen Bereiche lässt sich feststellen, dass bei Erhöhung der angelegten Spannung der Anteil der Membranoberfläche, auf dem ein Ionenfluss detektiert werden kann, konstant bleibt. Es ist zum Teil unerwartet, da bei einer Erhöhung der angelegten Spannung ein Protonentransport auch durch zuvor inaktive Kanäle stattfinden kann und damit der Anteil an leitender Oberfläche zunehmen könnte.

Des Weiteren gaben die durchgeführten Messungen erste Hinweise auf die Existenz eines kritischen Stromes. Dazu wurden die Membranoberfläche und Leitfähigkeit nur auf einem single-Scan-Profil durchgeführt Fig. 23, 24.

Die EC-AFM erlaubt eine detaillierte Betrachtung limitierender Parameter und ermöglicht dadurch die Rückführung der Leitfähigkeitsphänomene auf Betriebsparameter. In dieser Arbeit vorgestellte elektrochemische Raster-Kraft-Mikroskopie-Technik ist eine nützliche Methode für die Identifizierung und örtlich aufgelöste Charakterisierung der Protonenleitfähigkeit der Membranenoberfläche. Von besonderem Interesse ist hier die Aufklärung der Transportvorgänge in einer Pore einer Polymerelektrolyt-Membran.

- ✓ Die beobachtete Inhomogenität in der Stromverteilung kann zu lokal verstärkten Temperaturenunterschieden führen, besonders an Orten mit sehr hohem Reaktionsumsatz. Gleichzeitig kann die Membran an der Elektroden-Seite austrocknen, was einen erhöhten Membranenwiderstand verursacht und die Bildung von Radikalen induziert, die die Membranendegradation beschleunigen können. Weiterhin wird erwartet, dass die erhaltenen Resultate eine große Auswirkung im Hinblick auf die Optimierung des Wassermanagements und Membranenleitvermögens in der Brennstoffzelle haben werden. Die Existenz von Bereichen ohne signifikante Leitfähigkeit kann bedeuten, dass teure Edelmetallkatalysatoren hier inaktiv sind und nicht zum Strom beitragen können.

✓ Die Analyse der Zeitabhängigkeit des Stromflusses ermöglicht die Berechnung von realistischen Werten für die durchschnittliche Membranleitfähigkeit und den pH-Werten in den Poren der Membran.

✓ Die Effekte der Elektrodenkinetik und die Transportprozesse können auf dem Nanometermaßstab studiert und bei den theoretischen Berechnungen und Simulationen verwendet werden.

✓ Die EC-AFM-Technik ermöglicht nicht nur die Untersuchungen der leitfähigen Bereiche einer Nafion-Membran, sondern kann auch auf die neue, alternative Membranen, z.B. ionisch vernetzte polyaromatische Materialien, Block-copolymere, Compositmembranen, Polybenzimidazol-basierte Membranen ausgeweitet zu werden. Dabei stehen die Unterschiede in der Mikromorphologie und deren Auswirkung auf die Verteilung der ionischen Kanäle im Vordergrund. Durch die Bildanalyse gewonnene Information kann ein tieferes Verständnis zur Entwicklung neuartiger Polymere mit verbesserten protonenleitenden Strukturen beitragen.

Die vorgestellte Methode wurde hier entwickelt und erstmals eingesetzt. In den letzten zwei Jahren ist die Anzahl an Publikationen über elektrochemische Rasterkraft Mikroskopie deutlich gestiegen, was das große wissenschaftliche Interesse an diesen Systemen beweist. Es ist davon auszugehen, dass viele der Membranhersteller die neue Messmethode anwenden werden, da damit die Qualität der Membran und der Zusammenhang mit den Details des Herstellungsprozesses besser verstanden werden können. Gleichzeitig bietet sie Einblick in die fundamentalen Prozesse der Protonenleitung und in örtliche und zeitliche Modulationen der Eigenschaften der verwendeten Polymere. Mit diesem Verständnis kann zu einer Optimierung der Struktur der leitfähigen Membranen für eine Steigerung der Brennstoffzellen Performance führen.

7 LIST OF FIGURES

8 ABBREVIATIONS

PEMFC   Polymer Electrolyte Membrane Fuel Cell

PEM   Polymer Electrolyte Memnrane

OCP   Open Circuit Potential

AE   Activation Energy

PTFE   PolyTetraFluoroEthylene

EW   Equivalent Weight

PFSA   Perfluorosulfonic Acid

SPM   Scanning Probe Microscopy

STM   Scanning Tunneling Microscopy

AFM   Atomic Force Microscopy

SAXS   Small Angle X-ray Scattering

SANS   Small Angle Neutron Scattering

EIS   Electrochemical Impedance Spectroscopy (EIS)

TEM   Transmission Electron Microscopy

EC-AFM   Electrochemical Atomic Force Microscopy

RH   Relative Humidity

H_3O^+ Hydronium Ion

SO_3^- Sulfonic Group

9   ARTICLES PUBLISHED DURING THIS WORK

1.   E. Aleksandrova, R. Hiesgen, D. Eberhard, K. A. Friedrich, T. Kaz, E. Roduner, Proton conductivity study of a fuel cell membrane with nanoscale resolution. *ChemPhysChem* **2007**, *8*, 519.

2.   E. Aleksandrova, R. Hiesgen, K. A. Friedrich, E. Roduner, Electrochemical atomic force microscopy study of proton conductivity in a Nafion membrane. *Phys. Chem. Chem. Phys.* **2007**, *9*, 2735.

3.   R. Hiesgen, E. Aleksandrova, G. Meichsner, I. Wehl, E. Roduner, K. A. Friedrich, High-resolution imaging of ion conductivity of Nafion membranes with electrochemical atomic force microscopy. *Electrochim. Acta* **2009**, *55*, 423.

4.   S. Hink, E. Aleksandrova, E. Roduner, Electrochemical AFM investigations of proton conducting membranes. *ECS Trans.* **2010**, *33*, 57.

5.   E. Aleksandrova, S. Hink, R. Hiesgen, E. Roduner, Spatial distribution and dynamics of protonconductivity in fuel cell membranes: Potential and limitations of electrochemical atomic force microscopy measurements. *J. Phys. Condens. Matter* **2011**, *23*.

6.   R. Hiesgen, I. Wehl, E. Aleksandrova, E. Roduner, A. Bauder, K. Andreas Friedrich, Nanoscale properties of polymer fuel cell materials – a selected review. *International Journal of Energy Research*, **2009.**

7.   R. Hiesgen, D. Eberhardt, E. Aleksandrova, K. A. Friedrich, Structure and local reactivity of supported catalyst/Nafion layers by in-situ STM. *Fuel Cells* **2006**, *6*, 425.

8.   R. Hiesgen, D. Eberhardt, E. Aleksandrova, K. A. Friedrich, Investigation of structure and ORR reactivity of fuel cell catalysts by in-situ STM. *J. Appl. Electrochem.*, **2007**, *37*, 1495.

9.   B. Vogel, E. Aleksandrova, S. Mitov, A. Dreizler, J. Kerres and E. Roduner. Observation of Membrane Degradation by in-situ and ex-situ Electron Paramagnetic Resonance. *J. Electrochem. Soc.*, **2008**, 155 (6) B570.

10.   R. Hiesgen, E. Aleksandrova, E. Roduner, Visualisierung Ionen leitender Kanäle auf Polymer-Elektrolyt-Membranen mit dem elektrochemischen Rasterkraftmikroskop. *Horizonte*, **2008**, 31, 3.

10 BIBLIOGRAPHY

[1]   L. Carrette, K. A. Friedrich, U. Stimming, *Fuel Cells*, **1**, 5 (2001).

[2]   O. Savadogo, *J. Power Sources*, **127**, 135 (2004).

[3]   O. Savadogo, *J. New Mat. Electrochem. Systems*, **1**, 47 (1998).

[4]   K. A. Mauritz, R. B. Moore, *Chem. Rev.,* **104**, 4535 (2004).

[5]   E. Roduner, S. Schlick, ESR Methods for Assessing the Stability of Polymer Membranes Used in Fuel Cells, in: "Advanced ESR Methods in Polymer Research", Schlick, S. ed. Wiley, New York, (2006).

[6]   S. Srinivasan, R. Mosdale, P. Stevens & C. Yang, *Annu. Rev. Energy Env.,* **24**, 281 (1999).

[7]   U. Bossel, *The Birth of Fuel Cell* 1835-1845, European Fuel Cell Forum, Göttingen, 157 (2000).

[8]   W. R. Grove, *Phil. Mag*., **14**, 129 (1839).

[9]   W. R. Grove, *Phil. Mag*., **21**, 417 (1842).

[10]   A. J. Appleby and F. R. Foulkes, Van Nostrand Reinhold, *Fuel Cell Handbook*, New York, 792 (1989).

[11]   W. Vielstich, *Fuel Cells*, Wiley – Interscience, Bristol, 501 (1970).

[12]   A. J. Appleby, E. B. Yeager, *Energy,* **11,** 137 (1986).

[13]   G. Sattler, *J. Power Sources,* **86**, 61 (2000).

[14]   B. C. H. Steele, A. Heinzel, *Nature,* **414**, 345 (2001).

[15]   S. Gottesfeld, T. A Zawodzinski, *Polymer Electrolyte Fuel Cells in Advances in Electrochemical Science and Engineering*, R. C. Alkire, H. Gerischer, D. M. Kolb and C. W. Tobias (Ed.), Wiley-VCH, Weinheim, Vol. **5**, 197 (1997).

[16]   F. Barbir *PEM Fuel Cells: Theory and Practice*. Elsevier Academic Press (2005).

[17]   M. Adachi, Proton exchange membrane fuel cells: water permeation through Nafion membranes, Dissertation, Simon Fraser University (2010).

[18]   K. Kordesch, G. Simader, *Fuel Cells and Their Applications*, VCH-Verlag (1996).

[19]   M. Quintus, Dissertation, Universität Stuttgart (2002).

[20]   A. Panchenko, Dissertsation, Polymer Electrolyte Membrane Degradation and Oxygen Reduction in Fuel Cells: an EPR and DFT investigation, (2004).

[21]   I. D. Raistrick, in *Diaphragms, Separators, and Ion Exchange Membranes*, J. W. Van Zee, R. E. White, K. Kinoshita, and H. S. Burney, Editors, PV 86-13, The Electrochemical Society Proceedings Series, Pennington, NJ. (1986).

[22]   F. Uribe, T. Zawodzinski, J. Valerio, G. Bender, F. Garzon, A. Saab, T. Rockward, P. Adcock, J. Xie, and W. Smith, in *Proc. 2002 Fuel Cell Lab R&D Meeting*, *DOE Fuel Cells for transportation Programm*.

[23]   T. R. Ralph, M. P. Hogarth, *Platinum Met. Rev.*, **46**, 3 (2002).

[24]   G. G. Scherer, Ber. Bunsenges. *Phys. Chem.,* **94**, 1008 (1990).

[25]   Aldrich, Technical Information Bulletin, No AI-163, Aldrich Chemical Company, Inc. P.O. box 355, Milwaukee, WI 53201, USA.

[26]   L. Depre, J. Kappel, M. Poppall, *Electrochim. Acta*, **43**, 1301 (1998).

[27] B. Bonnet, D. J. Jones, J. Roziere, L. Tchicaya, G. Alberti, M. Casciola, L. Massinelli, B. Baner, A. Peraio, E. Ramunni, *J. New Mat. Electrochem. Systems*, **3**, 87 (2000).

[28] J. Kerres, A. Ullrich, M. Hein, *J. Pol. Sci.*, **39**, 2874 (2001).

[29] J. Kerres, *J. Membr. Sci.*, **185**, 3 (2001).

[30] Q. Guo, P.N. Pintauro, H. Tang, S. O'Connor, *J. Memb. Sci.*, **154**, 175 (1999).

[31] B. Vogel, H. Dilger, E. Roduner. *Macromolecules*, **43**, 468 (2010)

[32] B. Vogel, Dissertsation, Zersetzungsmechanismen von Polymerelektrolyt-membranen für Brennstoffzellenanwendungen (2010).

[33] S. J. Hamrock, M. A. Yandrasits, *J. Macromolecular Sci., Part C: Polymer Reviews*, **46**, 219 (2006).

[34] Nafion product sheet, Dupont NAE101, February 2004.

[35] L. Gubler, S. A. Gürsel, G. G. Scherer, *Fuel Cells*, **5**, 317 (2005).

[36] H. P. Brack, F. N. Büchi, J. Huslage, G. G. Scherer, *in Proc. 2nd Symposium on Proton Conducting Membrane Fuel Cells II*, ed. S. Gottesfeld and T. F. Fuller, The Electrochemical Society, Boston MA, USA, vol. 98–27, 52 (1998).

[37] G. Alberti, M. Casciola, *Solid State Ionics* 145, **3** (2001).

[38] L. Rubatat, Ph. D. Thesis, Grenoble (2003).

[39] T. D. Gierke, G. E. Munn, F. C. Wilson, *J. Polym. Sci., Polym. Phys.*, **19**, 1687, (1981).

[40] W. Y. Hsu, T. D. Gierke, *Macromolecules* **15**, 101 (1982).

[41] W. Y. Hsu, T. D. Gierke *J. Membr. Sci.* **13**, 307 (1983).

[42]   T. D. Gierke, W. Y. Hsu, In *Perfluorinated Ionomer Membranes*, A. Eisenberg, H. L. Yeager, Eds.; ACS Symposium Series No. 180; American Chemical Society: Washington, DC; **13**, 283 (1982).

[43]   H. J. Yeager, A. Eisenberg, in: *Perfluorinated Ionomer Membranes*; Eds. Eisenberg, A. and Yeager, H. L. ACS Symp. Ser. No.180, (American Chemical Society: Washington, DC) **41**, p. 1-6, (1982).

[44]   S. Rieberer, K. H. Norian, *Ultramicroscopy*, **41**, 225 (1992).

[45]   T. Xue, J. S. Trent, K. Osseo-Asare, *J. Membr. Sci.*, **45**, 261 (1989).

[46]   A. Gruger, A. Regis, T. Schmatko, P. Colomban, *Vibrational Spectroscopy*, **26**, 215 (2001).

[47]   P. J. James, M. Antognozzi, J. Tamayo, T. J. McMaster, J. M. Newton, and M. Miles, J. *Langmuir*, **17**, 349 (2001).

[48]   B. Dreyfus, G. Gebel, P. Aldebert, M. Pineri, & M. Escoubes, *J. Phys. France*, **51**, 1341 (1990).

[49]   H. L. Yeager, A. Steck, *J. Electrochem. Soc.*, **128**, 1880 (1981).

[50]   E. J. Roche, M. Pineri, R. Duplessix, *J. Polym. Sci., Polym. Phys.* Ed., **20**, 107 (1982).

[51]   E. J. Roche, M. Pineri, R. Duplessix, A. M. Levelut, *J. Polym. Sci., Polym. Phys.* Ed., **19**, 1 (1981).

[52]   H. W. Starkweather, Jr., *Macromolecules*, **15**, 320 (1982).

[53]   K. Schmidt-Rohr, & Q. Chen, *Nature Mater.*, **7**, 75 (2008).

[54]   R. S. McLean, M. Doyle, B.B. Sauer, *Macromolecules*, **33**, 6541 (2000).

[55]   Fu-Ren F. Fan, A. J. Bard, *Science*, **270**, 1849 (1995).

[56]   R. O'Hayre, M. Lee, and F. B. Prinz, *J. Appl. Phys.*, **95**, 8382 (2004).

[57]   D. A. Bussian, J. R. O'Dea, H. Metiu, S. K. Buratto, *Nanoletters*, 7, 227 (2007).

[58]   X. Xie, O. Kwon, Da-Ming Zhu, T. V. Nguyen, and G. Liu, *J. Phys. Chem. B*, **111**, 6134 (2007).

[59]   M. Cappadonia, J.W. Erning, S.M. Saberi Niaki, U. Stimming, *Sol. State Ionics*, **77**, 65 (1995).

[60]   M. Ise, K. D. Kreuer, J. Maier, *Sol. State Ionics*, **125**, 213 (1999).

[61]   P. Berg, K. Promislow, J. S. Pierre, J. Stumper, B. Wetton, *J. Electrochem. Soc.*, **151**, A341 (2004).

[62]   M. Watanabe, H. Uchida, Y. Seki, M. Emori, P. Stonehart, *J. Electrochem. Soc.*, **143**, 3847 (1996).

[63]   C. R. Buie, J. D. Posner, T. Fabian, S-W. Cha, D. Kim, F. B. Prinz, J. K. Eaton, and J. G. Santiago, *J. Pow. Sources*, V **161**, 191, (2006).

[64]   S. Gottesfeld, T. A. Zawodzinski, R. C. Alkire, H. Gerischer, D. M. Kolb and C. W. Tobias 1997, Advances in electrochemical science and engineering, Polymer Electrolyte Fuel Cells, 195–301 Wiley-VCH Vol.**5**.

[65]   A. V. Anantaraman, C. L. Gardner *J. Electroanal. Chem.*, **414** (2), 115-120 (6) (1996).

[66]   K. D. Kreuer, *Chem. Mat.*, **8**, 610 (1996).

[67]   E. Spohr, P. Commer A. A. Kornyshev, *J. Phys. Chem. B*, **106**, 10560, (2002).

[68]   T. A. Zawodinski, C. Derouin, S. Rodzinski, R. J. Sherman, V. T. Smith, T. E. Springer, S. Gottesfeld, *J. Electrochem. Soc.*, **140**, 1041, (1993).

[69]   S. J. Paddison, *Annu. Rev. Mater. Res.*, **33**, 289 (2003).

[70]   P. Commer, A. G. Cherstvy, E. Spor, and A. A. Kornyshev, *Fuel Cells*, **2**, 127, (2002).

[71]   J. A. Elliott, S. J. Paddison, *Phys. Chem. Chem. Phys.*, **9**, 2602 (2007).

[72]   R. Devanathan, A. Venkatnathan, M. Dupuis, *J. Phys. Chem. B*, **111**, 13006 (2007).

[73]   S. Mafe, J. A. Manzanares, P. Ramirez, *Phys. Chem. Chem. Phys.*, **5**, 376 (2003).

[74]   S. Gottesfeld, T. A. Zawodzinski, R. C. Alkire, H. Gerischer, D. M. Kolb, C. W. Tobias, *Advances in electrochemical science and engineering*, *Polymer Electrolyte Fuel Cells*, **1997,** 195–301 Wiley-VCH Vol. 5.

[75]   T. Colinart, S. Didierjean, O. Lottin, G. Maranzana and C. Moyne, J. Electrochem. Soc. **155** (3), B244, 2008.

[76]   S. J. Paddison, J. A. Elliott, *J. Phys. Chem. A*, **109**, 7583 (2005).

[77]   S. Urata, J. Irisawa, A. Takada, W. Shinoda, S. Tsuzuki, M. Mikami, *J. Phys. Chem. B*, **109**, 4269 (2005).

[78]   A. Venkatnathan, R. Devanathan, M. Dupuis, *J. Phys. Chem. B*, **111**, 7234 (2007).

[79]   E. Spohr, *Mol. Simul.*, **30**, 107 (2004).

[80]   J. T. Wescott, Y. Qi, L. Subramanian, T. W. Capehart, *J. Phys.Chem. B*, **124**, 134702 (2006).

[81]   R. Devanathan, A. Venkatnathan, M. Dupuis, *J. Phys. Chem. B*, **111**, 8069 (2007).

[82]   K. D. Kreuer, S. J. Paddison, E. Spohr, M. Schuster, *Chem. Rev.*, **104**, 4637 (2004).

[83]   M. Eikerling, A. A. Kornyshev and U. Stimming, *J. Phys. Chem. B*, **101**, 10807 (1997**)**.

[84]   K. D. Kreuer, *Chem. Mat.* **8**, 610 (1996).

[85]   M. Eikerling, A. A. Kornyshev, *J. Electroanal. Chem.*, **502**, 1 (2001).

[86]   M. Eikerling,Y. I. Kharkats, A. A. Kornyshev. and Y. M. Volfkovich, *J. Electrochem. Soc.*, **145**, 2684 (1998).

[87]   X. Yan, M. Hou, L. Sun, D. Liang, Q. Shen and H. Xu et al., *Int. J. Hydrogen Energy* **32**, 4358 (2007).

[88]   T. J. P. Freire, E. R. Gonzalez, *J. Electroanal. Chem.*, **503**, 57 (2001).

[89]   X. Yuan, H. Wang, J.C. Sun and J. Zhang, *Int. J. Hydrogen Energy* **32**, 4365 (2007).

[90]   E. B. Easton and P.G. Pickup, *Electrochim Acta* **50** (12) 2469 (2005).

[91]   F. N. Büchi, A. Marek and G. G. Scherer, *J. Electrochem. Soc.* **142** (6) 1895, (1995).

[92]   Z. Siroma, T. Ioroi, N. Fujiwara and K. Yasuda, *Electrochem. Commun.* **4**, 143 (2002).

[93]   I. A. Schneider, H. Kuhn, A. Wokaun, G. Scherer, *J. Electrochem. Soc.* **152**, (10) A2092 (2005).

[94]   I. Radeva, G. Georgiev, V. Sinigersky, E. Slavcheva *Int. J. Hydrogen Energy* (2008).

[95]   T. Okada, G. Xie, O. Gorseth, S. Kjelstrup, N. Nakamuraa, and T. Arimura, *Electrochim. Acta*, **43**, 3741 (1998).

[96]   A. V. Anantaraman, C. L. Gardner, *J. Electroanal. Chem.* **414**, 115 (1996).

[97]   S. Slade, S. A. Campbell, T. R. Ralph, and F. C. Walsh, *J. Electrochem. Soc.*, **149**, A1556 (2002).

[98]   T. A. Zawodzinski, T. E. Springer, J. Davey, R. Jestel, C. Lopez, J. Valerio, S. Gottesfeld, *J. Electrochem. Soc.*, 140, 1981 (1993).

[99]   S. Ma, A. Kuse, Z. Siroma, K. Yasuda, Espec Technolgy Report No20, 2005.

[100] M. Casciola, G. Alberti, M. Sganappa, R. Narducci, *J. of Pow. Sources* **162**, (2006) 141.

[101] G. Alberti, R. Narducci, M. Sganappa, *J. of Pow Sources* **178**, (2008) 575.

[102] G. Binnig, C. F. Quate, Ch. Gerber *Phys. Rev. Lett.* **56**, 930 (1986).

[103] P. Eaton and P. West, *Atomic Force Microscopy*, Chapter 3: AFM Modes, pp. 49. OUP, (2010).

[104] N. Jalili, K. Laxminarayana *Mechatronics Journal.,* **14**, 8, 861 (2004).

[105] B. R. Horrocks and G. Wittstock, In: A. J. Bard and M.V. Mirkin, Editors, *Scanning Electrochemical Microscopy*, Marcel Dekker, New York p. 445 (2001).

[106] G. Wittstock. "Imaging Localized Reactivities of Surfaces by Scanning Electrochemical Microscopy". *Topics in Applied Physics* **85**, 335 (2003).

[107] I. Horcas, *Rev. Sci. Instrum.* **78**, 13705 (2007).

[108] R. Hiesgen, J. Haiber, Measurement techniques: AFM In: J. Garche, C. Dyer, P. Moseley, Z. Ogumi, D. Rand and B Scrosati. *Encyclopedia of Electrochemical Power*, Vol 2. Amsterdam, Elsevier (2009).

[109] E. Gülzow, M. Schulze, N. Wagner, T. Kaz, R. Reissner, G. Steinhilber, A. Schneider, *J. Pow. Sources* **86**, 352 (2000).

[110] E. Aleksandrova, R. Hiesgen, K. A. Friedrich, E. Roduner, *Chem. Phys. Chem.* **8**(4), 519 (2007).

[111] E. Roduner, R. Hiesgen, "Spatially resolved measurements for PEMFC membranes". In: J. Garche; C. Dyer; P. Moseley; Z. Ogumi; D. Rand; B. Scrosati (Hrsg.): Encyclopedia of Electrochemical Power Sources: Basics: "Measurement techniques: AFM". Elsevier Science. - ISBN 978-0-444-52745-5.

[112] J. A. Elliott, S. Hanna, A. M. S. Elliott, G. E. Cooley, *Polymer*, **42**, 2251 (2001).

[113] R. S. Yeo, *Polymer*, **42**, 432 (1980).

[114] A. Affoune, A. Yamada, M.Umeda, *J. Power Sources*, **148**, 9 (2005).

[115] P. J. James, T. J. McMaster, J. M. Newton, M. J. Miles, *Polymer*, **41**, 4223 (2000).

[116] P. J. James, J. A. Elliott, T. J. McMaster, J. M. Newton, A. M. S. Elliott, S. Hanna, M. J. Miles, *J. Mat. Sci.*, **35**, 5111–5119 (2000).

[117] E. Aleksandrova, S. Hink, R. Hiesgen, E. Roduner, *J. Phys.: Condens. Matter* **23,** 234109 (2011).

[118] E. Aleksandrova, R. Hiesgen, K. A. Friedrich and E. Roduner, *Phys. Chem. Chem. Phys.***9**, 2735 (2007).

[119] F. N. Büchi, G. G. Scherer, *J. Electrochem. Soc.* **148**, A183-A188 (2001).

[120] Y. Sone P. Ekdunge and D. Simonsson, *J. Electrochem. Soc.*, **143**, 1254 (1996).

[121] M. Eikerling, A. A. Kornishev, A. M. Kusnetsov, J. Ulstrup and S. Walbran, *J. Phys. Chem. B* **105**, 3646 (2001).

[122] X. Xie, O. Kwon, Z. Da-Ming, T. V. Nguyen and G. Liu, *J. Phys. Chem.* B **111,** 6134 (2007).

[123] B. Dreyfus, G. Gebel, P. Aldebert, M. Pineri, M. Escoubes, M. Thomas, *J. Phys. (Paris)* **51,** 1341 (1990).

[124] D. B. Spry, A. Goun, K. Glusac, David E. Moilanen and M. D. Fayer, *J. Am. Chem. Soc.* **129**, 8122 (2007).

[125] L. Rubatat, G. Gebel & O. Diat, *Macromolecules* **37**, 7772 (2004).

[126] L. Rubatat, A. L. Rollet, G. Gebel, O. Diat, *Macromolecules* **35**, 4050 (2002).

[127] H. G. Haubold, T. Vad, H. Jungbluth, P. Hiller, *Electrochim. Acta,* **46**, 1559 (2001).

[128] R. Hiesgen, I. Wehl, E. Aleksandrova, E. Roduner, A. Bauder, K. A. Friedrich *Int. J. Energy Res.* **34**, 1223 (2009).

[129] Y. Kang , O. Kwon , X. Xie, Da-Ming Zhu, J. Phys. Chem. B, 113, 15040 (2009)

[130] N. Takimoto, S. Takamuku, M. Abe, A. Ohira, H.Lee, J. E. McGrath *J. of Pow. Sources* **194**, 662 (2009).

[131] S. Hink , N. Wagner, W. G. Bessler, E. Roduner, *Membranes* **2**, 237 (2012).

CURRICULUM VITAE
ELENA ALEKSANDROVA

PERSONAL INFORMATION

Elena Aleksandrova

Birthday place   Kazakhstan, Presnowka

EDUCATION / WORK

01.01.2012	Daimler AG, Sindelfingen, Passenger car development. Development and integration of PHEV batteries.
01.01.2009-31.12.2011	Honda R&D Europe (Deutschland) GmbH Carl-Legien-Str. 30, 63073 Offenbach am Main.
	Project responsibility: Lithium ion battery research, hydrogen storage and thermo-electric materials.
01.10.2005-31.12.2008	Ph.D. Thesis at the University of Stuttgart, Institute of Physical Chemistry, Chair of Professor Dr. E. Roduner. Ph.D. Thesis: „Electrochemical atomic force microscopy study of proton conductivity in polymer electrolyte fuel cell membranes".
07.10.2005-10.03.2006	Participation in the South German Catalysis Institute courses.
15.09.2000-15.09.2005	Study of Chemistry at the University of Stuttgart. Diploma thesis: „*In-situ* electron spin resonance study of fuel cell polymer membrane degradation".
01.03.1996-01.07.2000	Abiturabschluss at the Evangelische Firstwald-gymnasium Mössingen. Degree: General qualification for university entrance.

TEACHING

01.03.2005-31.12.2008	Teaching assistant at the Institute of Physical Chemistry, Stuttgart. Supervision of the laboratory work for the graduate students.
01.06.2006-31.12.2008	Supervision of two student research projects:
	• Untersuchungen zur Stabilität der Niedertemperatur-Brennstoffzellen-Membranen mittels ESR.
	• Untersuchung der Protonenleitfähigkeit einer Nafion 112 Membran mit Hilfe der Elektrochemischen Raster-Kraft-Mikroskopie (EC-AFM).
01.10.2004-01.03.2005	Scientific assistant at the Institute of Biochemistry, chair of Professor Dr. B. Singer Krüger.
01.03.2003-01.08.2004	Teaching assistant at the Institute of Inorganic Chemistry.

AWARDS / CONFERENCES

June 2006, Ulm, Germany, **10th Ulm Electrochemical Talks**. First price for the diploma thesis: „*In-situ* electron spin resonance study of fuel cell polymer membrane degradation".

June 2007, Vitznau Switzerland, **DSM Innovation – Science & Technology Award 2007**, presented project: "Electrochemical Atomic Force Microscopy: Proton Transport in Fuel Cell Membranes".

September 2007, Stuttgart, **F-Cell Award 2007**, Sonderpreis: "Entwicklung einer elektrochemischen Rasterkraftmikroskopie-Methode für die Untersuchung der Leitfähigkeit von Polymerelektrolyt-Membranen".

April 2006, Neu-Ulm, **O$_2$ Red-Net: Efficient Oxygen Reduction for the Electrochemical Energy Conversion**. Poster: „Nanostructure and local reactivity of catalysts fort he oxygen reduction reaction".

May 2006, Erlangen, **105. Bunsentagung**, Poster: "*In-situ* EPR investigation of polymer electrolyte membrane degradation in fuel cell applications".

June 2006, Düsseldorf, **87. AGEF-Seminar und NRW-Netzwerk NanoEnergie: Workshop: *In-situ* Messmethoden in Brennstoffzellen**. Presentation: „*In-situ* ESR-Untersuchungen zur Stabilität der Brennstoffzellen-Membranen".

January 2007, Bonn, **Forum Process Engineering**.

February 2007, Asilomar California USA, **Advances in Materials for Proton Exchange Membrane Fuel Cell Systems**. Poster: "Visualization of ionic active channels in the Nafion membrane by using Electrochemical Atomic Force Microscopy".

September 2007, Crete Greece, **International workshop on degradation issues of fuel cells**, invited talk and poster presentation.

October 2007, Washington, DC**, 212th Meeting of The Electrochemical Society**, talk and poster presentation.

June 2008, Berlin, 4th Gerischer Symposium, **Electrochemistry with Spatial and Temporal Resolution**, poster presentation.